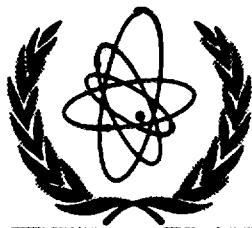




XA9745761



International Atomic Energy Agency

INDC(BLR)-009

Distr. G

**INDC**

**INTERNATIONAL NUCLEAR DATA COMMITTEE**

## **EVALUATION OF NEUTRON DATA FOR PLUTONIUM-238**

V.M. Maslov, E.Sh. Sukhovitskij, Yu.V. Porodzinskij,  
G.B. Morogovskij

Radiation Physics & Chemistry Problems Institute  
220109, Minsk-Sosny, Belarus

October 1997

**IAEA NUCLEAR DATA SECTION, WAGRAMERSTRASSE 5, A-1400 VIENNA**

**29-02**

**We regret that  
some of the pages  
in this report may  
not be up to the  
proper legibility  
standards, even  
though the best  
possible copy was  
used for scanning**

Reproduced by the IAEA in Austria  
October 1997

## EVALUATION OF NEUTRON DATA FOR PLUTONIUM-238

V.M. Maslov, E.Sh. Sukhovitskij, Yu.V. Porodzinskij,  
G.B. Morogovskij

Radiation Physics & Chemistry Problems Institute  
220109, Minsk-Sosny, Belarus

### Abstract

The evaluation of neutron data for  $^{238}\text{Pu}$  is made in the energy region from  $10^{-5}$  eV up to 20 MeV. The results of the evaluation are compiled in the ENDF/B-VI format.

This work is performed under the Project Agreement CIS-03-95 with the International Science and Technology Center (Moscow). The Financing Party for the Project is Japan. The evaluation was requested by JNDC (JAERI, Japan).

Date of Manuscript: August 6, 1997

# Contents

<b>1. Introduction</b>	7
<b>2. Resolved resonance region</b>	7
2.1 Previous evaluations of resolved resonance parameters	7
2.2 Measured data fitting	8
2.2.1 Status of experimental data	8
2.2.2 Energy region below 20 eV	10
2.2.3 Energy region 20 ÷ 500 eV	10
2.2.4 Resonance parameter analysis	11
<b>3. Unresolved resonance region</b>	12
3.1 Review	12
3.2 The s-wave average resonance parameter evaluation	12
3.2.1 Estimate of resonance level missing influence on $\langle D_{\text{obs}} \rangle$ and $S_0$	12
3.2.2 Evaluation of $\langle D_{\text{obs}} \rangle$ , $S_0$ , $\langle \Gamma_\gamma \rangle$ and $\langle \Gamma_f \rangle$ based on the resolved resonance parameters	12
3.3 The s-, p- and d-wave average resonance parameter evaluation	13
3.3.1 Neutron width	13
3.3.2 Neutron resonance spacing	13
3.3.3 Fission width	14
3.3.4 Radiative capture width	14
3.4 Cross section evaluation in the region 0.5-44.2667 keV	14
3.4.1 Fission cross section energy dependence	14
3.4.2 Capture cross section energy dependence	14
3.4.3 Comparison of present, JENDL-3 and ENDF/B-VI evaluated data	15
3.4.4 Drawbacks of ENDF/B-VI format and associated inconsistencies in neutron cross sections	16
<b>4. Fast neutron cross sections</b>	16
4.1 Optical potential	16
4.2 Fission cross section	17
4.2.1 Status of the experimental data	17
4.2.2 Statistical model calculation of fission cross section	18
4.2.3 Fission transmission coefficient, level density and transition state spectrum	18
4.2.4 Fission cross section above emissive fission threshold	21
4.3 Inelastic scattering cross section	21
4.3.1 Levels of $^{238}\text{Pu}$	22
4.3.2 $^{238}\text{Pu}$ level density	22
4.3.3 $^{239}\text{Pu}$ level density	23
4.3.4 Compound inelastic scattering	23
4.3.5 Direct inelastic scattering	24
4.4 Radiative capture cross section	24
4.5 Cross sections of (n,2n) and (n,3n) reactions	24

<b>5.</b>	<b>Energy distributions of secondary neutrons</b>	25
5.1	Model calculations of (n,nx) reaction spectra	25
5.2	Prompt fission neutron spectra	26
5.2.1	Prompt fission neutron spectra evaluation	26
<b>6.</b>	<b>Number of neutrons per fission</b>	28
<b>7.</b>	<b>Angular distributions of secondary neutrons</b>	29
<b>8.</b>	<b>Conclusions</b>	29
<b>9.</b>	<b>Figure captions</b>	33

## 1 Introduction

The advanced nuclear fuel cycle studies request the nuclear data of minor actinides [1]. The neutron data for  $^{238}\text{Pu}$  are important also for non-proliferation concepts development. In this work the evaluation of  $^{238}\text{Pu}$  neutron data is performed. The quantities evaluated are resolved and unresolved resonance parameters, total, elastic and inelastic scattering, fission, capture,  $(n,2n)$  and  $(n,3n)$  reaction cross sections, angular and energy distributions of secondary neutrons, including partial  $(n,xn)$  and  $(n,xnf)$  reaction spectra, fission spectra and number of neutrons per fission. The incident neutron energy range covered is from  $10^{-5}$  eV up to 20 MeV. The evaluated quantities are compared with JENDL-3 [2], ENDF/B-VI [3] and JEF-2 [4] evaluations.

## 2 Resolved resonance region

### 2.1 Previous evaluations of resolved resonance parameters

In ENDF/B-VI Breit-Wigner single-level parameters by Young et al. [5] up to 200 eV are adopted.

In JENDL-3 evaluation four resonance parameters by Young et al. [5] up to 10 eV, including two negative resonances, are adopted. Above 10 eV up to 500 eV 49 resonance parameters by Silbert et al. [6] were employed. Thermal fission cross section estimate by Mughabghab [7] was used to get first positive and negative resonance parameters.

In JEF-2 evaluation negative resonance parameters by Young et al. [5] are adopted. Parameters of first three positive resonances are adopted from Stabbins et al.[8] and Young et al.[5]. Above 20 eV resonance parameters by Silbert et al. [6] are adopted with minor modifications.

The purpose of current resonance parameter evaluation is to extract the resolved resonance parameters up to 500 eV and to reconcile the available fission data by Budtz-Jorgensen et al. [9] from 5.5 eV up to 500 eV and Alam et al.[10] from 0.1 eV up to 100 keV with bomb-shot fission data by Silbert et al.[6] and Drake et al. [11], let alone the consistent analysis of total cross section data by Young et al. [5], fission cross section data [6, 8, 9, 10, 11, 12] and capture data by Silbert et al.[13].

## 2.2 Measured data fitting

Basically there is only one fission cross section measurement by Budtz-Jorgensen et al. [9] covering almost whole energy region of interest (up to 10 MeV). The latest fission cross section measurement by Alam et al.[10] is roughly compatible with the former measurement at low energies. Current state of the measured data base at resolved resonance energies is as follows. The extensive bomb-shot data cover energy range of 18 eV - 500 eV. At lower energies down to thermal point we fit basically data by Alam et al. [10], the same is the case above 500 eV. In the intermediate energy range we maintain the data fit attributing highest statistical weight to the data points by Alam et al.[10].

### 2.2.1 Status of experimental data

**2.2.1.1 Fission data** Neutron induced fission cross section have been measured by Stubbins et al. [8] from 2 eV to 4 MeV. The neutrons were produced at 30-MeV linac. Fission fragments were detected with a spark chamber, which contained 63 mg of  $^{238}\text{Pu}$ . The fission cross section of  $^{238}\text{Pu}$  relative to  $^{239}\text{Pu}$  (resonance fission areas in the overlapping region) was normalized using absolute fission cross section by Barton and Koonts [14] at 3 MeV, the uncertainty of normalization is about 40 % ( $2.5 \pm 0.12$  barns was obtained relative to 1.3 barns for  $^{235}\text{U}$ , while relative to  $^{239}\text{Pu}$ ,  $\sigma_f = 2$  barns). Values of  $\Gamma_n^o \Gamma_f / \Gamma$  are provided. Fission resonances are identical to those detected in total cross section measurement by Young et al. [5], except 59.8-eV resonance. Above 0.1 MeV the data shape is different from that of Butler and Sjoblom [15] data, measured in the energy interval 0.14 MeV - 1.75 MeV.

Gerasimov [12] has measured energy dependence of fission cross section from 0.02 to 400 eV. The neutrons were produced with linac. Fission cross section was normalized to the thermal fission cross section value of 16.6 barn. The fission areas of first and second resonances are compatible with other data, while those of next three resonances are about two times lower than values obtained by Budtz-Jorgensen et al. [9].

The bomb-shot fission cross section data of Silbert et al.[6] are available in the energy region of 18 eV - 3 MeV. The neutron flux was measured relative to the reactions  $^3\text{He}(n,p)$  (18-100 eV),  $^6\text{Li}(n,\alpha)$  (100 - 1000 eV) and  $^{235}\text{U}(n,f)$  (above 1000 eV,  $^{235}\text{U}$  data by Davey [16] were used). Fission cross section areas are reported for 49 resonances below 500 eV, the fission resonance areas are compatible with data by Stubbins et al.[8]. Pointwise data are also available. A number of previously unobserved resonances, either in fission and total cross section measurements, are reported, the estimate of  $D = 9.5 \pm 0.7$  eV is obtained. Estimate of second well resonance spacing



$D_{II}$  of 1 keV is obtained by analysis of intermediate structure. The bomb-shot measurement are inherently very sensitive, while the energy resolution is poorer than that obtained with linacs. Intermediate structure is evident above  $\sim 300$  eV.

Fission cross section is measured by Budtz-Jørgensen et al. [9] from 5 eV up to 10 MeV. The range of 5 eV - 2 MeV is covered with linac. Influence of  $\alpha$ -pileup was diminished with specially designed fission chamber. Above 150 keV Van de Graaff accelerator is employed. Above 100 keV fission cross section is measured relative to  $^{235}\text{U}$  fission cross section of ENDF/B-V, at lower energies relative to the  $^6\text{Li}(n,\alpha t)$  cross section shape. To normalize fission data below 100 keV fission integral of  $^{235}\text{U}$  (240 barn $\times$ eV)[17] between 7.8 and 11 eV is used. Fission width and fission areas below 500 eV are obtained for resonances except the first one, they are consistent with data by Stubbins et al. [8]. The sensitivity is an order of magnitude worse than in bomb-shot experiment by Silbert et al. [6], however the resolution is a factor of two better. Value of  $\Gamma_\gamma = 34$  meV is assumed throughout, a fission widths were obtained using capture areas obtained by Silbert et al. [13], except that of 9.97-eV resonance.

Recently the fission data measurements in the energy range from 0.1 eV to 100 keV, made with linac at RINS spectrometer were reported by Alam et al.[10]. The fission areas and widths for three first resonances were defined, however they disagree with data by Budtz-Jørgensen et al.[9]. The fission resonance integral is found to be  $15.9 \pm 0.6$  barns. The  $\alpha$ -pileup effects were suppressed. The fission data are normalized to resolution-broadened ENDF/B-V  $^{235}\text{U}$  fission cross section. Broad peaks near 280, 600 and 6500 eV are noticed.

**2.2.1.2 Total cross section data** Total cross section was measured by Young et al.[5] from 0.008 eV to 6500 eV. They provide single-level Breit-Wigner parameters below 200 eV. Thermal total cross section is measured to be  $588^{+15}_{-25}$  barns, thermal absorption cross section is predicted to be  $532^{+15}_{-25}$  barns. Resonance absorption integral is calculated with resonance parameters up to 200 eV and average resonance parameters at higher energies, to be  $164 \pm 15$  barns. To fit the data below 2 eV two negative resonances are employed. From 2 eV up to 200 eV resonance parameters are obtained by shape fitting and area analysis. Above 130 eV up to 200 eV there might be clusters of unresolved resonances. The radiative width  $\Gamma_\gamma = 38$  meV was assumed for resonances above 22 eV. That is just an average for the first three positive resonance values. Potential scattering cross section used is 17 barns. Neutron strength function  $S_0 = 1.1 \pm 0.2$  was obtained.

**2.2.1.3 Capture cross section data** Capture cross section was measured by Silbert et al.[13] above 17.79 eV. There is a strong non-resonant contribution evident in resonance valleys. Data could be used to extract partial widths of strong capture resonances only.

### 2.2.2 Energy region below 20 eV

Thermal total and fission cross sections are defined by varying negative resonance parameters which fit also the data shape up to 1 eV. We assumed potential scattering cross section of 17 barns to fit thermal total cross section value of 588.3 barns. This high value of potential scattering cross section one needs to fit total cross section data by Young et al. [5] in valleys between resonances. Afterwards we used the scattering radius  $P = 9.238$  Fm, obtained with optical model calculations. That leads to the renormalization of evaluated total cross section to the value of 579.642 barns.

The first resonance occurs at 2.882 eV. The values of  $\Gamma_n^o$ ,  $\Gamma_f$  and  $\Gamma_\gamma$  for the 2.882-eV, 9.971-eV and 18.56-eV resonances are defined by fitting in effect data by Alam et al.[10] and Gerasimov [12].

### 2.2.3 Energy region 20 ÷ 500 eV

The  $\Gamma_n^o$ ,  $\Gamma_f$  and  $\Gamma_\gamma$  resonance parameters are derived by consistent analysis of total [5], fission [6, 9, 10, 11] and capture [13] measured data. The main problem of fission data fitting is the relative weighting of different data. Data by Alam et al. [10], which are fitted below 20 eV have rather poor energy resolution at higher energies. Figure 2.1 shows the fit of data by Alam et al. [10] up to 500 eV. Actually we will use them to estimate the average cross section value above 18 eV. Data by Budtz-Jorgensen et al. [9] seem to have rather high background, hence we decreased their weight twice, as compared with the weight we attributed to the data by Alam et al. [10]. Relative weight of bomb-shot data by Silbert et al. [6] and Drake et al. [11] was decreased after fission resonance area analysis by 50% and 30 %, respectively. Data by Stubbins et al. [8] are discrepant with data by Alam et al. [10] below 10 eV, hence we decreased their weight 5-fold. Total cross section data by Young et al.[5] should be used for fitting purposes only up to ~55 eV. Because of poor resolution at higher energies we will use them only for illustrative purposes. Figures 2.2, 2.3, 2.4, 2.5 show the comparison of total cross section, calculated with present resonance parameters with measured data. Figures 2.2 and 2.3 demonstrate data measured by Young et al.[5] with different resolution. Present parameters describe data at resonance peaks somewhat better. Figures 2.4 and 2.5 show the improvement of total data description above 145 eV up to 350 eV. Decrease of neutron width of 320.5-eV resonance from 170 meV up to 75 meV improves data

description sufficiently. Figures 2.6, 2.7, 2.8 show different fission data fits in the energy interval 100 - 150 eV. Figure 2.8 shows that the measurements by Budtz-Jorgensen et al. [9] are made with good resolution, while there is large background contribution in the valleys between resonances. The same drawback is observed in case of capture data by Silbert et al. [13] (see fig. 2.9). At still higher energies 284.5-eV class II resonance is observed with anomalous fission width value of 3.37 eV. Figures 2.10, 2.11, 2.12 show different fission data descriptions in the energy interval 250 - 350 eV. Capture cross section measured data in this energy interval also demonstrates non-resonance contribution (see Fig.2.13).

#### 2.2.4 Resonance parameter analysis

We have got 58 resonance parameters up to 500 eV. The average resonance parameters, thermal cross sections and resonance integrals are presented in Table 2.2. Thermal cross sections and resonance integrals are fairly compatible with respective measured data.

Table 2.2

	ENDF/B-VI	JENDL-3	JEF-2	This evaluation
$\langle \Gamma_n^0 \rangle$ , meV	1.7418	1.2573	1.2673	1.0157
$\langle \Gamma_f \rangle$ , meV	6.9998	81.0745	79.8631	68.388
$\langle \Gamma_\gamma \rangle$ , meV	36.077	34.066	34.141	34.845
$\langle D \rangle$ , eV	13.4667	9.7308	9.5472	9.2544
$S_0 \times 10^{-4}$	1.3796	1.31696	1.3524	1.1168
$\sigma_t$ , barn	598.407	586.723	583.70	579.404
$\sigma_\gamma$ , barn	561.086	540.307	546.70	540.978
$\sigma_f$ , barn	17.0117	17.8897	17.150	16.601
$\sigma_n$ , barn	20.3092	28.5257	19.860	21.965
$g_\gamma$	0.96044	0.95979		0.96162
$g_f$	0.96058	0.96064		0.96357
$I_\gamma$ , barn	152.671	153.708	136.494	141.765
$I_f$ , barn	30.7234	32.7017	32.197	28.4497

Thermal total  $\sigma_t$ , fission  $\sigma_f$ , capture  $\sigma_\gamma$  and scattering  $\sigma_n$  cross sections,  $g_\gamma$ -, and  $g_f$ - factors, as well as resonance integrals  $I_\gamma$  and  $I_f$  values are calculated with a code INTER [18]. In case of JENDL-3 and present evaluations the multi-level Breit-Wigner formalism was used, while for ENDF/B-IV evaluation single-level formula was employed.

### 3 Unresolved resonance region

#### 3.1 Review

Unresolved resonance region of  $^{238}\text{Pu}$  is supposed to be from 0.5 keV up to 44.2667 keV. The lower energy is the end-point of resolved resonance region, the upper energy is the threshold energy of the first excited level. We suppose  $s$ -,  $p$ - and  $d$ -wave neutron-nucleus interactions to be effective.

#### 3.2 The $s$ -wave average resonance parameter evaluation

##### 3.2.1 Estimate of resonance level missing influence on $\langle D_{obs} \rangle$ and $S_0$ .

Preliminary estimates of average partial widths were obtained by averaging the evaluated resolved resonance parameters. Figure 3.1 demonstrates the cumulative sum of resolved resonance levels. The average resolved resonance parameters are as follows:

$$\begin{aligned}\langle \Gamma_n^0 \rangle &= 1.0157 \times 10^{-4} \text{ (eV)}^{1/2} \\ \langle \Gamma_f \rangle &= 34 \text{ meV} \\ \langle D_{obs} \rangle &= 9.2544 \text{ eV} \\ \langle \Gamma_\gamma \rangle &= 34.845 \text{ meV}\end{aligned}$$

Average fission width value  $\langle \Gamma_f \rangle = 34 \text{ meV}$  assumes that experimental resonance fission widths must be averaged over the fission resonance spacing in the second well, which is around 1 keV.

Due to missing of weak resonances these values overestimate neutron resonance spacing  $\langle D_{obs} \rangle$  and actual average reduced neutron width  $\langle g\Gamma_n^0 \rangle$ . To get a physically justified values of  $\langle D_{obs} \rangle$  and  $\langle g\Gamma_n^0 \rangle$  we employ a method, which is described elsewhere [19]. Both reduced neutron width and neutron resonance spacing distributions with account of missing are obtained in a unified approach. We take into account the correlation of weak resonance missing and resonance missing due to poor experimental resolution. The resolution function as well as  $\langle D_{obs} \rangle$  and  $\langle g\Gamma_n^0 \rangle$  values are obtained by maximum likelihood method when comparing experimental distributions of reduced neutron width and neutron resonance spacing with Porter-Thomas and Wigner distributions, modified for experimental resonance missing. The latter distributions are called here expected distributions.

##### 3.2.2 Evaluation of $\langle D_{obs} \rangle$ , $S_0$ , $\langle \Gamma_\gamma \rangle$ and $\langle \Gamma_f \rangle$ based on the resolved resonance parameters.

We applied our method [19] to the resolved resonance data base. The evaluated values are:

$$S_0 = (1.036 \pm 0.217) \times 10^{-4} \text{ (eV)}^{1/2}$$

$$\langle D_{obs} \rangle = (8.301 \pm 0.6) \text{ eV}$$

Figure 1 shows cumulative sum of neutron resonances. Figure 3.2 shows the cumulative sum of reduced neutron widths. Figure 3.3 shows the comparison of expected and experimental reduced neutron width distributions. Figure 3.4 shows the comparison of distributions for neutron resonance spacing. The expected distributions shown on the figures 3.3 and 3.4 demonstrate the influence of resonance missing. These figures also show that expected distributions are consistent with experimental data within statistical errors. That is the reason to consider the estimates of  $\langle D_{obs} \rangle$  and  $S_0$  reliable.

### 3.3 The s-, p- and d-wave average resonance parameter evaluation

#### 3.3.1 Neutron width

Average neutron width is calculated as follows

$$\langle \Gamma_n^{l,j} \rangle = S_l \langle D_J \rangle E_n^{1/2} P_l,$$

where  $P_l$  is the transmission factor for the  $l$ th partial wave, which was calculated within black nucleus model. The  $p$ -wave neutron strength function  $S_1 = 2.399 \times 10^{-4} \text{ (eV)}^{-1/2}$  was calculated with the optical model, using the deformed optical potential, described below. According to the results of optical model calculations  $S_0$  was assumed to decrease linearly from  $S_0 = 1.036 \times 10^{-4} \text{ (eV)}^{-1/2}$  to the value of  $S_0 = 0.968 \times 10^{-4} \text{ (eV)}^{-1/2}$  for neutron energy of 44.2667 keV. The  $d$ -wave neutron strength function was taken from optical model calculations:  $S_2 = 1.242 \times 10^{-4} \text{ (eV)}^{-1/2}$ . Since the  $d$ -wave contribution is rather small, the impact of any reasonable approximation on calculated values is negligible.

#### 3.3.2 Neutron resonance spacing

Neutron resonance spacing  $\langle D_J \rangle$  was calculated with the phenomenological model [20], which takes into account the shell, pairing and collective effects. The main parameter of the model  $\tilde{a}$  was normalized to the observed neutron resonance spacing of  $^{238}\text{Pu}$   $\langle D_{obs} \rangle = 8.301 \text{ eV}$ .

### 3.3.3 Fission width

Fission widths are calculated within a double-humped fission barrier model. We constructed transition spectra by supposing the triaxiality of inner saddle and mass asymmetry at outer saddle. Energy and angular momentum dependence of fission width is defined by the transition state spectra at inner and outer barrier humps. They will be described below. The calculated fission width for neutron incident energy of 0.5 keV equals  $\langle \Gamma_f^{1/2+} \rangle = 0.013\text{eV}$ . One must realize that due to the second well impact on fission width distribution, which can not be taken into account within ENDF/B format, fission widths values describing measured fission data at this neutron incident energies might be lower than actual fission width values. Moreover, this effect is energy dependent and the ratio of evaluated and actual fission widths decreases at low incident neutron energy. This effect tends to disappear around neutron incident energy of 45 keV.

### 3.3.4 Radiative capture width

Energy and angular momentum dependences of radiative capture width are calculated within a two-cascade  $\gamma$ -emission model with allowance for the  $(n,\gamma f)$  and  $(n,\gamma n)$  reaction competition to the  $(n,\gamma\gamma)$  reaction. In this energy region  $(n,\gamma\gamma)$  reaction appears to be a radiative capture reaction. The radiative capture width was normalized to the value of  $\langle \Gamma_\gamma \rangle = 34.845\text{ meV}$  determined for  $^{238}\text{Pu}$  in resolved resonance region. (For details see Chapter IV).

## 3.4 Cross section evaluation in the region 0.5-44.2667 keV

### 3.4.1 Fission cross section energy dependence

Fission cross section of  $^{238}\text{Pu}$  in unresolved energy region was measured by Silbert et al.[6], Budtz-Joergensen et al.[9], Alam et al.[10], Drake et al.[11] and Ermagambetov et al.[21]. One can see (fig 3.5) that experimental data are rather discrepant. Our evaluation is based on data of Alam et al.[10], reproducing measured fission cross section structure. Evaluated fission cross section values were adjusted by fitting  $\langle \Gamma_f^{1/2+} \rangle$  width.

### 3.4.2 Capture cross section energy dependence

Capture cross section of  $^{238}\text{Pu}$  is measured by Silbert et al.[13]. Since problems, which are supposed to be due to high background in that bomb-shot experiment were not solved, evaluation is based on calculated values.

### 3.4.3 Comparison of present, JENDL-3 and ENDF/B-VI evaluated data

Evaluated fission cross sections of this work is  $\sim 40\%$  lower than JENDL-3 and JEF-2 (the latter is taken from JENDL-2) at higher boundary, at lower energies our evaluation ignores structure observed by Silbert et al [6], which is adopted in JENDL-3 and JEF-2 evaluations. ENDF/B-VI evaluated fission cross section is  $\sim 30\%$  higher in this energy region except short energy interval of 10-15 keV. We keep in mind that this evaluation is too old, originating from ENDF/B-I. Figure 3.5 shows the comparison of fission cross sections  $\sigma_f$  for these evaluations. Current evaluated capture cross section  $\sigma_\gamma$  is lower than that of JENDL-3, which is  $\sim 15\%$  higher at lower edge of energy interval and almost coincides with ours at higher boundary of unresolved resonance region. ENDF/B-VI evaluated  $\sigma_\gamma$  is in good agreement with our evaluation. Comparison of the evaluated capture cross-sections is given on Fig 3.6. Comparison of the evaluated fission and capture cross-sections is given in Table 3.1 also.

Table 3.1 Comparison of the evaluated fission and capture cross-sections

Energy, keV	$\sigma_f, b$				$\sigma_\gamma, b$			
	present	J-3	JEF-2	B-VI	present	J-3	JEF-2	B-VI
0.50	2.30	1.20	1.36	3.11	7.88	9.62	1.94	7.85
0.60	2.50	1.83	1.28	2.83	6.73	8.13	7.89	6.80
0.70	2.61	2.96	6.69	2.62	5.89	6.76	9.15	6.02
0.80	2.24	2.87	3.28	2.45	5.45	6.13	5.40	5.37
1.00	1.72	1.71	1.98	2.22	4.79	5.53	4.19	4.48
1.50	1.26	1.25	1.06	1.89	3.69	4.19	1.97	3.22
2.00	1.17	1.22	1.38	1.72	3.02	3.40	2.10	3.52
2.80	1.22	1.77	2.25	1.58	2.36	2.52	2.63	2.91
4.50	0.97	0.86	0.90	1.45	1.82	2.05	1.97	2.30
5.00	0.95	1.08	1.25	1.43	1.63	1.87	1.48	2.20
6.50	0.91	1.29	1.16	1.40	1.50	1.55	1.12	1.90
10.0	0.73	0.77	0.76	1.36	1.28	1.37	1.26	1.45
11.5	0.66	0.80	0.70	0.56	1.23	1.28	1.32	1.31
15.0	0.63	0.82	0.72	0.50	1.12	1.13	0.99	1.15
20.0	0.60	0.81	0.85	0.75	1.01	1.01	0.78	0.96
25.0	0.58	0.81	0.62	0.72	0.94	0.92	0.79	0.92
35.0	0.53	0.75	0.83	0.68	0.83	0.81	0.89	0.84
40.0	0.52	0.75	0.71	0.66	0.80	0.77	0.66	0.80
44.2667	0.51	0.70	0.69	0.65	0.77	0.75	0.64	0.76

### 3.4.4 Drawbacks of ENDF/B-VI format and associated inconsistencies in neutron cross sections

Within ENDF/B-VI format number of the degrees of freedom for fission widths distributions must not exceed 4, while structure of fission barriers leads to a greater number degrees of freedom for most compound states. Distribution due to second well fission resonances can not be described within current format. To fit the data we ought to decrease the fission width value and assume rather abnormal energy dependence of fission widths.

## 4 Fast neutron cross sections

Measured neutron data in fast energy region, i.e. above  $\sim 44$  keV are available only for fission cross section. The detailed fission cross section data are available up to  $\sim 16.9$  MeV. The available fission data fit would be used as constraint for  $(n, n')$  and  $(n, \gamma)$  reaction cross sections calculation. We reproduce also the average resonance fission width within double-humped fission barrier model. To fix fission channel parameters the systematic trends are used.

### 4.1 Optical potential

The deformed optical potential for  $n+^{238}\text{Pu}$  interaction was obtained. The starting values for the potential parameters were those for  $n+^{238}\text{U}$  interaction[22]. The isotopic dependences of real and imaginary parts of the potential were calculated using the optical potential parameter systematics. We modified the original potential geometry parameters[22] to fit total cross section and differential scattering data for N-odd and -even targets above 10 MeV. This procedure of parameter fitting is well-tested in case of and  $^{233}\text{U}$ ,  $^{239}\text{Pu}$ ,  $^{235}\text{U}$ ,  $^{232}\text{Th}$  and  $^{238}\text{U}$  targets. Four levels of the ground state rotational band  $(0^+, 2^+, 4^+, 6^+)$  are coupled. Deformations parameter of the potential  $\beta_2, \beta_4$  were adjusted to fit evaluated  $S_0$  value. The potential parameters are as follows:

$$W_D = \begin{cases} V_R = 46.26 - 0.3E, \text{ MeV}, r_R = 1.26 \text{ fm}, a_R = 0.615 \text{ fm} \\ 3.63 + 0.4E, \text{ MeV}, & E \leq 10 \text{ MeV}, r_D = 1.24 \text{ fm}, a_D = 0.5 \text{ fm} \\ 7.63 \text{ MeV}, & E > 10 \text{ MeV} \end{cases}$$

$$V_{SO} = 6.2 \text{ MeV}, r_{SO} = 1.12 \text{ fm}, a_{SO} = 0.47 \text{ fm}, \beta_2 = 0.197, \beta_4 = 0.061$$

The  $s$ -,  $p$ -, and  $d$ -wave strength functions and potential scattering cross section, calculated with this potential parameters in a coupled channel approach at incident neutron energy of 0.5 keV are:

$$S_0 = 1.036 \times 10^{-4} (\text{eV})^{-1/2}, \quad P' = 9.238 \text{ fm}$$



and at 44.2667 keV are:

$$S_0 = 0.968 \times 10^{-4}(\text{eV})^{-1/2} \quad S_1 = 2.399 \times 10^{-4}(\text{eV})^{-1/2} \quad S_2 = 1.242 \times 10^{-4}(\text{eV})^{-1/2}$$

The  $^{238}\text{Pu}$  reaction cross sections, calculated with deformed optical potential and spherical optical potential, which is used in JENDL-3 evaluation, are compared on fig. 4.1. The significant differences below 1 MeV and above 10 MeV would be manifested in inelastic scattering cross section and  $(n, 3n)$  cross section. The total and elastic scattering cross sections also appear to be rather different (see figs.4.2, 4.3).

## 4.2 Fission cross section

### 4.2.1 Status of the experimental data

Besides measurements described in Chapter "Resolved resonance region" fission cross section was measured by the following authors.

Fission cross section ratio of  $^{238}\text{Pu}$  and  $^{235}\text{U}$  was defined by Fomushkin et al. [23] in the range of incident neutron energies from 0.45 MeV to 3.62 MeV. They have used mica detectors. The sample weight was defined using  $T_{\alpha 1/2} = 87.48$  years, renormalization of their results to new value of  $T_{\alpha 1/2} = 87.75$  years changes original values only slightly.

Fission cross section was measured by Ermagambetov et al. [24] relative to  $^{235}\text{U}$  and  $^{238}\text{U}$  from 0.5 up to 16.9 MeV. Sample weight was defined in thermal flux. Data should be renormalized to new values of  $^{235}\text{U}$  and  $^{238}\text{U}$  fission cross sections [25, 26]. Subthreshold fission cross section of  $^{238}\text{Pu}$  was measured by Ermagambetov et al. [21] relative to fission cross section of  $^{235}\text{U}$ . Fission fragments were registered with glass detectors. The absolute values were normalized to the fission cross section values of previous measurement [24].

Fission cross section ratio to  $^{235}\text{U}$  and  $^{238}\text{U}$  at incident neutron energy of 2.9 MeV was measured by Aleksandrov et al. [27], fission fragments were registered with glass detector.

Fission cross section ratio to  $^{238}\text{U}$  and  $^{237}\text{Np}$  was measured at 14.5 MeV by Fomushkin et al. [28], when renormalized to recent values of  $^{238}\text{U}$  and  $^{237}\text{Np}$  fission cross section, the resulting value is compatible with data by Ermagambetov et al. [24].

The data by Budtz-Jørgensen et al. [9] are consistent with data by Barton and Koonts [14], Ermagambetov and Smirenkin [21, 24], Fomushkin et al. [23] within experimental errors.

The data by Alam et al. [10] are available up to 100 keV. The data by Budtz-Jørgensen et al. [9] cover the incident neutron energy region from 0.1 eV up to 10 MeV. Below 100 keV they are rather discrepant with data

by Alam et al. [10]. Both data sets predict different fission cross section shapes, data by Budtz-Jorgensen et al.[9] being systematically higher than former data (see fig.4.4). Another set of data by Ermagambetov et al. [21], when renormalized properly, appears to be consistent with data by Alam et al.[10] below 100 keV (see fig. 4.4). Above 1 MeV available data sets are compatible within errors (see figs. 4.5, 4.6).

#### 4.2.2 Statistical model calculation of fission cross section

We choose to fit data Alam et al. [10] below 100 keV. At higher neutron energies we will follow basically the trend of data by Budtz-Jorgensen et al. [9]. The most peculiar feature of data base is the step-like structure around 1 MeV, i.e. just above fission threshold and decreasing trend of data above  $\sim 2.5$  MeV incident neutron energies. Structure of the same kind is evident in  $^{240}\text{Pu}$  neutron-induced fission cross section [29]. Both features would be reproduced within the statistical model calculations. To describe the step-like structure above 1 MeV, we assume it to be due to interplay of level densities of even-odd  $^{239}\text{Pu}$  fissioning nuclide and even-even  $^{238}\text{Pu}$  residual nuclide.

The comparison of calculated fission cross section with measured data is shown in figs. 4.4, 4.5 and 4.6. The statistical theory calculation of fission cross section was accomplished within the double-humped fission barrier model. The approach employed in code STAT [30] is described in more details elsewhere [31, 32]. The procedure of calculating fission transmission coefficients is briefly described below.

#### 4.2.3 Fission transmission coefficient, level density and transition state spectrum

The different behavior of level densities of even-even and even-odd nuclei at low excitation energies should be taken into account. The one-quasiparticle neutron states of even-odd  $^{239}\text{Pu}$  fissioning nuclide, lying below the three-quasiparticle states excitation threshold define the shape of  $^{238}\text{Pu}(n,f)$  fission cross section below incident neutron energy of  $\sim 1.5$  MeV. At higher excitation energies three-quasiparticle states are excited. Each one-quasiparticle state is assumed to have a rotational band built on it with a rotational constant, dependent upon the respective saddle deformation. These levels comprise the discrete transition spectra at both saddles. We construct the discrete transition spectra up to 100 keV, using one-quasiparticle states of Bolsterli et al. [33] (see Table 4.1). At higher excitation energies the continuous level densities are used.

The discrete transition spectra, as well as continuous level contribution to the fission transmission coefficient are dependent upon the order of symmetry for  $^{239}\text{Pu}$  fissioning nucleus at inner and outer saddles. Due to the

axial asymmetry at the inner saddle [34] we additionally assume  $(2J+1)$  rotational levels for each  $J$  value. The negative parity bands  $K^\pi = 1/2^-, 3/2^-, 5/2^- \dots$  at outer saddle are assumed to be doubly degenerate due to mass asymmetry [34]. With transition state spectra thus defined (see Table 4.1) the fission barrier parameters are obtained (see table 4.2). The fission width  $\Gamma_f^{1/2+} = 0.013$  eV calculated at incident neutron energy of 0.5 keV coincides with average fission width obtained in unresolved resonance region.

The generalized pairing model provides the means of taking into account the discrete character of few-quasiparticle excitations. It was shown to be important in case of even-even fissioning nucleus  $^{236}\text{U}$  in the  $^{235}\text{U}(\text{n.f})$  reaction [31]. However that is a general effect, which is evident in neutron-induced fission cross sections of even-even, Z-even, N-odd and odd-odd target nuclei [29]. We will model the discrete few-quasiparticle excitation effects in level density in the following approximate way. The level density of axially symmetric fissioning nucleus is calculated in constant temperature approximation, i.e.  $\rho(U) = T_f^{-1} \exp((U - U_o)/T_f)$ . The respective parameters, nuclear temperature  $T_f$  and excitation energy shift  $U_o$  are defined at the matching energy  $U_c = 2.4$  MeV. At excitation energies above  $U_c$  the continuum part of the transition state spectrum is represented with the phenomenological model [20], which takes into account pairing, shell and collective effects at saddle deformations. The asymptotic value of the main parameter of the level density for fissioning nucleus  $^{239}\text{Pu}$  is assumed to be the same, as that of  $^{239}\text{Pu}$  compound nuclide. Then the effects of non-axiality and mass asymmetry are included. The detailed procedure of calculating fission transmission coefficient is described elsewhere [31, 32]. The respective parameters: shell correction at saddles  $\delta W$ , pairing correlation function  $\Delta$ , quadrupole deformation  $\epsilon$ , and momentum of inertia at zero temperature  $F_0/\hbar^2$  are given in Table 4.3.

The threshold energies for the excitations of few-quasiparticle states are calculated within generalized pairing model [20] using closed-form equations by Fu [35]. The procedure is described in more detail elsewhere [36]. In case of even-odd nuclei the nuclear level density  $\rho(U)$  up to the three-quasiparticle excitation threshold depends on the excitation energy only weakly, since the intrinsic state density is constant. In this excitation energy region we will model the level density as  $\rho(U) \simeq T_f^{-1} (1 + 2(U - 0.5U_3)) \exp((\Delta_f - U_o)/T_f)$ . Above the three-quasiparticle states excitation threshold the constant temperature model is used. The one- and three-quasiparticle states level density of even-odd fissioning nucleus  $^{239}\text{Pu}$  defines the fission cross section shape at incident neutron energies below  $\sim 2.5$  MeV (see fig. 4.5). Above  $\sim 2.5$  MeV incident neutron energy fission cross section data were fitted (see fig. 4.6) by slight increase of pairing correlation function value. The parameters used for calculation of residual nuclide  $^{238}\text{Pu}$  level density for neutron emission

competition are described below.

Table 4.1

Transition spectra band-heads of  $^{239}\text{Pu}$

inner saddle		outer saddle	
$K^\pi$	$E_{K^\pi}$ , MeV	$K^\pi$	$E_{K^\pi}$ , MeV
$1/2^+$	0.0	$1/2^+$	0.0
$5/2^+$	0.08	$1/2^-$	0.0
$1/2^-$	0.05	$3/2^+$	0.08
$3/2^-$	0.0	$3/2^-$	0.08
		$5/2^+$	0.0
		$5/2^-$	0.0

Table 4.2

Fission barrier parameters

Nucleus	Barrier	Barrier height, MeV	Curvature, MeV
$^{239}\text{Pu}$	inner	6.325	0.75
$^{239}\text{Pu}$	outer	5.70	0.6
$^{238}\text{Pu}$	inner	5.60	0.9
$^{238}\text{Pu}$	outer	5.10	0.6
$^{237}\text{Pu}$	inner	6.00	0.8
$^{237}\text{Pu}$	outer	5.80	0.6
$^{236}\text{Pu}$	inner	5.60	0.9
$^{236}\text{Pu}$	outer	5.10	0.6

Table 4.3

Level density parameters of  $^{239}\text{Pu}$  fissioning nucleus and residual nucleus  $^{238}\text{Pu}$

Parameter	inner saddle	outer saddle	neutron channel
$\delta W$ , MeV	2.5	0.6	-2.439
$\Delta$ , MeV	$\Delta_0 + 0.06$	$\Delta_0 + 0.06$	$\Delta_0$
$\epsilon$	0.6	0.8	0.24
$F_0/\hbar^2$ , $\text{MeV}^{-1}$	100	200	73

Below incident neutron energy of 1.14 MeV the neutron cross sections are calculated within Hauser-Feshbach approach with a width fluctuation correction taken into account. For width fluctuation correction calculation

only Porter-Thomas fluctuations are taken into account. Effective number of degrees of freedom for fission channel is defined at the higher (inner) saddle as  $\nu_f^{\mathcal{J}\pi} = T_f^{\mathcal{J}\pi} / T_{f\text{max}}^{\mathcal{J}\pi}$ , where  $T_{f\text{max}}^{\mathcal{J}\pi}$  is the maximum value of the fission transmission coefficient  $T_f^{\mathcal{J}\pi}$ . Above incident neutron energy of 1.14 MeV the Tepel et al. [37] approach is employed.

#### 4.2.4 Fission cross section above emissive fission threshold

The first chance fission cross section of  $^{238}\text{Pu}(\text{n},\text{f})$  reaction above the emissive fission threshold is fixed with the level density and fission barrier parameters systematics [31, 32] ( see Tables 4.2, 4.3) and secondary neutron spectra parameterization [41] (see fig. 4.6). A consistent description of a complete set of measured data on (n,f), (n,2n) and (n,3n) for  $^{238}\text{U}$  and  $^{235}\text{U}$  targets was accomplished with the secondary neutron spectra parameterization [41], which is used here.

The fission barrier parameters of  $^{238}\text{Pu}$  are fixed by  $^{237}\text{Pu}(\text{n},\text{f})$  inferred data [38] description. Figure 4.7 shows the  $^{238}\text{Pu}(\text{n},\text{f})$  measured data description. We modelled the fissioning even-even nuclide  $^{238}\text{Pu}$  nuclear level density  $\rho(U)$  above the pairing gap up to the four-quasiparticle excitation threshold as  $\rho(U) = \rho(\bar{U}) / (1 + \exp(U_2 - U + \delta_1) / \delta_2)$ . The two-quasiparticle states level density of even-even fissioning nucleus  $^{238}\text{Pu}$  defines the fission cross section shape at incident neutron energies  $\sim 0.5 \div 2 \text{ MeV}$  (see fig. 4.8), the parameters  $\bar{U} = 1.7 \text{ MeV}$ ,  $\delta_1 = \delta_2 = 0.2 \text{ MeV}$  are fixed by analysis of fission data for U and Pu target nuclei.

The fission barrier parameters of  $^{237}\text{Pu}$  are fixed by the  $^{236}\text{Pu}(\text{n},\text{f})$  reaction data [39, 40] and inferred data by Britt et al.[38] analysis. The fig.4.9 shows the  $^{236}\text{Pu}(\text{n},\text{f})$  data description.

The calculated fission cross section is rather different from previous evaluated curves above (n,nf) reaction threshold (see figs. 4.10). The calculated fission cross section at  $\sim 15 \text{ MeV}$  neutron energy appears to be consistent with data by Ermagambetov and Smirenkin [24] (see fig. 4.7). The discrepancy of the calculated cross section with data by Budtz-Jorgensen et al. [9] appears unavoidable, since the measured data are just as high as reaction cross section around 10 MeV, so they are incompatible with the calculated fission cross section.

### 4.3 Inelastic scattering cross section

The inelastic scattering cross section is calculated with the statistical codes STAT [30] and STAPRE [42]. The discrete level excitation (compound and direct), continuum excitation and pre-equilibrium emission contribute to the inelastic scattering cross section.

#### 4.3.1 Levels of $^{238}\text{Pu}$

The low-lying levels of scheme of Nuclear Data Sheets [43] (see table 4.4) appears incomplete at excitation energy above 1.14 MeV (see fig. 4.11). In JENDL-3 evaluation there are 29 discrete excited levels up to 1.636 MeV, i.e. the missing of levels above  $\sim 1.14$  MeV is ignored (see figs. 4.12, 4.13).

Table 4.4

Level scheme of  $^{238}\text{Pu}$

$E_{K\pi}^J$ , MeV	$J$	$\pi$	$K$	band
0.000	0	+	0	A
0.04408	2	+	0	A
0.14598	4	+	0	A
0.3034	6	+	0	A
0.5134	8	+	0	A
0.60518	1	-	0	B
0.66143	3	-	0	B
0.76320	5	-	0	B
0.7728	10	+	0	A
0.9415	0	+	0	C
0.96277	1	-	1	D
0.9681	2	-	1	D
0.9831	2	+	1	C
0.98546	2	-	0	A
1.02855	2	+	2	D
1.06995	3	+	1	C
1.0785	12	+	2	A
1.08257	4	-	2	D
1.1258	4	+	0	E
1.1340	0	+	2	B

#### 4.3.2 $^{238}\text{Pu}$ level density

The continuum level density below excitation energy  $U_c = 3.6$  MeV is calculated with the constant temperature model

$$\rho(U) = T^{-1} \exp((U - U_0)/T),$$

here, energy shift  $U_0 = -0.0002$  MeV, nuclear temperature  $T = 0.38454$  MeV are the constant temperature model parameters. . The cumulative number

of observed levels is compared with constant temperature approximation on fig. 4.11. At higher excitation energies the phenomenological model [20] is used. The main level density model parameter  $a$  for  $^{238}\text{Pu}$  residual nucleus is obtained by systematics [44].

The generalized pairing model provides the means of taking into account the discrete character of few-quasiparticle excitations just above the pairing gap. It was shown to be important in case of even-even residual nucleus  $^{238}\text{Pu}$  in the  $^{239}\text{Pu}(n,2n)$  reaction [36]. We modelled the nuclear level density  $\rho(U)$  above the pairing gap  $U_2$  up to the four-quasiparticle excitation threshold  $U_4$  as  $\rho(U) = \rho(U_4 - 0.1)/(1 + \exp((U_2 - U + \delta_1)/\delta_2))$ . The two-quasiparticle states level density of even-even residual nuclide  $^{238}\text{Pu}$  influences the fission cross section shape at incident neutron energies above  $\sim 1.4\text{MeV}$ , the parameters,  $\delta_1 = \delta_2 = 0.1\text{ MeV}$  values were extracted. Below the pairing gap the collective levels were employed.

#### 4.3.3 $^{239}\text{Pu}$ level density

The level density of even-odd compound nuclide  $^{239}\text{Pu}$  one needs to calculate radiative capture width and  $(n,\gamma')$  reaction contribution to the compound inelastic scattering cross section. The continuum level density below excitation energy  $U_c = 2.4\text{ MeV}$  is calculated with the constant temperature model, the constant temperature model parameters are: energy shift  $U_0 = -0.65658\text{ MeV}$ , nuclear temperature  $T = 0.36845\text{ MeV}$ . The cumulative number of observed levels is compared with constant temperature approximation on fig. 4.14. At higher excitation energies the phenomenological model [20] is used. The main model parameter  $\tilde{a}$  for  $^{239}\text{Pu}$  residual nucleus is obtained by fitting the evaluated neutron resonance spacing of  $^{238}\text{Pu}$  target nuclide  $\langle D_{obs} \rangle = 8.301\text{ eV}$ .

#### 4.3.4 Compound inelastic scattering

The residual nucleus  $^{238}\text{Pu}$  level density modelling, adopted in present work changes the inelastic scattering cross section below 5 MeV as compared with ENDF/B-VI, JEF-2 and JENDL-3.2 evaluations. The most close to our estimate is that of JEF-2 evaluation (see figs. 4.12, 4.13, 4.15-4.20). However the discrepancies still remain in the range 1-5 MeV and above 10 MeV. Above  $\sim 1.5\text{ MeV}$  incident neutron energy the discrepancies are due to direct excitation of the ground state band levels. Above 1 MeV incident neutron energy inelastic scattering to the continuum gives a major contribution to the total inelastic scattering cross section (see fig. 4.13). Above 5 MeV incident neutron energy pre-equilibrium emission and direct inelastic scattering are the two reaction mechanisms which define inelastic scattering cross section (see fig. 4.12). The pre-equilibrium model parameters were

tested by the statistical model description of  $^{238}\text{U}+n$  interaction secondary neutron spectra and consistent description of fission and  $(n,xn)$  reaction data for major actinides [41]. Steep decrease of inelastic scattering cross section of JENDL-3 above 5 MeV (see fig. 4.12) is due to missing of pre-equilibrium emission of neutrons.

#### 4.3.5 Direct inelastic scattering

The direct inelastic scattering changes the shape of ground state band levels excitation cross sections above 1 MeV incident neutron energy (see figs. 4.15 - 4.20). This mechanism defines partly the hard-energy tail in total inelastic scattering cross section (see fig. 4.13).

### 4.4 Radiative capture cross section

The radiative capture cross section is calculated within a statistical approach up to 5 MeV. Radiative capture strength function equals  $S_{\gamma 0} = 41.977$ . At higher incident neutron energies we assume radiative capture cross section to be 1 mbarn. The radiative capture width was calculated with  $(n,\gamma f)$  and  $(n,\gamma n')$  reactions competition against "true" capture reaction  $(n,\gamma\gamma)$ . Due to low fission threshold for  $^{239}\text{Pu}$  compound nuclide the competition of  $(n,\gamma f)$  reaction is stronger than that of  $(n,\gamma n')$  reaction. The influence of  $(n,\gamma n')$  and  $(n,\gamma f)$  reaction competition on radiative capture cross section is illustrated on fig.4.21 by sharp decrease of capture cross section above 1 MeV incident neutron energy, as compared with  $(n,\gamma x)$  reaction cross section. Present capture cross section shape and that of JENDL-3.2 are rather similar.

### 4.5 Cross sections of $(n,2n)$ and $(n,3n)$ reactions

Current and JENDL-3 evaluated  $(n,2n)$  and  $(n,3n)$  cross sections are drastically different. The magnitude of  $(n,2n)$  cross section below the  $(n,2nf)$  reaction threshold is defined by  $(n,nf)$ ,  $(n,n\gamma)$  and  $(n,2n)$  reaction competition. Present and JENDL-3 evaluated fission cross sections are rather different, as well as reaction cross sections above 10 MeV incident neutron energy (see fig. 4.1). To calculate the  $(n,2n)$  reaction cross section we use an approach, developed for description of the  $^{238}\text{U}(n,2n)$  reaction cross section [41]. The present and previous evaluations are compared in fig. 4.22. There is no hard-energy tail in  $(n,2n)$  reaction cross sections of JENDL-3 evaluation. In case of  $(n,3n)$  reaction the difference in reaction cross section above 11 MeV (see fig. 4.1) contributes essentially to the discrepancy, shown on fig. 4.23.



## 5 Energy distributions of secondary neutrons

There is no measured data on secondary neutron spectra. To calculate neutron energy distributions of  $(n, xn\gamma)$  and  $(n, xnf)$ ,  $x=1, 2, 3$  reactions we use a simple Weisskopf-Ewing evaporation model [45] taking into account fission and gamma competition to neutron emission. The pre-equilibrium emission of first neutron is included.

### 5.1 Model calculations of $(n, nx)$ reaction spectra

The first neutron spectra for the  $(n, nx)$  reaction is the sum of evaporated and pre-equilibrium emitted neutron contributions. The pre-equilibrium emission contribution is calculated with a parameter systematics tested in case of  $n+^{238}\text{U}$  and  $n+^{235}\text{U}$  interactions [41]. We have calculated the 1st, 2nd and 3d neutron spectra for the  $(n, n\gamma)$ ,  $(n, 2n)$  and  $(n, 3n)$ , where applicable. According to the ENDF/B-VI format we included the secondary neutron spectra in the following way. The calculated spectra were summed up and tabular spectra for the  $(n, n\gamma)$ ,  $(n, 2n)$  and  $(n, 3n)$  reactions were obtained. To clarify the competition of neutron,  $\gamma$ -emission and fission in case of  $(n, nx)$  and  $(n, 2nx)$  reactions we have chosen the following presentation of spectra. Figure 5.1 shows the spectrum of 1st neutron of the reaction  $(n, nx)$  and its partial contributions for  $(n, n\gamma)$ ,  $(n, 2n)$ ,  $(n, nf)$ ,  $(n, 2nf)$  and  $(n, 3n)$  reactions. Figure 5.2 shows the spectrum of 2nd neutron of the reaction  $(n, 2nx)$  and its partial contributions for  $(n, 2n)$ ,  $(n, 3n)$  and  $(n, 2nf)$  reactions. The spectra of 1st and 2nd neutrons are normalized to unity. The partial neutron spectra shown on figs. 5.1, 5.2 are normalized to the contributions of appropriate cross sections to the  $(n, nx)$  and  $(n, 2nx)$  reaction cross sections, respectively.

The inclusion of pre-equilibrium emission changes significantly the average energies of emitted neutron spectra. That is shown in Table 5.1, where the average secondary neutron energies for current ENDFB-VI and JENDL-3 evaluations are compared. The most significant is the change of neutron spectra of  $(n, n\gamma)$  reaction. Figures 5.3-5.7 demonstrate the discrepancies of secondary neutron spectra in current and JENDL-3 evaluations.

The 1st neutron spectra of  $(n, nf)$  reaction also becomes harder and that influences prompt fission neutron spectra. On the other hand, the spectra of 2nd and 3d neutrons become softer.

Table 5.1 Average energies of secondary neutron spectra

$E_n$ , MeV	1st neutron average energy, MeV									
	(n, n')			(n, 2n)			(n, n'f)	(n, 3n)		(n, 2n'f)
	pres.	B-VI	J - 3	pres.	B-VI	J - 3	pres.	pres.	J - 3	pres.
2.0	0.42	0.45	0.21							
8.0	3.87	1.19	1.06	0.43	0.20	0.54	1.17			
14.0	9.97	1.56	1.44	3.20	1.08	1.43	3.01	0.36	0.62	0.81
20.0	16.0	1.85	1.73	9.47	1.48	1.73	4.50	2.84	1.71	3.24

$E_n$ , MeV	2nd neutron average energy, MeV						3d neutron	
	(n, 2n)			(n, 3n)		(n, 2n'f)		
	pres.	B-VI	J - 3	pres.	J - 3	pres.	pres.	J - 3
8.0	0.14	0.55	0.48					
14.0	0.75	1.55	0.90	0.32	0.57	0.59	0.10	0.51
20.0	0.74	1.85	1.31	1.09	1.31	1.08	0.59	0.70

## 5.2 Prompt fission neutron spectra

Prompt fission neutron spectra were calculated with the account of pre-fission neutron emission above emissive fission threshold .

### 5.2.1 Prompt fission neutron spectra evaluation

Prompt fission neutron spectra are calculated involving Watt[46] formula with the parameters given in Table 5.2. Approach employed by Watt assumes neutron evaporation from fully accelerated fission fragments.

Above emissive fission threshold the fission neutron spectra  $N(E, E_n)$  is the superposition of emissive fission spectra, i.e.

$$\begin{aligned}
 N(E, E_n) = & \left( \frac{\sigma_{nF}}{\sigma_{nF}} \nu_1(E_n) N_1(E, E_n) + \frac{\sigma_{nn'f}}{\sigma_{nF}} [\Phi_{nn'f}(E, E_n) + \nu_2(E_n) N_2(E, E_n)] \right. \\
 & + \frac{\sigma_{n2n'f}}{\sigma_{nF}} [\Phi_{n2n'f}^1(E, E_n) + \Phi_{n2n'f}^2(E, E_n) + \nu_3(E_n) N_3(E, E_n)] \Big) / \\
 & \left[ \frac{\sigma_{nF}}{\sigma_{nF}} \nu_1(E_n) + \frac{\sigma_{nn'f}}{\sigma_{nF}} (1 + \nu_2(E_n)) + \frac{\sigma_{n2n'f}}{\sigma_{nF}} (2 + \nu_3(E_n)) \right],
 \end{aligned}$$

where  $\sigma_{nF}$ ,  $\sigma_{nn'f}$ ,  $\sigma_{n2n'f}$  are the total and i-th chance fission cross sections ( $i = 1, 2, 3$ );  $\Phi_{nn'f}$ ,  $\Phi_{n2n'f}^1$ , and  $\Phi_{n2n'f}^2$  are emitted neutron spectra; for

(n,nf) reaction. 1st and 2nd neutrons of (n,2nf) reaction, respectively;  $\nu_i$  and  $N_i$  are multiplicity and prompt neutron spectra for the  $i$ -th fissioning nucleus. Prompt neutron multiplicities  $\nu_i$  are described in Chapter 6. Average neutron energy dependences of prompt neutron spectra for the  $i$ -th fissioning nucleus  $N_i(E, E_n)$  were calculated using assumption by Terrell[47]  $\overline{E}_i = a + b\sqrt{1 + \nu_i(E_n)}$  (for parameters see Table 5.2). The pre-equilibrium emission of the first neutron is included, the  $\Phi_{n,nf}^i$  spectra for the emissive fission are calculated with Weisskopf-Ewing evaporation model [45].

Table 5.2

Parameters  $a$  and  $b$  of Terrell' systematics

Fissioning nucleus	$a$ , MeV	$b$ , MeV
$^{239}\text{Pu}$	0.75	0.645
$^{238}\text{Pu}$	0.75	0.645
$^{247}\text{Pu}$	0.75	0.645

Figure 5.8 shows the comparison of calculated prompt fission neutron spectra involving maxwellian and Watt spectrum with the same average energies of neutrons. The maxwellian spectrum overestimates number of emitted neutrons below 1 MeV and above 6 MeV emitted neutron energies. Average energies of fission spectrum for thermal neutron-induced fission predicted with the adopted parameters are 2.014 MeV for  $^{239}\text{Pu}$ , 2.017 MeV for  $^{238}\text{Pu}$  and 2.012 MeV for  $^{247}\text{Pu}$ . They are compatible with evaluated value of 2.022 MeV in JENDL-3, however the spectra shapes are significantly different. Figure 5.9 demonstrates the differences between our spectra taking into account pre-fission neutrons and those calculated using Watt formula with the same average energy of emitted neutron. Large differences can be found above 3 MeV emitted neutron energies. Figures 5.10-5.12 show the partial contributions of  $i$ -th chance fission to the total fission neutron spectrum at incident neutron energies of 6, 14 and 20 MeV. Table 5.3 gives comparison of average neutron energies for our JENDL-3 and ENDFB-VI evaluations. Our estimate of average fission spectrum energy almost coincides with JENDL-3 and is much higher than that of ENDF/B-VI at high neutron incident energies. Both JENDL-3 and ENDF/B-VI evaluation use simple maxwellian approximation for fission spectra, without taking into account emission of pre-fission neutrons. Differences which may arise because of this simplification are shown on Fig. 5.9

Table 5.3 Comparison of average fission spectra energies for different evaluations.

$E_n$ , MeV	Present	JENDL-3	ENDF/B-VI
Thermal	2.014	2.022	1.995
1.0	2.036	2.046	1.995
5.0	2.120	2.138	1.995
10.0	2.176	2.244	1.995
15.0	2.310	2.345	1.995
20.0	2.472	2.438	1.995

## 6 Number of neutrons per fission

There are no experimental data on number of prompt fission neutrons  $\nu_p$  for  $^{238}\text{Pu}$  except thermal values measured by Jaffey et al.[48] and Zamyatnin et al.[49]. We adopted thermal value  $\nu_p^{238} = 2.84$  for  $^{238}\text{Pu}$  using normalization procedure by Malinovski[50]. Numbers of prompt fission neutrons  $\nu_p$  for neutron-induced fission of  $^{237}\text{Pu}$  and  $^{236}\text{Pu}$  were taken from systematics[52] and are 2.86 and 2.83, respectively. The systematics by Howerton[51], used in JENDL-3 and ENDF/B-6 evaluations gives steep increase of  $\nu_p$  with excitation energy (fig. 6.1). In present approach we assume that below emissive fission threshold energy dependence of number of neutrons per fission on the excitation energy has a slope  $d\nu_p/dE = 0.14 \text{ MeV}^{-1}$ . When calculating excitation energies  $E$  of emerging nuclei we took into account binding and average kinetic energies of pre-fission neutrons. The comparison of  $\nu_p(E)$ , calculated with fixed parameters, with JENDL-3 and ENDF/B-VI evaluations is shown in fig. 6.1. The adopted slope of  $d\nu_p/dE = 0.14$  is considerably lower than that of Howerton systematics[51] prediction, adopted in JENDL-3 and ENDF/B-VI. However, it is consistent with  $d\nu_p/dE$  for neighboring nuclei. Our calculations predict non-linear shape of  $\nu_p(E)$  above emissive fission threshold. The influence of pre-equilibrium pre-fission neutrons manifests as additional appreciable decrease of  $d\nu_p/dE$  above 12 MeV.

The delayed number of neutrons per fission  $\nu_d$  is taken from systematics by Tuttle[53]. Specifically,  $\nu_d = 0.0047$  for incident neutron energies up to 6 MeV and  $\nu_d = 0.0032$  for  $E_n \geq 8\text{MeV}$ . Both values are linearly connected between 6 and 8 MeV. The decay constants for six groups of delayed neutrons are taken from Brady et al.[54]

## 7 Angular distributions of secondary neutrons

The angular distributions of elastically scattered neutrons and those for neutrons, scattered on four levels of ground state band are calculated with the coupled channel method. The isotropic compound scattering contribution is taken into account by renormalizing l-th Legendre polynomial coefficients  $A_l^{cc}$ , calculated with coupled channels:

$$A_l = A_l^{cc} \sigma_{dir} / (\sigma_{dir} + \sigma_{comp}),$$

where  $\sigma_{dir}$  and  $\sigma_{comp}$  are the scattering cross section direct and compound contributions, respectively. For the other contributing reactions angular distributions of secondary neutrons are assumed isotropic.

## 8 Conclusions

The evaluated neutron data file for  $^{238}\text{Pu}$  is compiled in ENDF/B-VI format and sent to the International Science and Technology Center (Moscow) and Japan Nuclear Data Center at Japan Atomic Energy Research Institute.

The scarcity of experimental data coupled with possibility of some new data becoming available may urge some revision of data file. Present version of  $^{238}\text{Pu}$  data file may be revised before March of 1998, the expiration date of Project CIS-03-95.

## References

- [1] Nakagawa T., Kikuchi Y., Proc. of the Int. Conf. on Nuclear Data and Technology, Gatlinburg, Tenn., USA, 9-13 May, 1994, Dickens J.K. (Editor), 709, ANS Inc., 1994.
- [2] Japanese Evaluated Data Library, Version 3, JAERI 1319, 1990.
- [3] Dunford C.L. Nuclear Data for Science and Technology, Proc. Int. Conf. Julich, 1991, 788, Springer-Verlag, 1992, Berlin.
- [4] Derrien H. Proc. Int. Conf. Nuclear Data for Science and Technology, Antwerpen, Belgium, September 6-10, 1982, p. 669, D/ Reidel Publishing Co., Boston (1983).
- [5] Young T.E., Simpson F.B., Berreth J.R., Coops M.S. Nucl. Sci. Engng. 30, 355 (1967).

- [6]Silbert M.G., Moat A., Young T.E. Nucl. Sci. Eng. 52, 176 (1973)
- [7]Mughabghab S.F. Neutron Cross Sections, vol. 1, Part B, Academic Press, 1984.
- [8]Stubbins W.F., Bowman C.D., Auchampaugh G.F., Coops M.F. Phys. Rev. 154, 1111 (1967).
- [9]Budtz-Jørgensen C., Knitter H.-H. and Smith D.L. Proc. Int. Conf. Nuclear Data for Science and Technology, Antwerpen, Belgium, September 6-10, 1982, p. 206, D/ Reidel Publishing Co., Boston (1983).
- [10]Alam B., Block R.C., Slovacek R.E., Hoff R.W. Nucl. Sci. Eng. 99, 267 (1988).
- [11]Drake D.M., Bowman C.D., Coops M.S., et.al., Rep. LA-4420 (1970)
- [12]Gerasimov V.F. Sov. J. Nucl. Phys., 4, 706 (1967).
- [13]Silbert M.G., Berreth Nucl. Sci. Eng. 52, 187 (1973)
- [14]Barton D.M. and Koontz P.G. Phys. Rev., 162, 1070 (1967).
- [15]Butler D.K., Sjoblom Bull. Amer. Phys. Soc, 8, 369 (1963).
- [16]Davey W.G. Nucl. Sci. Eng., 26, 149 (1966).
- [17]Wagemans C. and Deruytter A.J., Proc. IAEA Advisory Group Meeting 'Nuclear Standards Reference Data ', Geel, Belgium, November, 1984, IAEA-TECDOC-335, p. 156, IAEA, Vienna (1985).
- [18]Dunford C.L.: "ENDF Utility Codes Release 6.9", IAEA-NDS-29 (1993).
- [19]Porodzinskij Yu.V., Sukhovitskij E.Sh., Nuclear Constants, 4, p.27, 1987 (in Russian).
- [20]Ignatjuk A.V., Istekov K.K., Smirenkin G.N. Sov. J. Nucl. Phys. 29, 450 (1979)
- [21]Ermagambetov S.B., Smirenkin G.N. JETP Letters, 9, 309 (1969).
- [22]Haouat, Lachkar J., Lagrange Ch., et al., Nucl.Sci. Engng. 81, 491 (1982).
- [23]Fomushkin E.F., Gutnikova E.K. Sov. J. Nucl. Phys. 10, 529 (1970).
- [24]Ermagambetov S.B., Smirenkin G.N. Sov. At. Energy, 25, 1364 (1969).
- [25]Sowerby M.G. Nuclear Data Standards for Nuclear Measurements, NE-ANDC - 311 'U', INDC(SEC)-101, 1992, p.51.

- [26]Y. Kanda, Y. Nakajima. Nuclear Data Standards for Nuclear Measurements, NEANDC - 311 'U', INDC(SEC)-101, 1992, p.70.
- [27]Aleksandrov B.M., Solovjev S.M., Soloshenkov P.S. et al. Nuclear Constants, 1(50), p.3, 1983 (in Russian).
- [28]Fomushkin E.F., Gutnikova E.K., Zamyatnin Yu.S. et al. Sov. J. Nucl. Phys. 5, 966 (1967).
- [29]Maslov V.M. Int. Conf. Nuclear Data for Science and Technology, Trieste, Italy, May 19-24, 1997, to be published.
- [30]Klepatskij A.B., Maslov V.M., Sukhovitskij E.Sh., private communication.
- [31]Ignatjuk A.V., Maslov V.M., Proc. Int. Symp. Nuclear Data Evaluation Methodology, Brookhaven, USA, October 12-16, 1992, p.440, World Scientific, 1993.
- [32]Maslov V.M., Kikuchi Y. JAERI-Research 96-030, June, 1996.
- [33]Bolsterli M., Fiset E.O., Nix J.R., Norton J.L. Phys.Rev., C 5, 1050 (1972).
- [34]Howard W.M., Moller P. Atomic Data and Nuclear Data Tables, 25, 219 (1980).
- [35]Fu C. Nucl. Sci. Engng. 86, 344 (1984).
- [36]Maslov V.M. Zeit. Phys. A, Hadrons & Nuclei, 347, 211 (1994).
- [37]Tepel J.W., Hoffman H.M., Weidenmuller H.A. Phys. Lett. 49, 1 (1974).
- [38]Britt H.C., Wilhelmy J.B. Nucl. Sci. Eng., 72, 222 (1979).
- [39]Vorotnikov P.E., Gohberg B.M., Gromova E.A. et al., Proc. Int. Conf. on Neutron Physics, 14-18 Sept., Kiev, USSR, V.3, p.76, 1988.
- [40]Gromova E.A. et al., Sov. J. Atomic Energy, 68, 223 (1990).
- [41]Ignatjuk A.V., Maslov V.M., Pashchenko A.B. Sov. J. Nucl. Phys. 47, 224 (1988).
- [42]Uhl M. and Strohmaier B., Report IRK - 76/10 (Vienna, 1976).
- [43]ENSDF, 1995.

- [44] Porodzinskij Yu.V., Sukhovitskij E.Sh. and Maslov V.M. Int. Conf. Nuclear Data for Science and Technology, Trieste, Italy, May 19-24, 1997, to be published.
- [45] Maslov V.M., Porodzinskij Yu.V., Sukhovitskij E.Sh., Proc. Int. Conf. on Neutron Physics, 14-18 Sept., Kiev, USSR, V.1, p.413, 1988.
- [46] Watt B.E. Phys. Rev., 87, 1032 (1952).
- [47] Terrell J., Proc. of Symp. on Phys. and Chem. of Fission, Salzburg, v.2, p.3 (1965)
- [48] Jaffey A.H., Lerner J.L., Nucl. Phys. A145 (1970); Report ANL-7625 (1969).
- [49] Zamyatnin Yu.S., Kroshkin N.I., Melnikov A.K., et al., Nuclear Data for Reactors, Proc of Int. Conf., Helsinki, 1970, v 2, IAEA, Vienna (1970).
- [50] Malinovski V.V., Tarasko M.Z., Kuzminov B.D., Sov Journal of Atomic Energy, v.2, 430 (1985).
- [51] Howerton R.J., Nucl. Sci. Engng. 62, 438 (1977).
- [52] Manero F., Konshin V.A., Atomic Energy Review, v.10 (1972).
- [53] Tuttle R.J. Proc. Consultants Meeting on Delayed Neutron Properties, 1979, Vienna, INDC(NDS)-107/G, p.29.
- [54] Brady M.C., Wright R.Q., England T.R., Report ORNL/CSD/TM-226(1991), IAEA-NDS-102, 1992



## 9 Figure captions

- Fig. 2.1 Fission cross section of  $^{238}\text{Pu}$  in the energy region below 600 eV.  
Fig. 2.2 Total cross section of  $^{238}\text{Pu}$  in the energy region 100-150 eV.  
Fig. 2.3 Total cross section of  $^{238}\text{Pu}$  in the energy region 100-150 eV.  
Fig. 2.4 Total cross section of  $^{238}\text{Pu}$  in the energy region 145-200 eV.  
Fig. 2.5 Total cross section of  $^{238}\text{Pu}$  in the energy region 100-150 eV.  
Fig. 2.6 Fission cross section of  $^{238}\text{Pu}$  in the energy region 105-145 eV.  
Fig. 2.7 Fission cross section of  $^{238}\text{Pu}$  in the energy region 105-145 eV.  
Fig. 2.8 Fission cross section of  $^{238}\text{Pu}$  in the energy region 105-145 eV.  
Fig. 2.9 Capture cross section of  $^{238}\text{Pu}$  in the energy region 105-145 eV.  
Fig. 2.10 Fission cross section of  $^{238}\text{Pu}$  in the energy region 250-350 eV.  
Fig. 2.11 Fission cross section of  $^{238}\text{Pu}$  in the energy region 250-350 eV.  
Fig. 2.12 Fission cross section of  $^{238}\text{Pu}$  in the energy region 250-350 eV.  
Fig. 2.13 Capture cross section of  $^{238}\text{Pu}$  in the energy region 250-350 eV.  
Fig. 2.14 Distribution of capture widths.  
Fig. 3.1 Cumulative sum of neutron resonance levels of  $^{238}\text{Pu}$   
Fig. 3.2 Cumulative sum of reduced neutron widths of  $^{238}\text{Pu}$   
Fig. 3.3 Distribution of reduced neutron widths for  $^{238}\text{Pu}$ .  
Fig. 3.4 Neutron resonance spacing distribution for  $^{238}\text{Pu}$ .  
Fig. 3.5 Fission cross section of  $^{238}\text{Pu}$  in unresolved resonance region.  
Fig. 3.6 Radiative capture cross section of  $^{238}\text{Pu}$  in unresolved resonance region.  
Fig. 4.1 Compound reaction cross section of  $^{238}\text{Pu}$ .  
Fig. 4.2 Total cross section of  $^{238}\text{Pu}$ .  
Fig. 4.3 Elastic scattering cross section of  $^{238}\text{Pu}$ .  
Fig. 4.4 Fission cross section of  $^{238}\text{Pu}$ .  
Fig. 4.5 Fission cross section of  $^{238}\text{Pu}$ .  
Fig. 4.6 Fission cross section of  $^{238}\text{Pu}$ .  
Fig. 4.7 Fission cross section of  $^{238}\text{Pu}$ .  
Fig. 4.8 Fission cross section of  $^{237}\text{Pu}$ .  
Fig. 4.9 Fission cross section of  $^{236}\text{Pu}$ .  
Fig. 4.10 Fission cross section of  $^{238}\text{Pu}$ .  
Fig. 4.11 Cumulative number of levels of  $^{238}\text{Pu}$ .  
Fig. 4.12 Inelastic scattering cross section of  $^{238}\text{Pu}$ .  
Fig. 4.13 Continuum inelastic scattering cross section of  $^{238}\text{Pu}$ .  
Fig. 4.14 Cumulative number of levels of  $^{239}\text{Pu}$ .  
Fig. 4.15 Cross section of  $^{238}\text{Pu}$ : 0.04408 MeV,  $2^+$  level excitation.  
Fig. 4.16 Cross section of  $^{238}\text{Pu}$ : 0.14596 MeV,  $4^+$  level excitation.

- Fig. 4.17 Cross section of  $^{238}\text{Pu}$ : 0.3034 MeV,  $6^+$  level excitation.  
Fig. 4.18 Cross section of  $^{238}\text{Pu}$ : 0.5134 MeV,  $8^+$  level excitation.  
Fig. 4.19 Cross section of  $^{238}\text{Pu}$ : 0.60518 MeV,  $1^-$  level excitation.  
Fig. 4.20 Cross section of  $^{238}\text{Pu}$ : 0.66143 MeV,  $3^-$  level excitation.  
Fig. 4.21 Radiative capture cross section of  $^{238}\text{Pu}$ .  
Fig. 4.22  $^{238}\text{Pu}(\text{n},2\text{n})$  reaction cross section.  
Fig. 4.23  $^{238}\text{Pu}(\text{n},3\text{n})$  reaction cross section.  
Fig. 5.1 Components of first neutron spectrum of  $^{238}\text{Pu}$  for incident neutron energy 14 MeV.  
Fig. 5.2 Components of second neutron spectrum of  $^{238}\text{Pu}$  for incident neutron energy 14 MeV.  
Fig. 5.3 Comparison of  $(\text{n},\text{n}'\gamma)$  reaction neutron spectra of  $^{238}\text{Pu}$  for incident neutron energy 8 MeV.  
Fig. 5.4 Comparison of  $(\text{n},2\text{n})$  reaction neutron spectra of  $^{238}\text{Pu}$  for incident neutron energy 8 MeV.  
Fig. 5.5 Comparison of  $(\text{n},\text{n}'\gamma)$  reaction neutron spectra of  $^{238}\text{Pu}$  for incident neutron energy 14 MeV.  
Fig. 5.6 Comparison of  $(\text{n},2\text{n})$  reaction neutron spectra of  $^{238}\text{Pu}$  for incident neutron energy 14 MeV.  
Fig. 5.7 Comparison of  $(\text{n},3\text{n})$  reaction neutron spectra of  $^{238}\text{Pu}$  for incident neutron energy 14 MeV.  
Fig. 5.8 Thermal prompt fission neutron spectrum of  $^{238}\text{Pu}$ .  
Fig. 5.9 Calculated fission neutron spectra of  $^{238}\text{Pu}$  ratio to JENDL-3 evaluation (  $T_{\text{maxw}} = 1.48$  ).  
Fig. 5.10 Fission neutron spectra of  $^{238}\text{Pu}$  for incident neutron energy 6 MeV.  
Fig. 5.11 Fission neutron spectra of  $^{238}\text{Pu}$  for incident neutron energy 14 MeV.  
Fig. 5.12 Fission neutron spectra of  $^{238}\text{Pu}$  for incident neutron energy 20 MeV.  
Fig. 5.13 Fission neutron spectra of  $^{238}\text{Pu}$  for incident neutron energy 15 MeV.  
Fig. 6.1 Prompt fission neutron multiplicity for  $^{238}\text{Pu}$ .

# $^{238}\text{Pu}$ FISSION CROSS SECTION

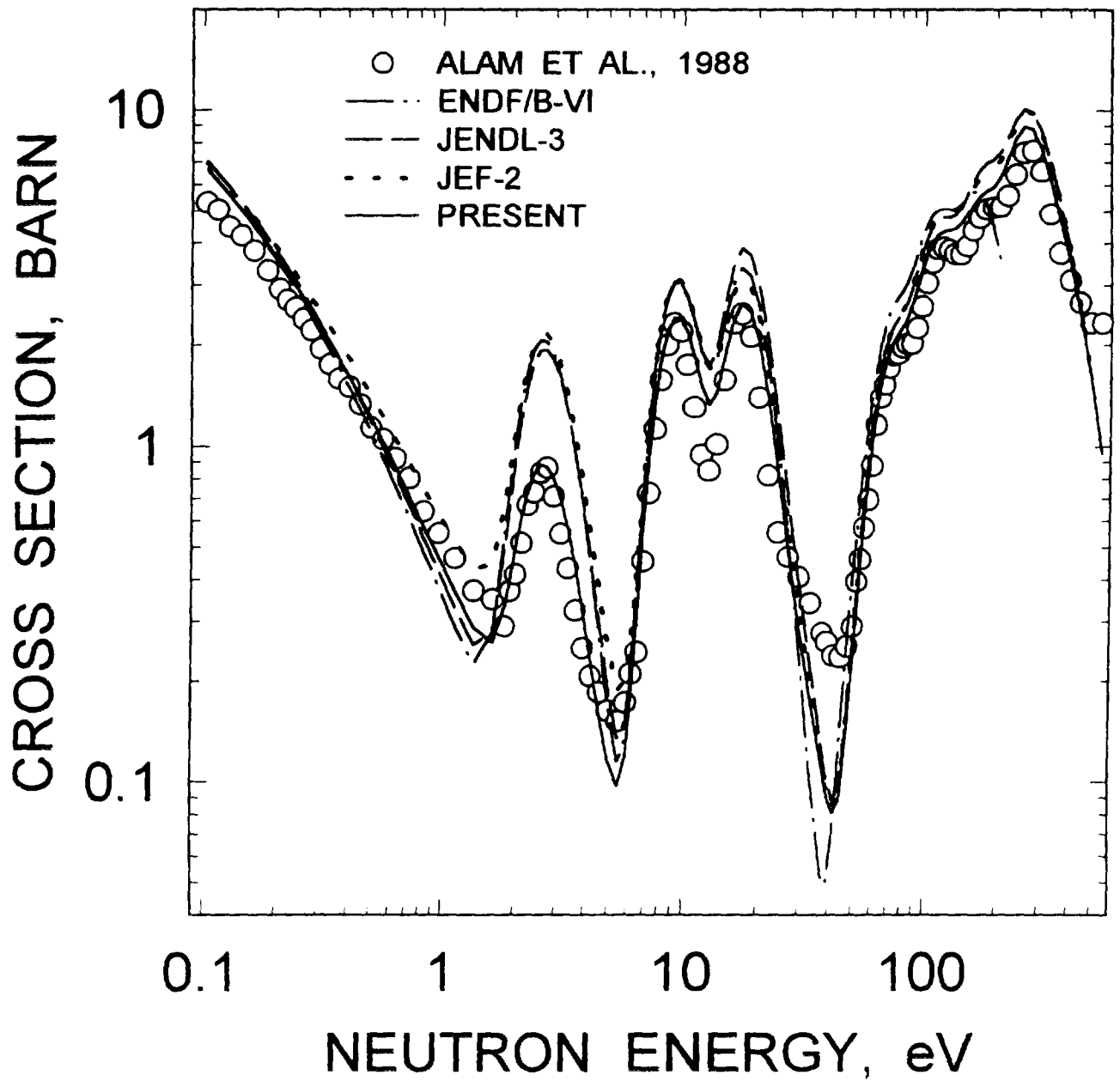


FIG.2.1

# $^{238}\text{Pu}$ TOTAL CROSS SECTION

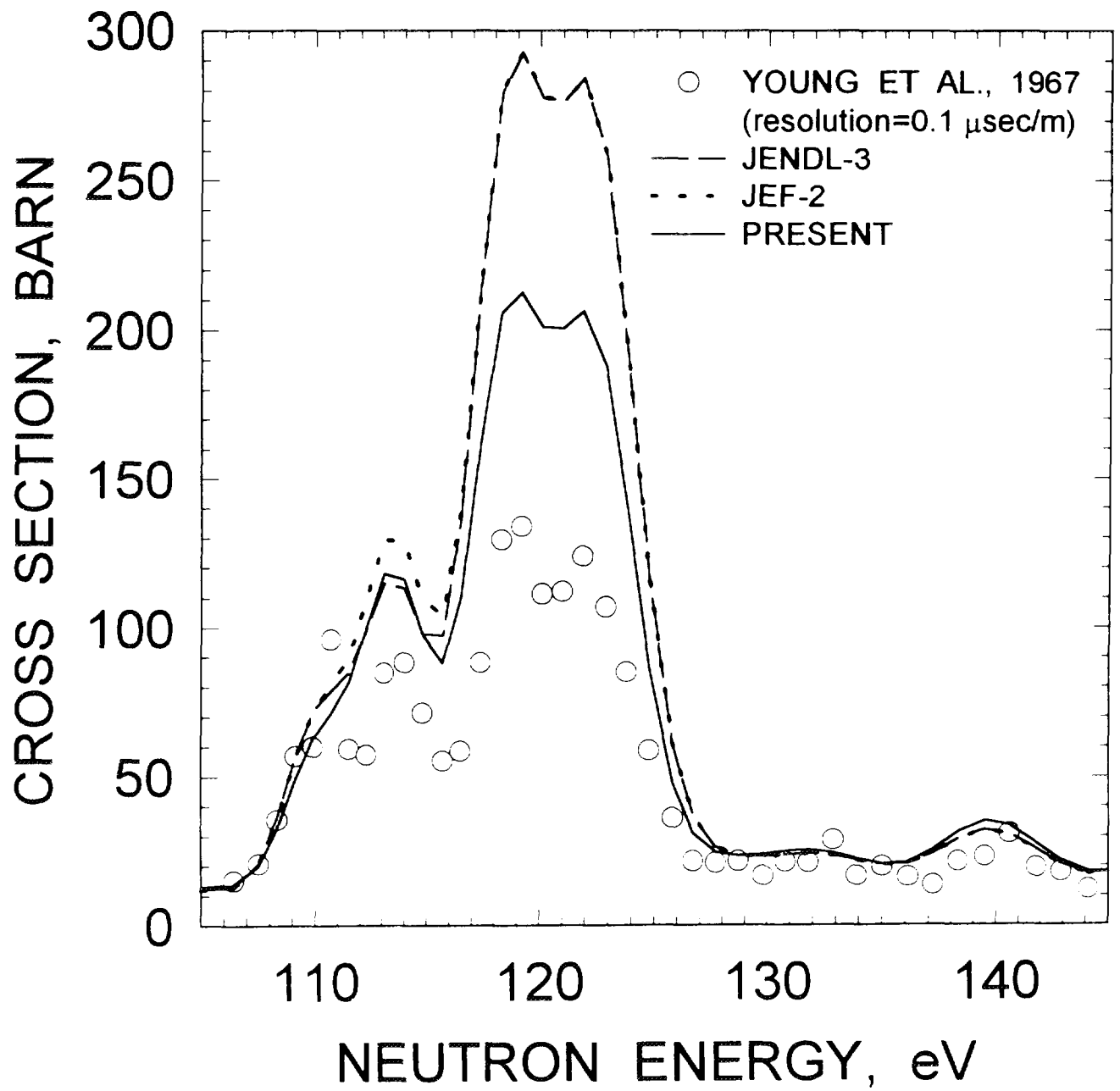


FIG.2.2

# $^{238}\text{Pu}$ TOTAL CROSS SECTION

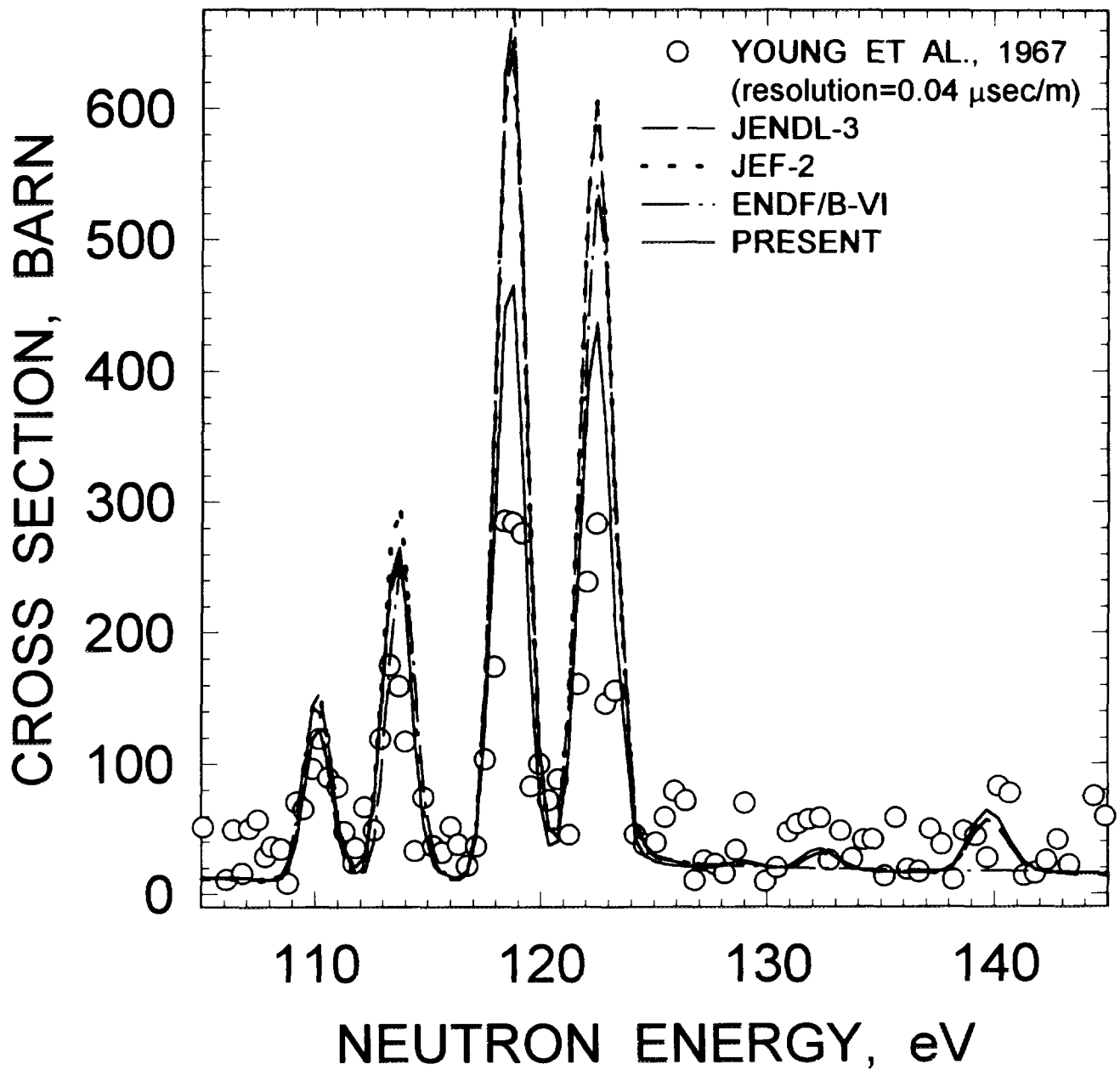


FIG.2.3

# $^{238}\text{Pu}$ TOTAL CROSS SECTION

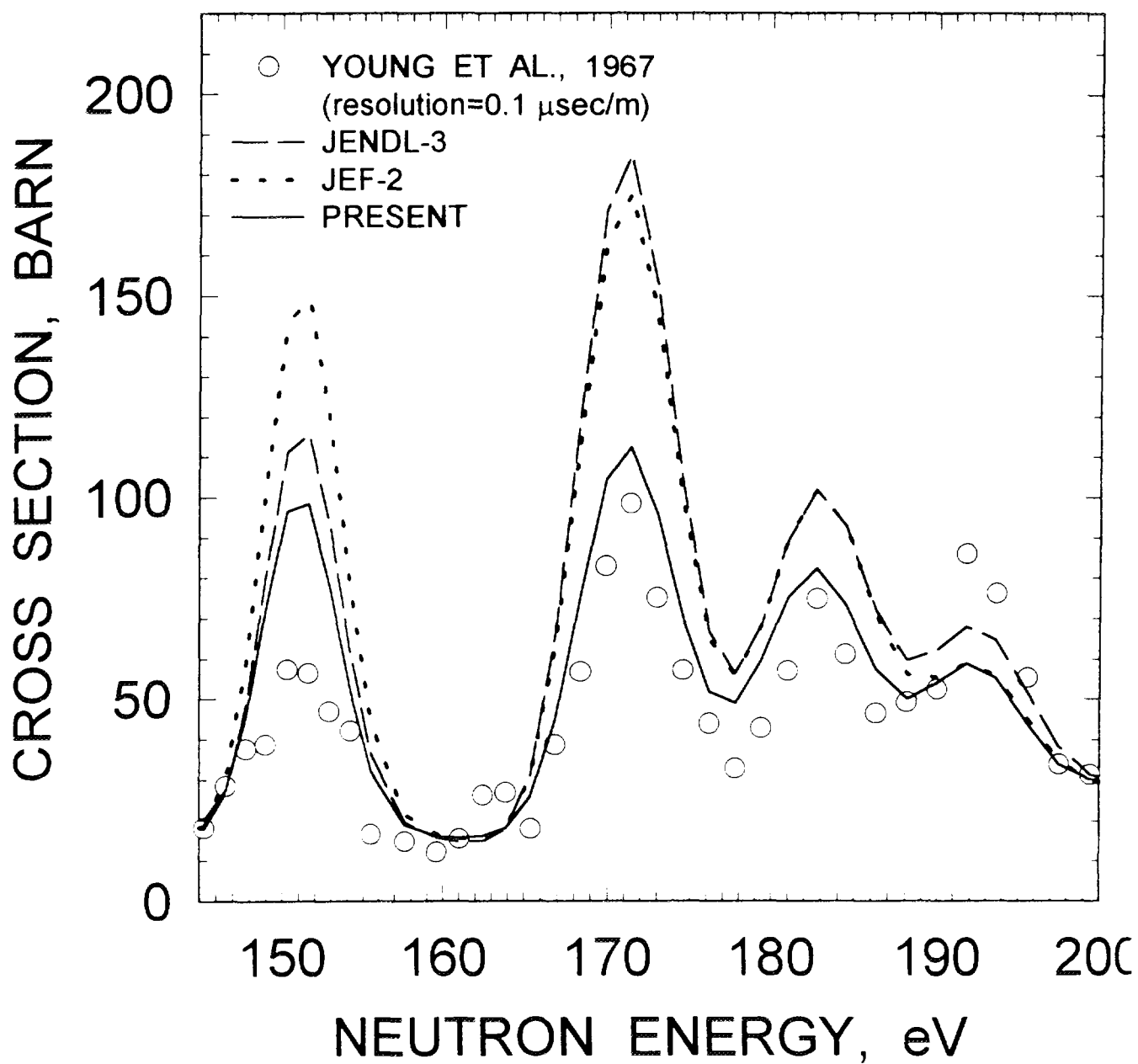


FIG.2.4

# $^{238}\text{Pu}$ TOTAL CROSS SECTION

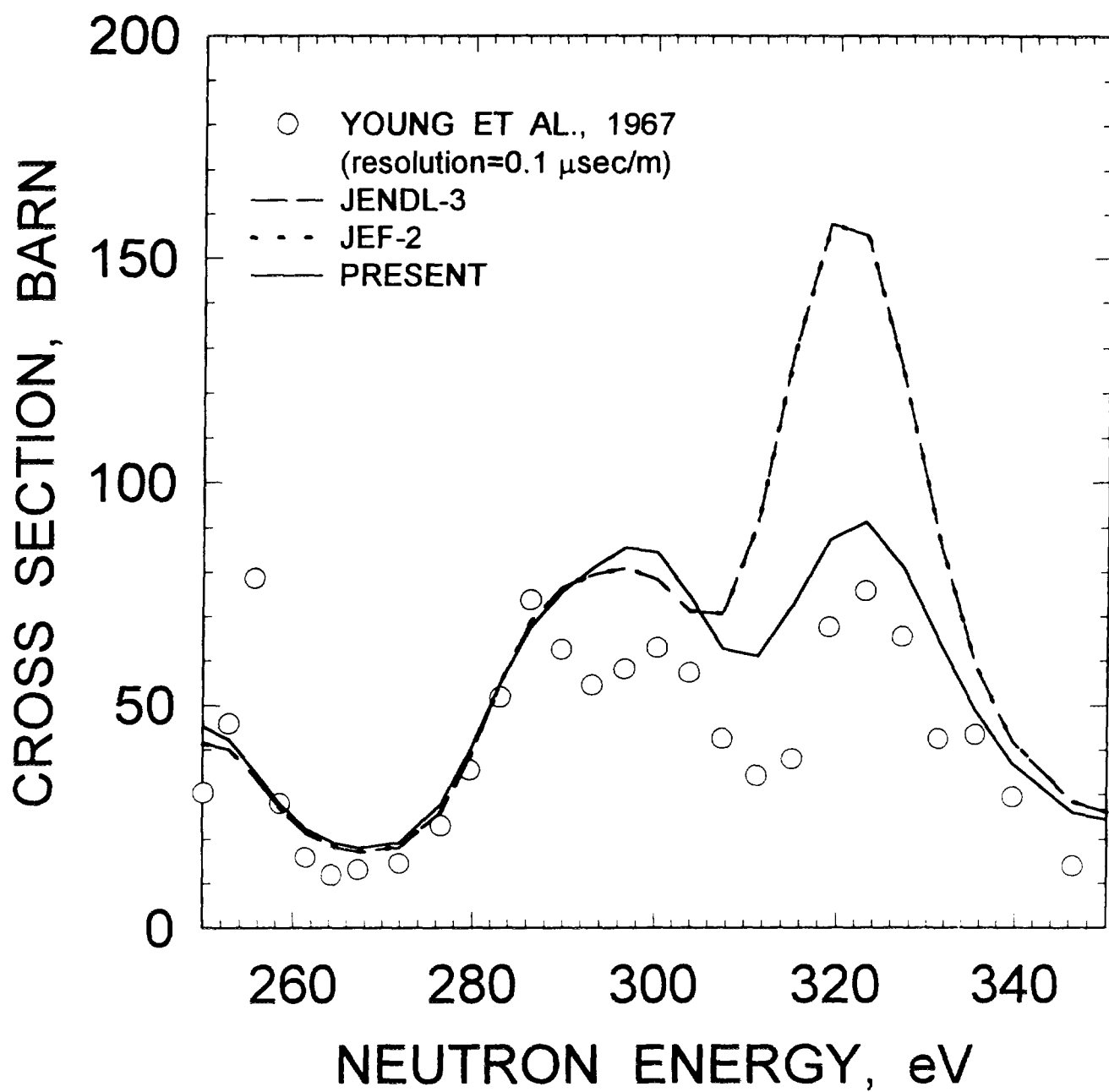


FIG.2.5

# $^{238}\text{Pu}$ FISSION CROSS SECTION

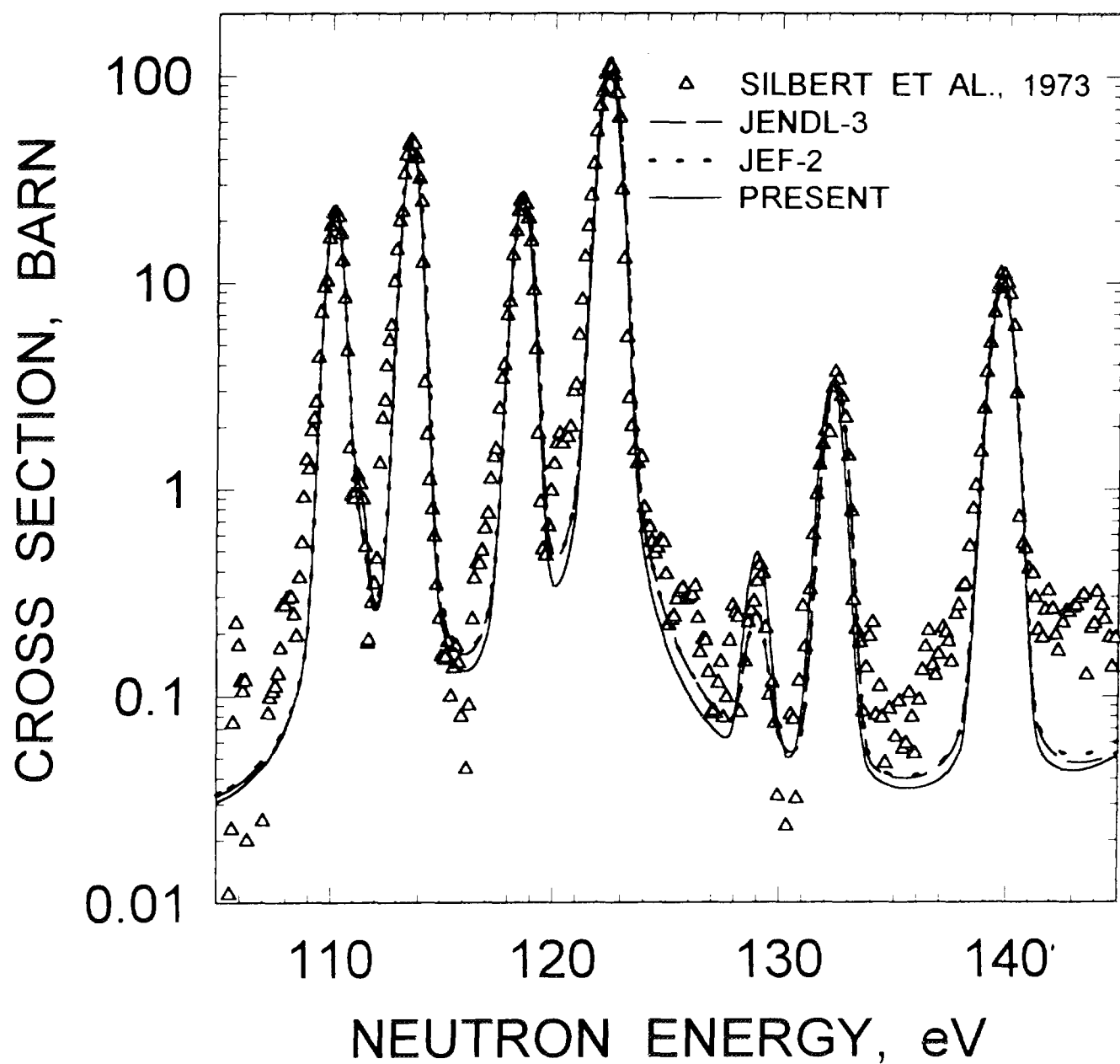


FIG.2.6



# $^{238}\text{Pu}$ FISSION CROSS SECTION

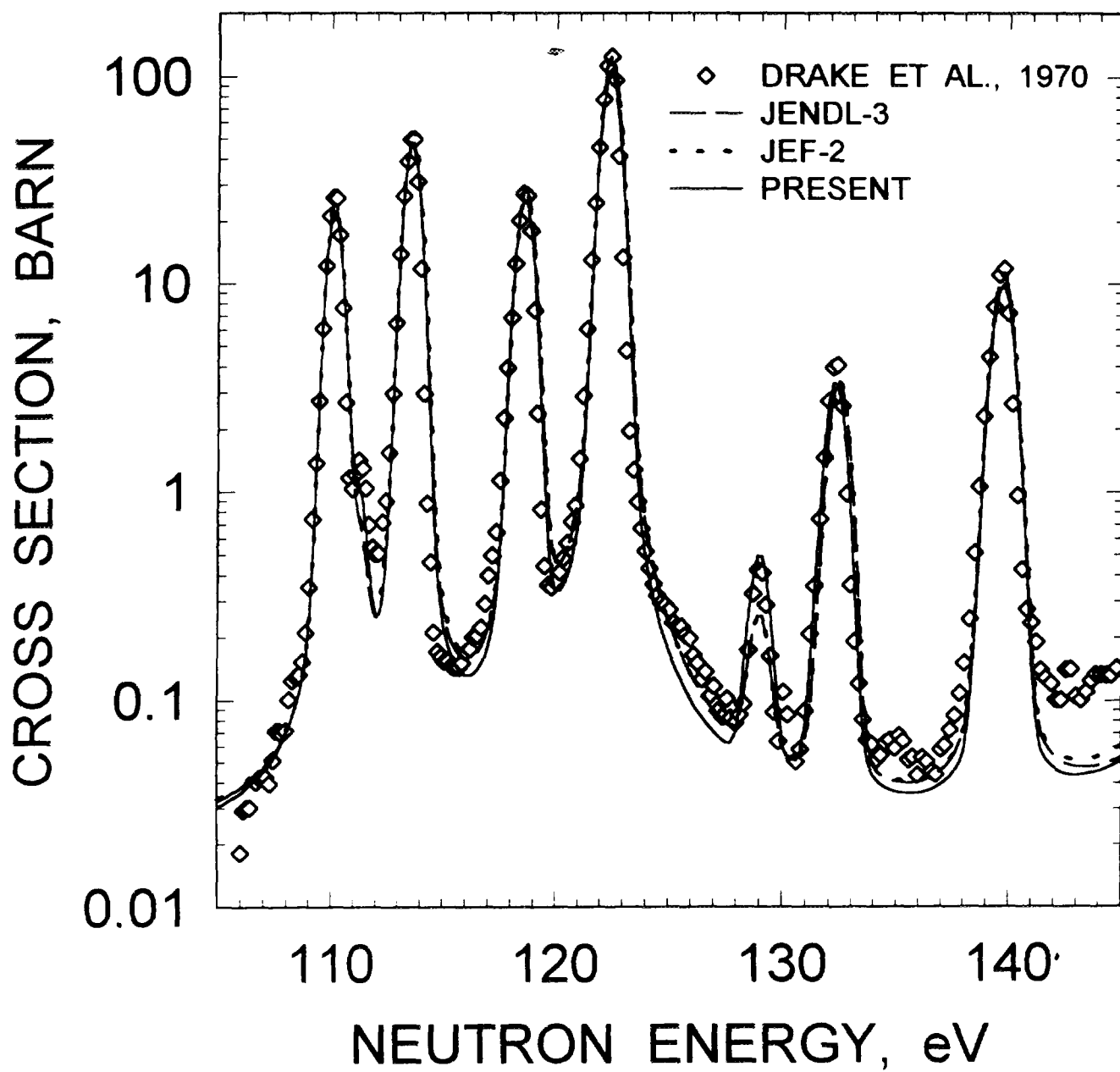


FIG.2.7

# $^{238}\text{Pu}$ FISSION CROSS SECTION

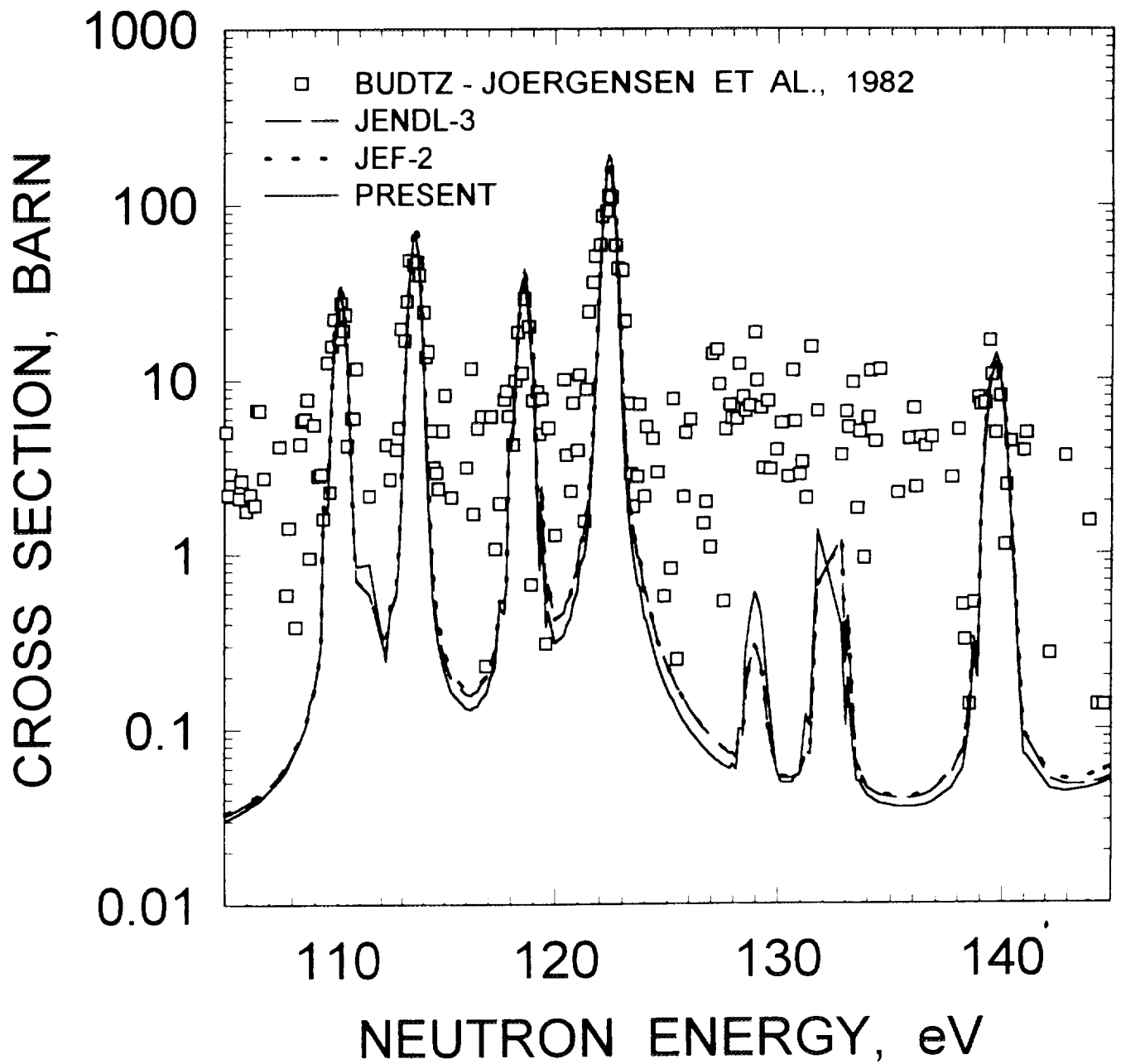


FIG.2.8

# $^{238}\text{Pu}$ CAPTURE CROSS SECTION

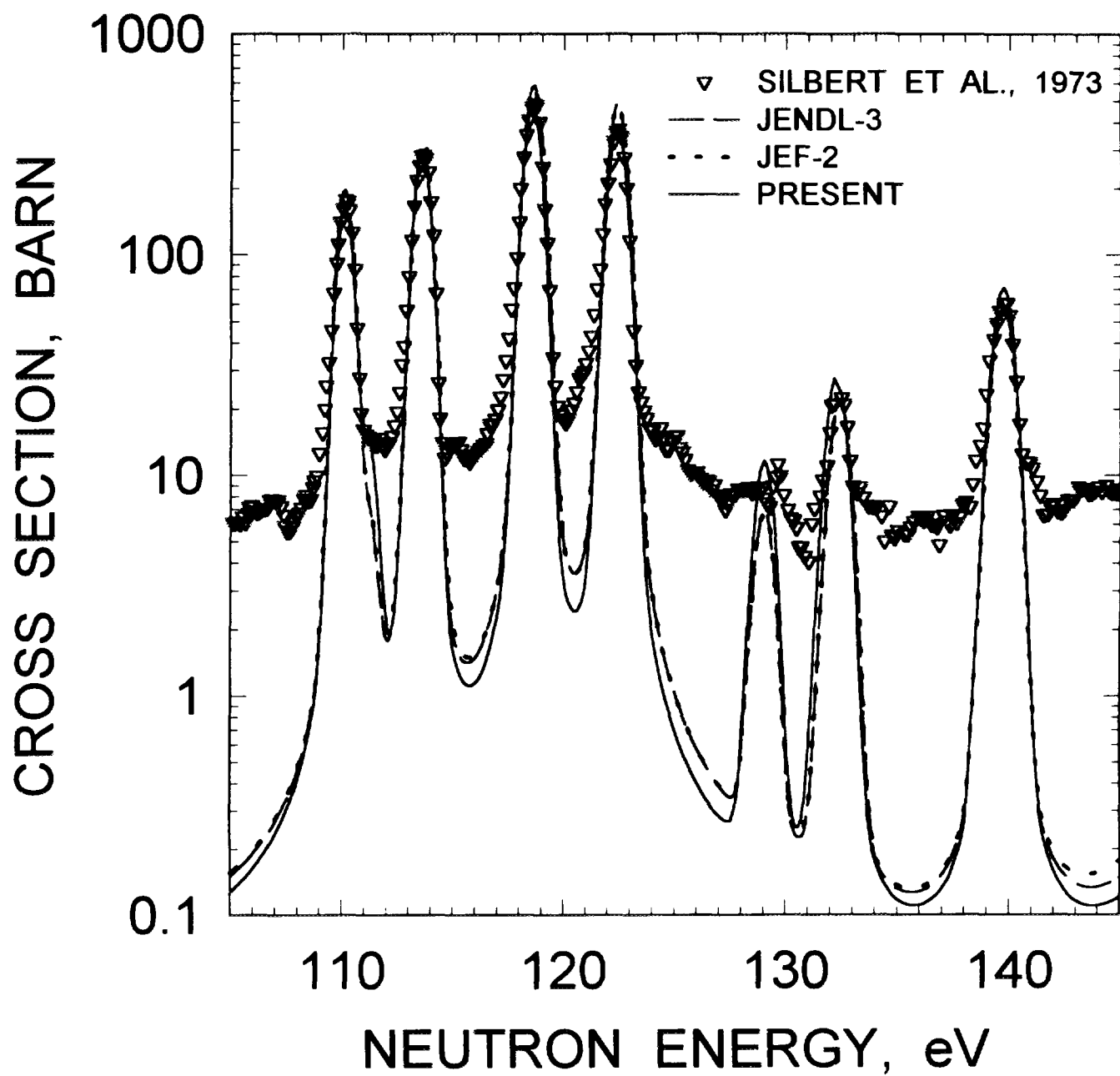


FIG.2.9

# $^{238}\text{Pu}$ FISSION CROSS SECTION

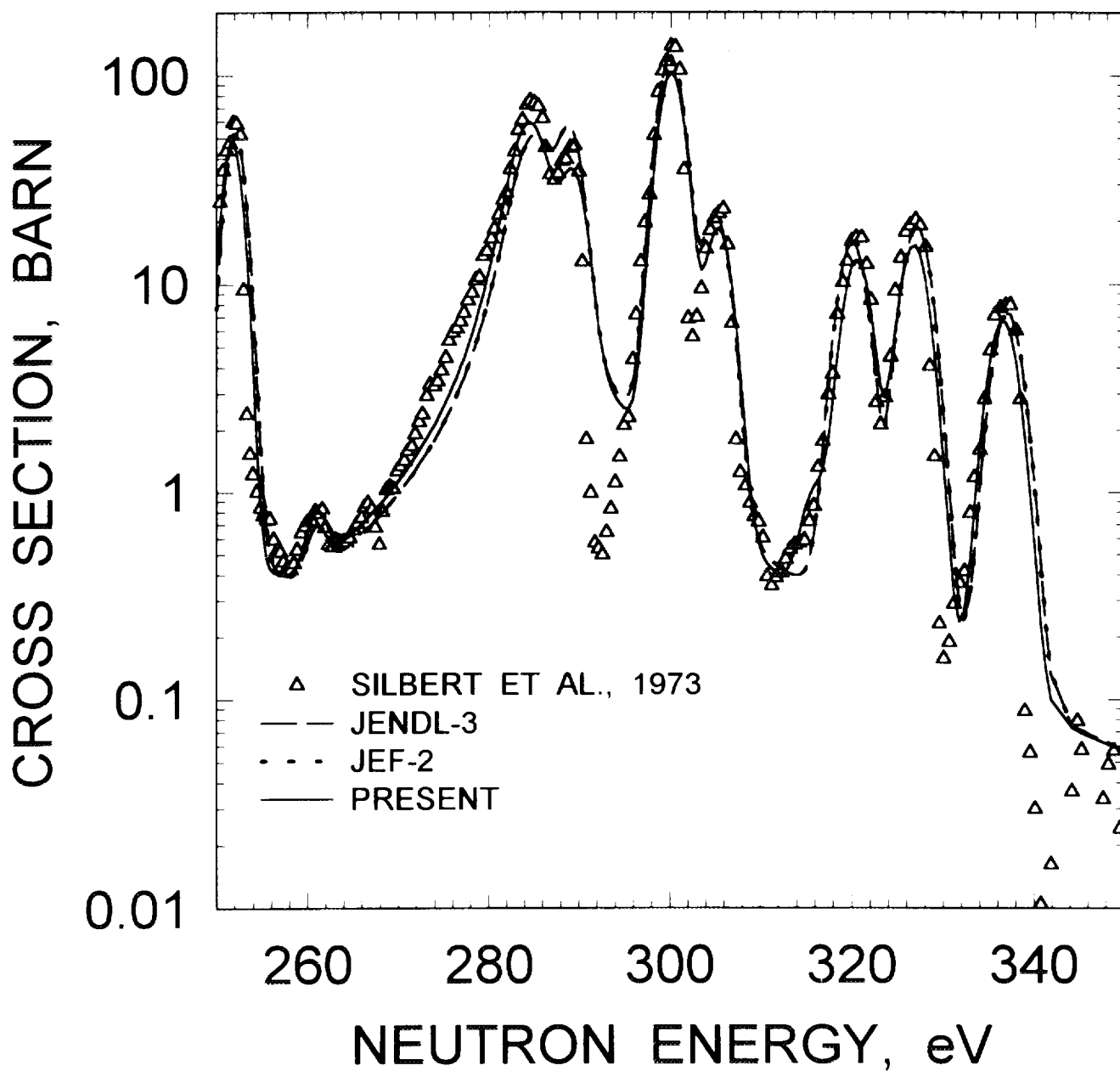


FIG.2.10

# $^{238}\text{Pu}$ FISSION CROSS SECTION

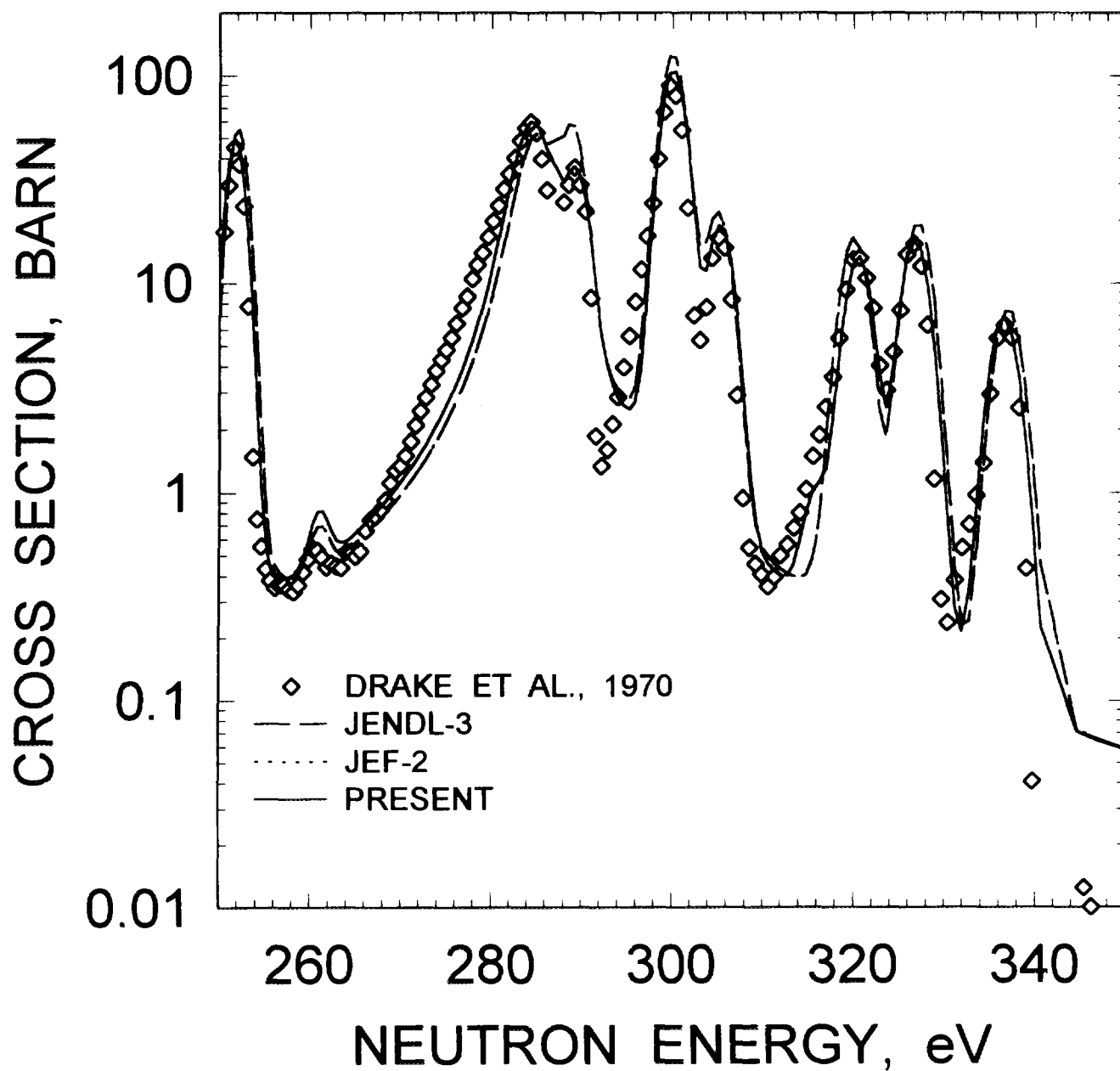


FIG.2.11

# $^{238}\text{Pu}$ FISSION CROSS SECTION

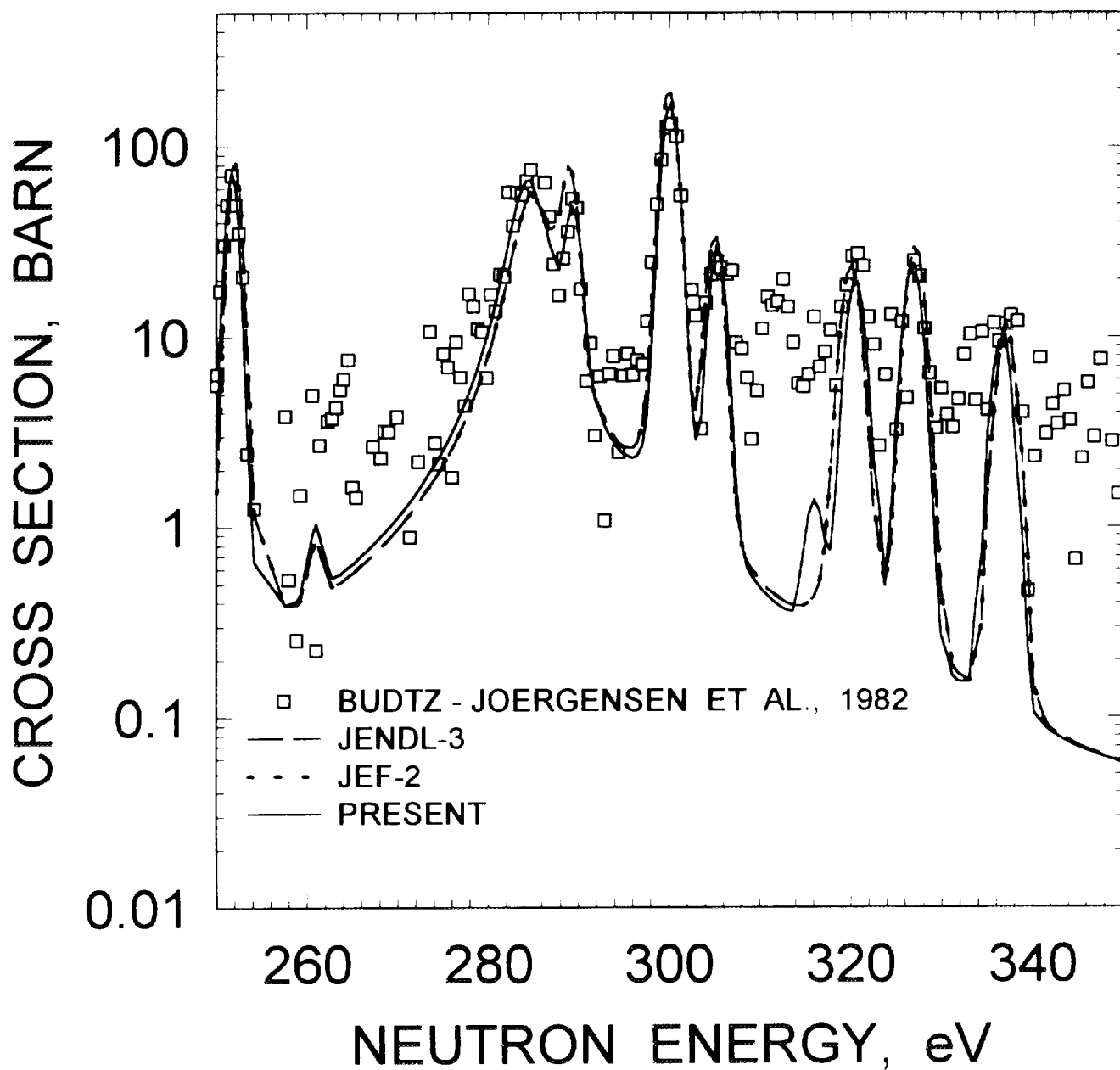


FIG.2.12

# $^{238}\text{Pu}$ CAPTURE CROSS SECTION

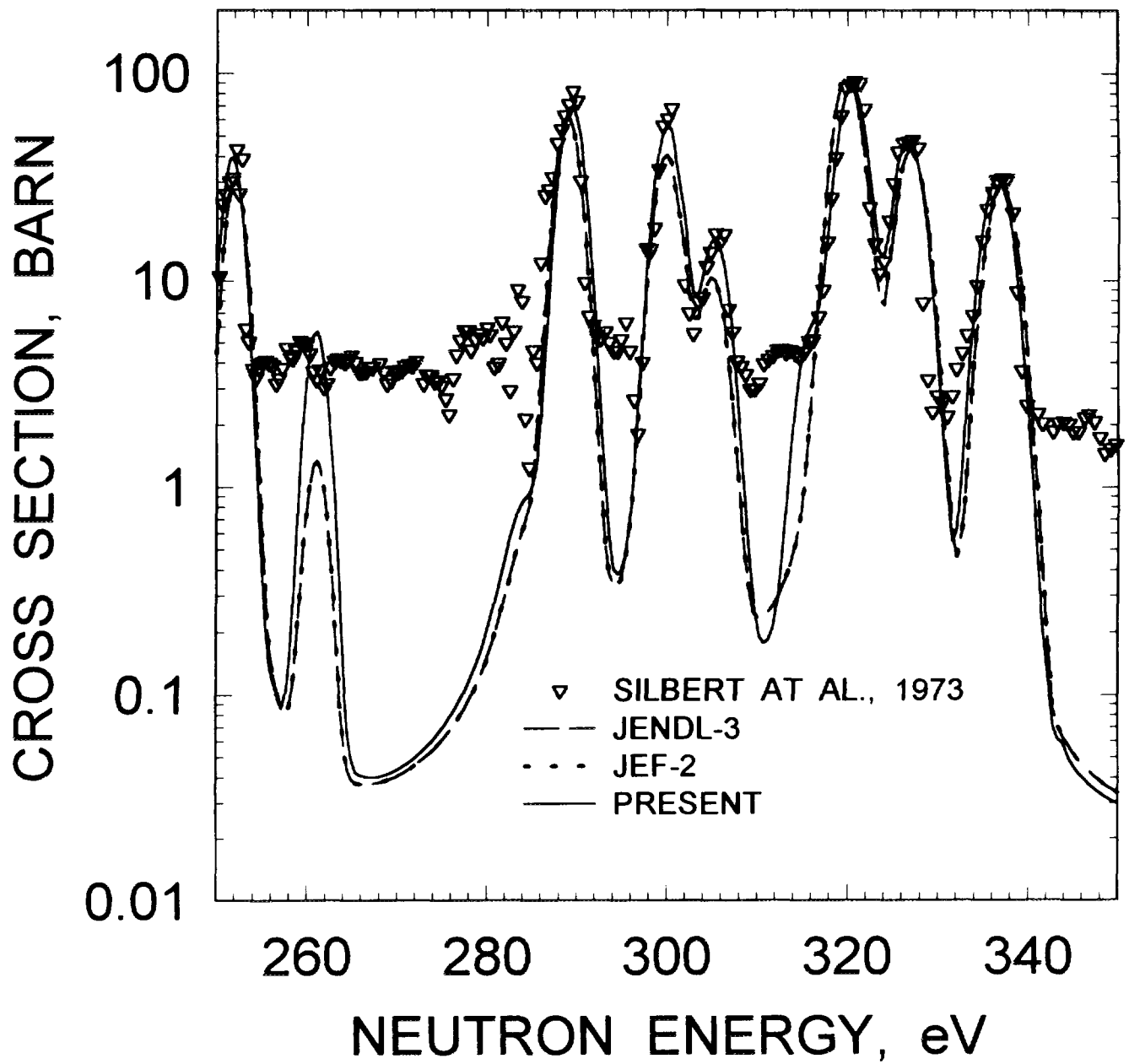


FIG.2.13

# $^{238}\text{Pu}$ DISTRIBUTION OF CAPTURE WIDTHS

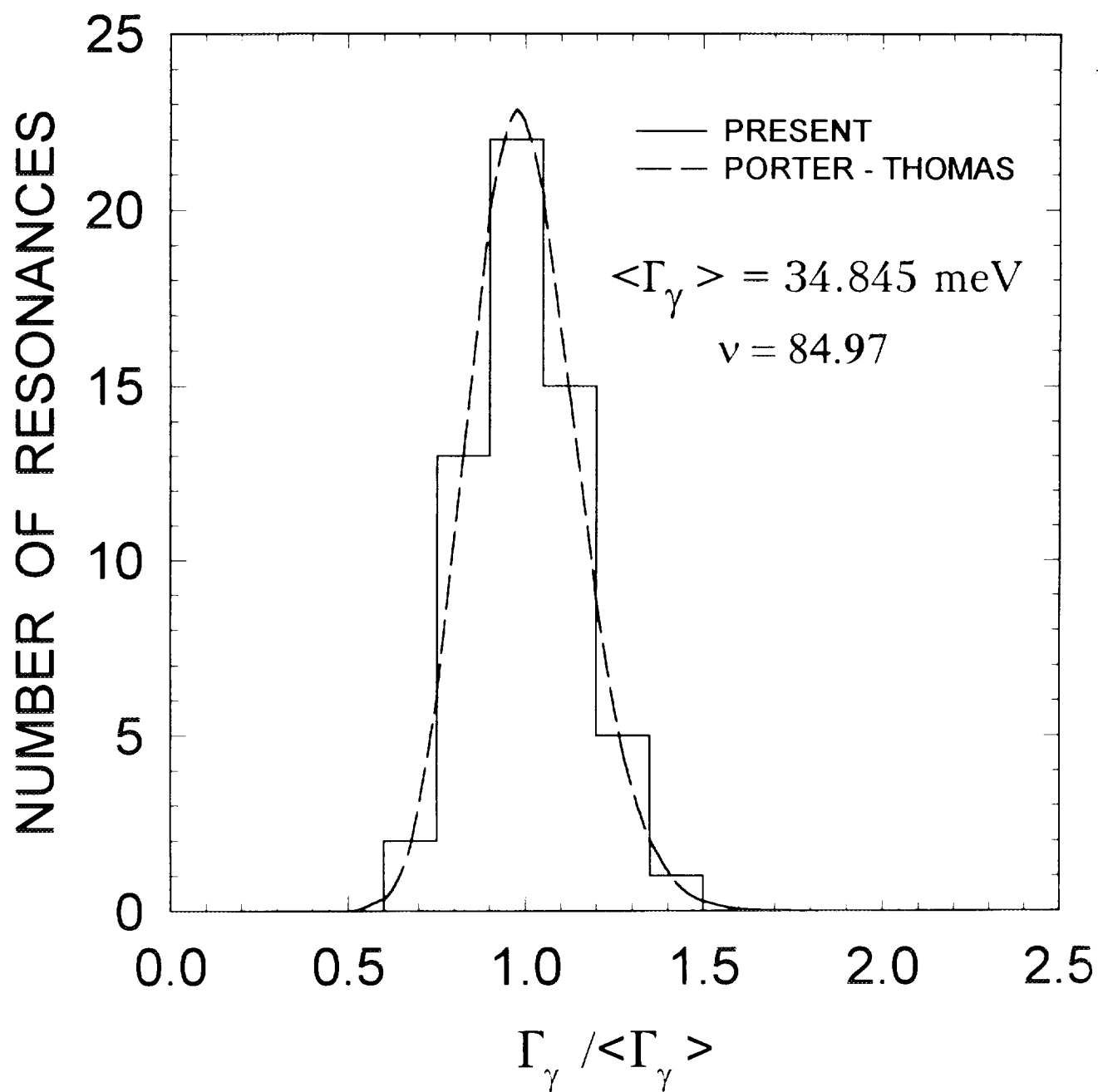


FIG.2.14



# $^{238}\text{Pu}$ CUMULATIVE SUM OF LEVELS

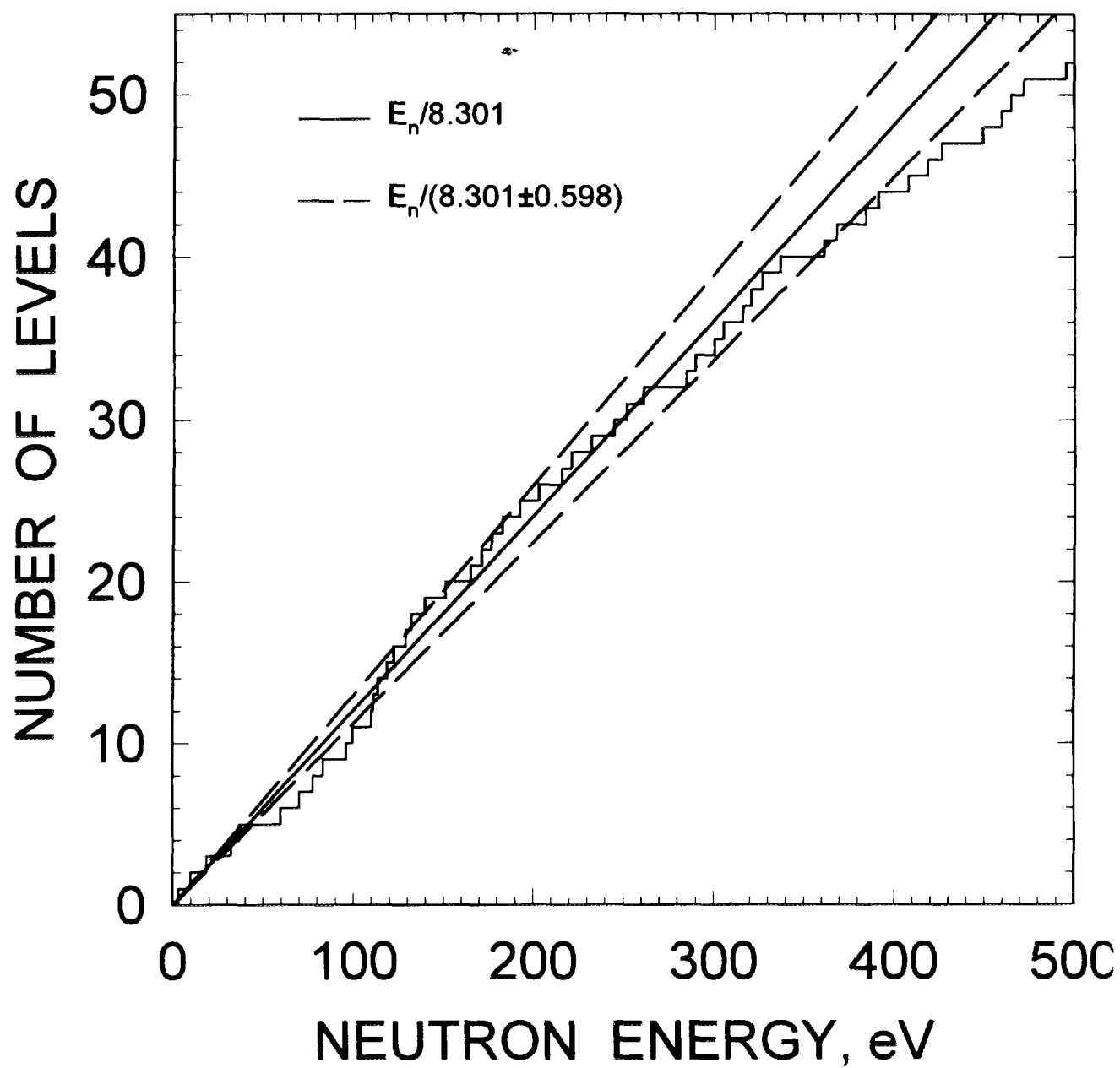


FIG. 3.1

$^{238}\text{Pu}$  CUMULATIVE SUM OF REDUCED  
NEUTRON WIDTHS

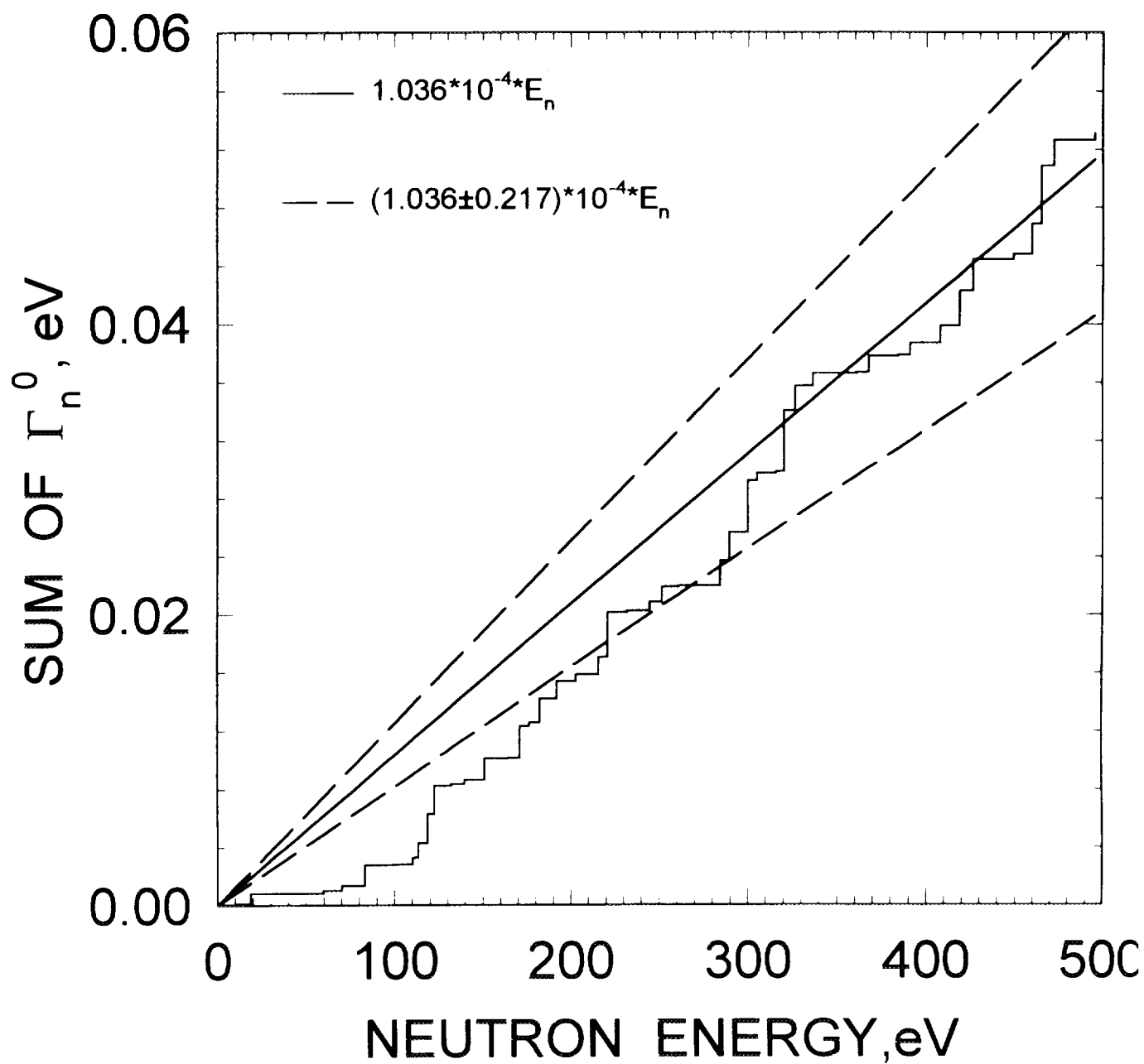


FIG. 3.2

# $^{238}\text{Pu}$ REDUCED NEUTRON WIDTH DISTRIBUTION

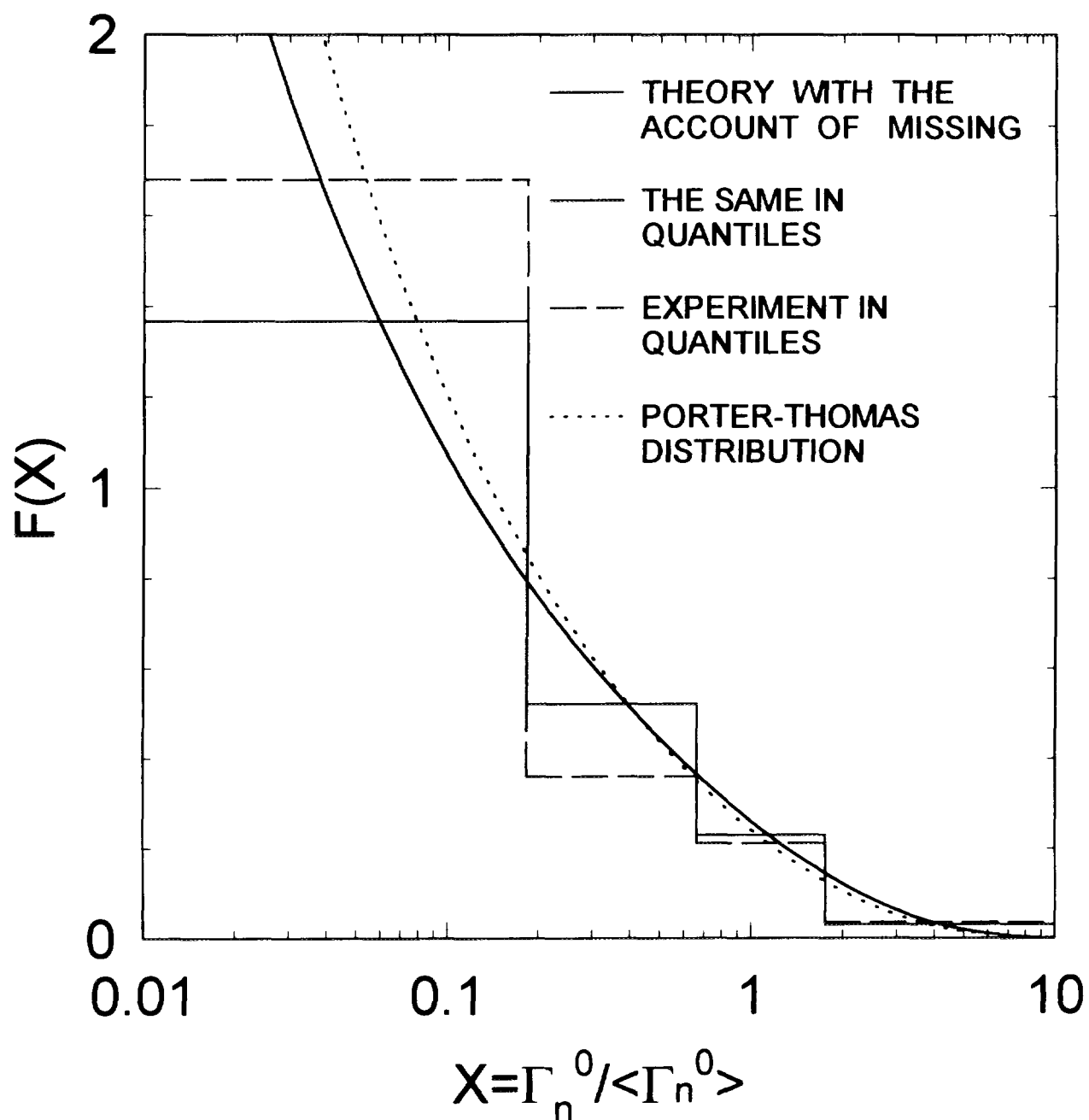


FIG. 3.3

# $^{238}\text{Pu}$ LEVEL SPACING DISTRIBUTION

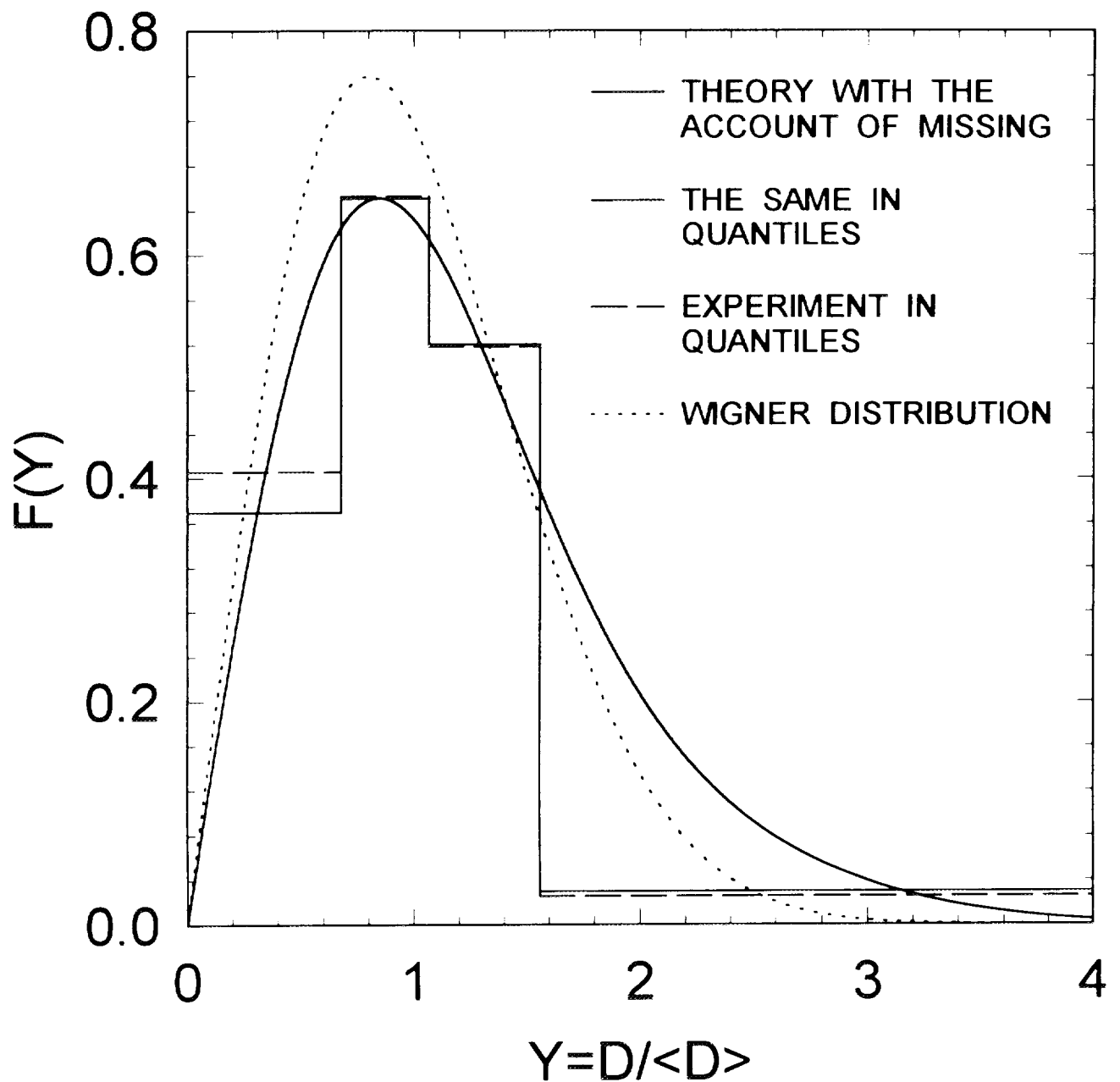


FIG. 3.4

# $^{238}\text{Pu}$ FISSION CROSS SECTION

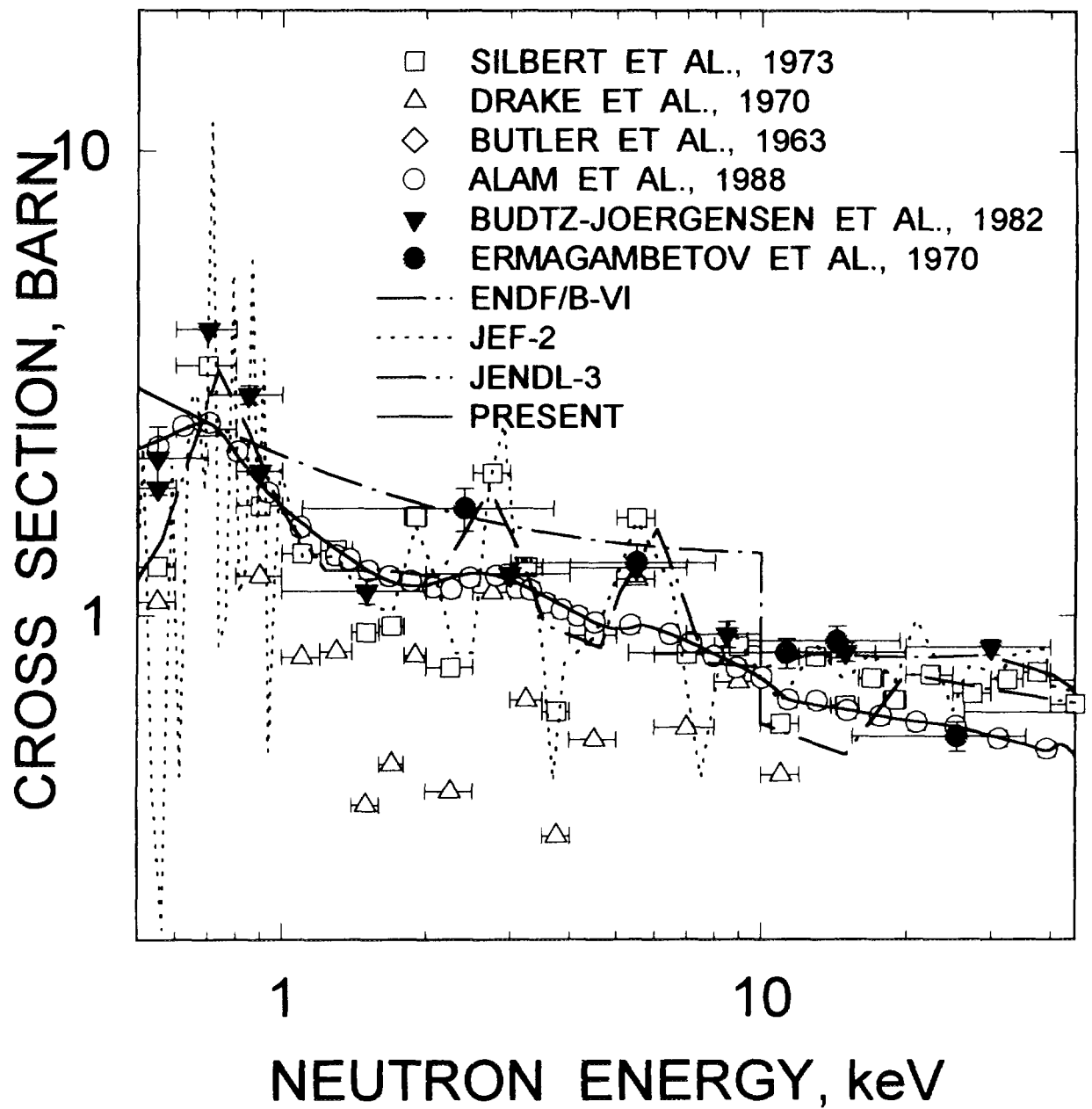


FIG.3.5

# $^{238}\text{Pu}$ CAPTURE CROSS SECTION

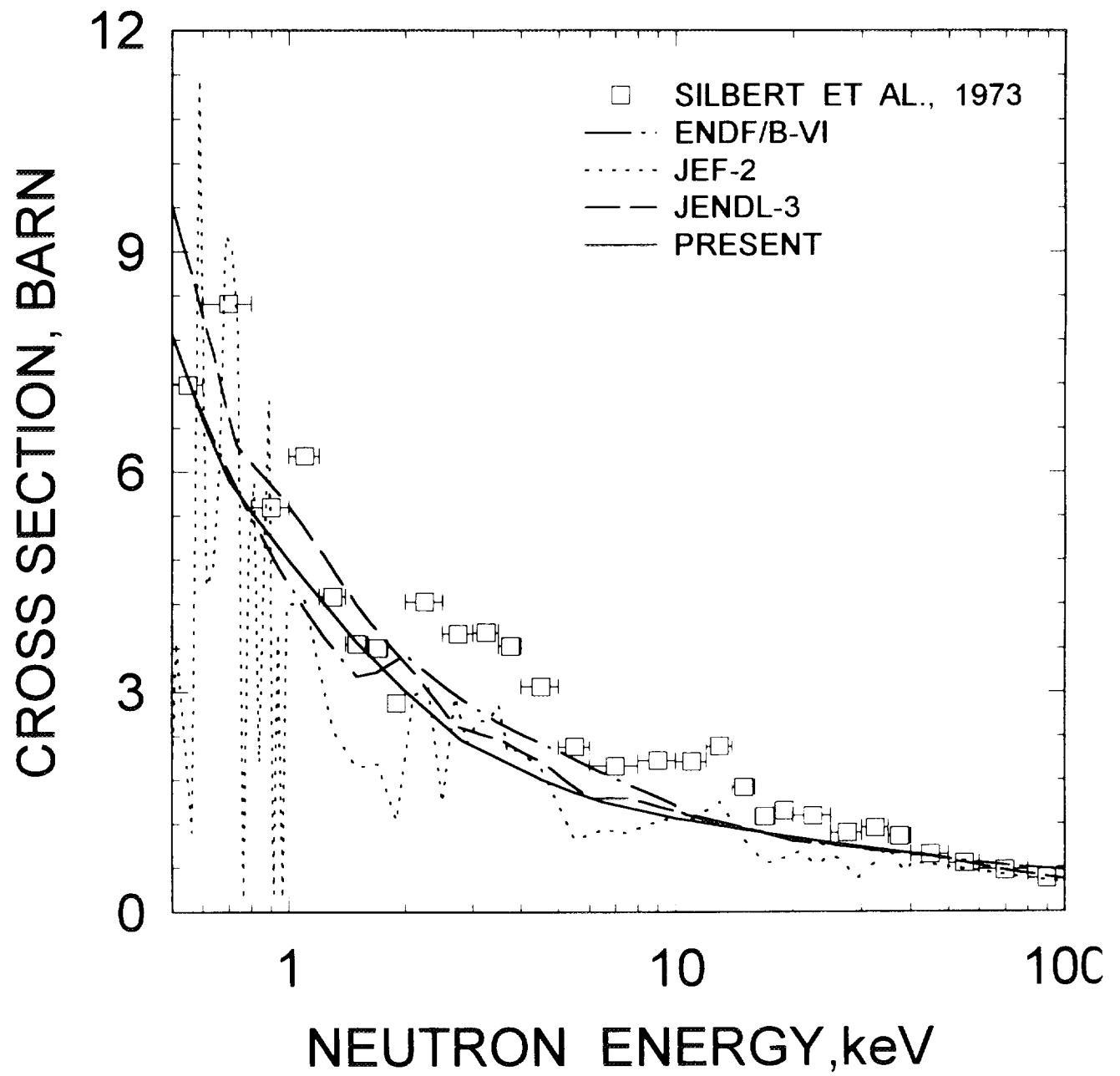


FIG.3.6

# $^{238}\text{Pu}$ REACTION CROSS SECTION

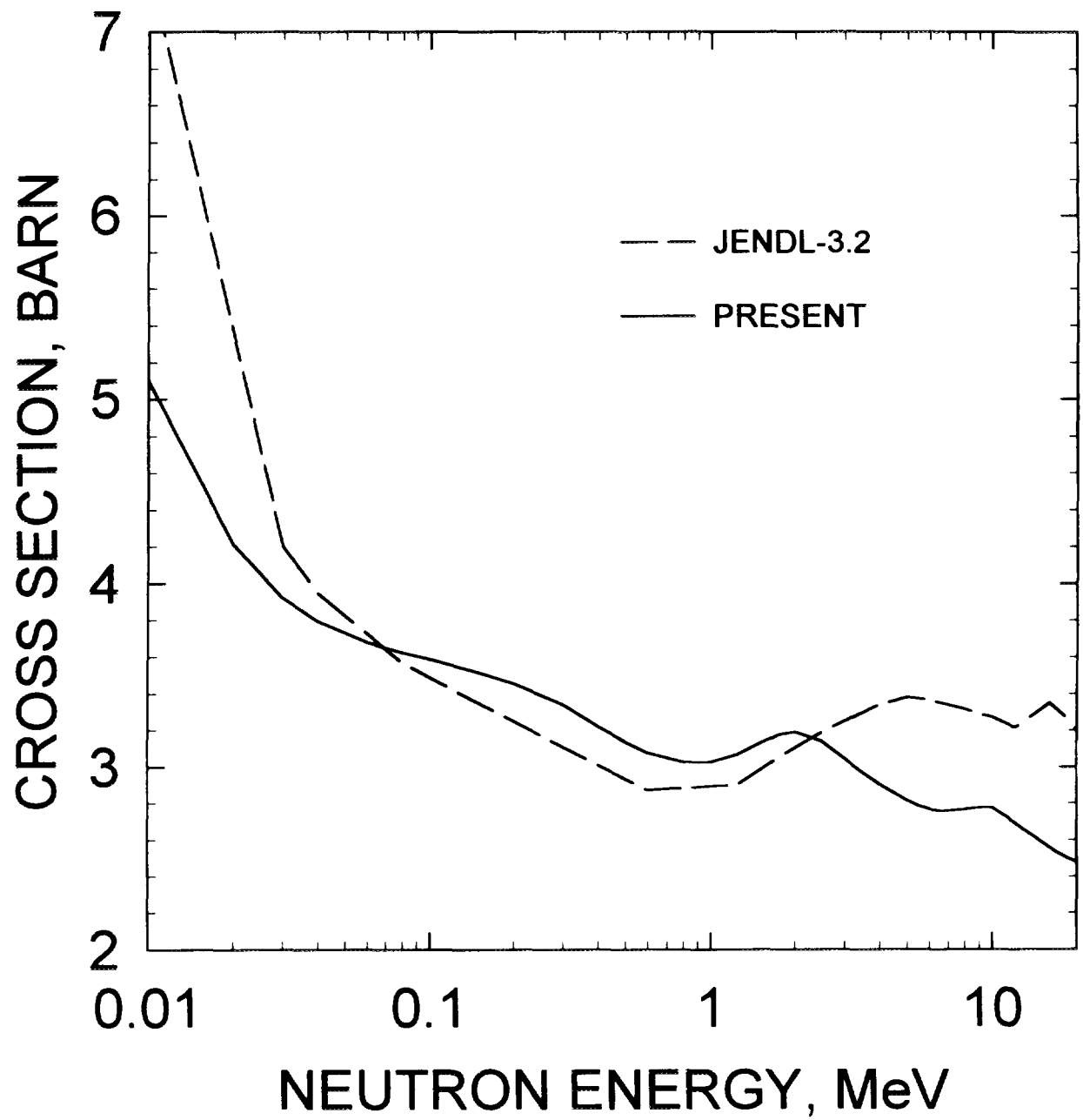


FIG.4.1

$^{238}\text{Pu}$  TOTAL CROSS SECTION

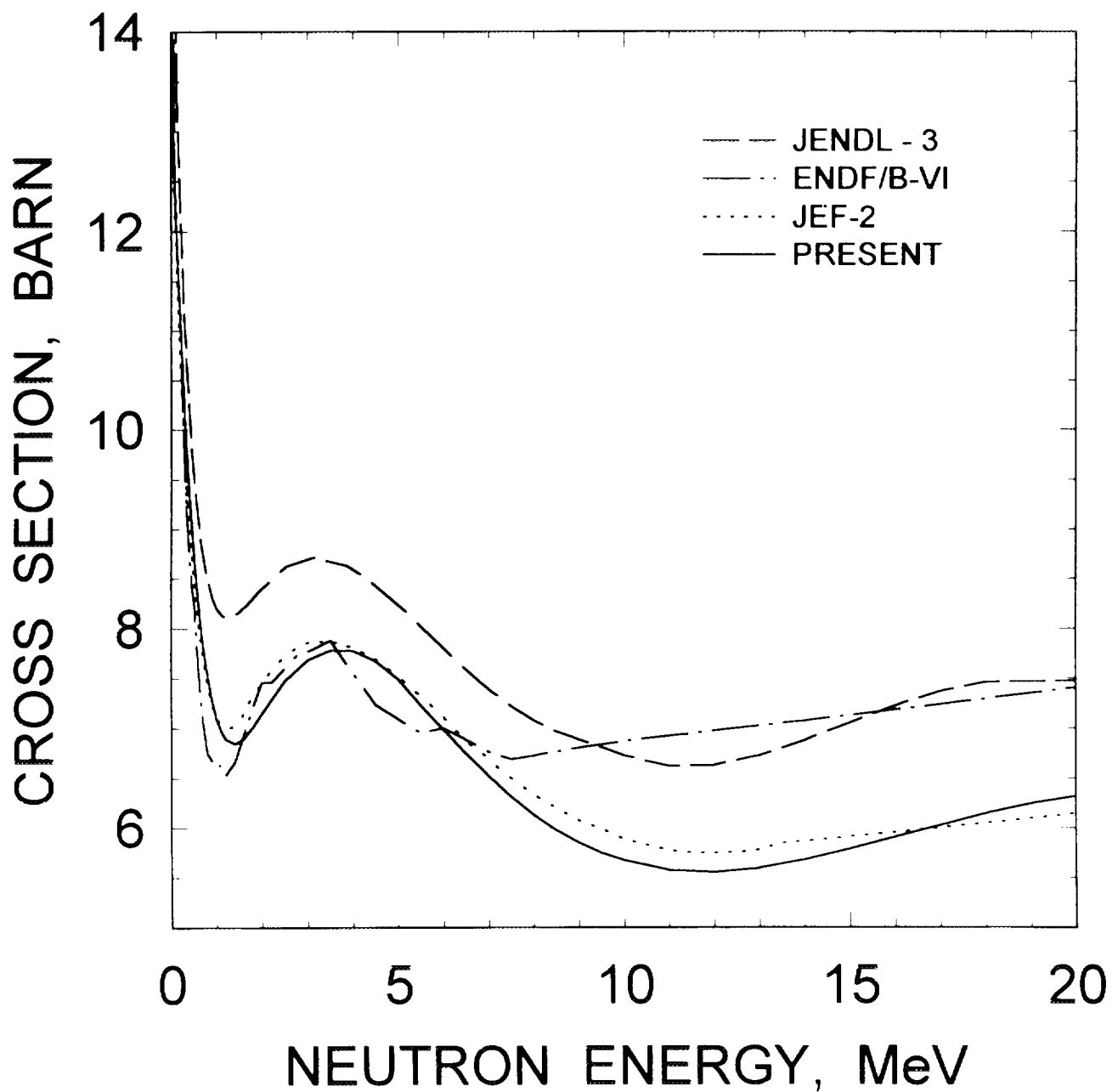


FIG. 4.2



$^{238}\text{Pu}$  ELASTIC SCATTERING  
CROSS SECTION

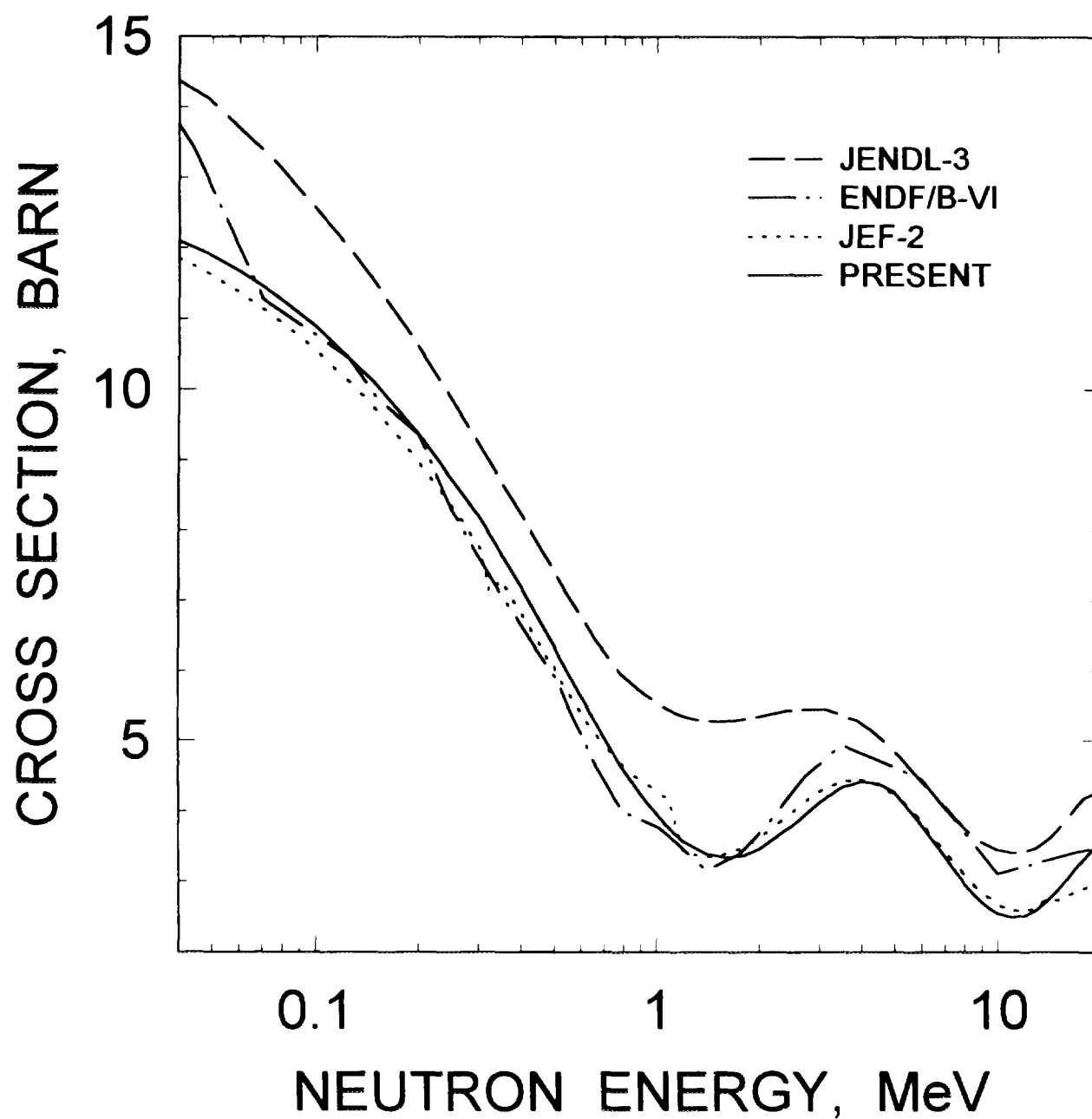


FIG. 4.3

## $^{238}\text{Pu}$ FISSION CROSS SECTION

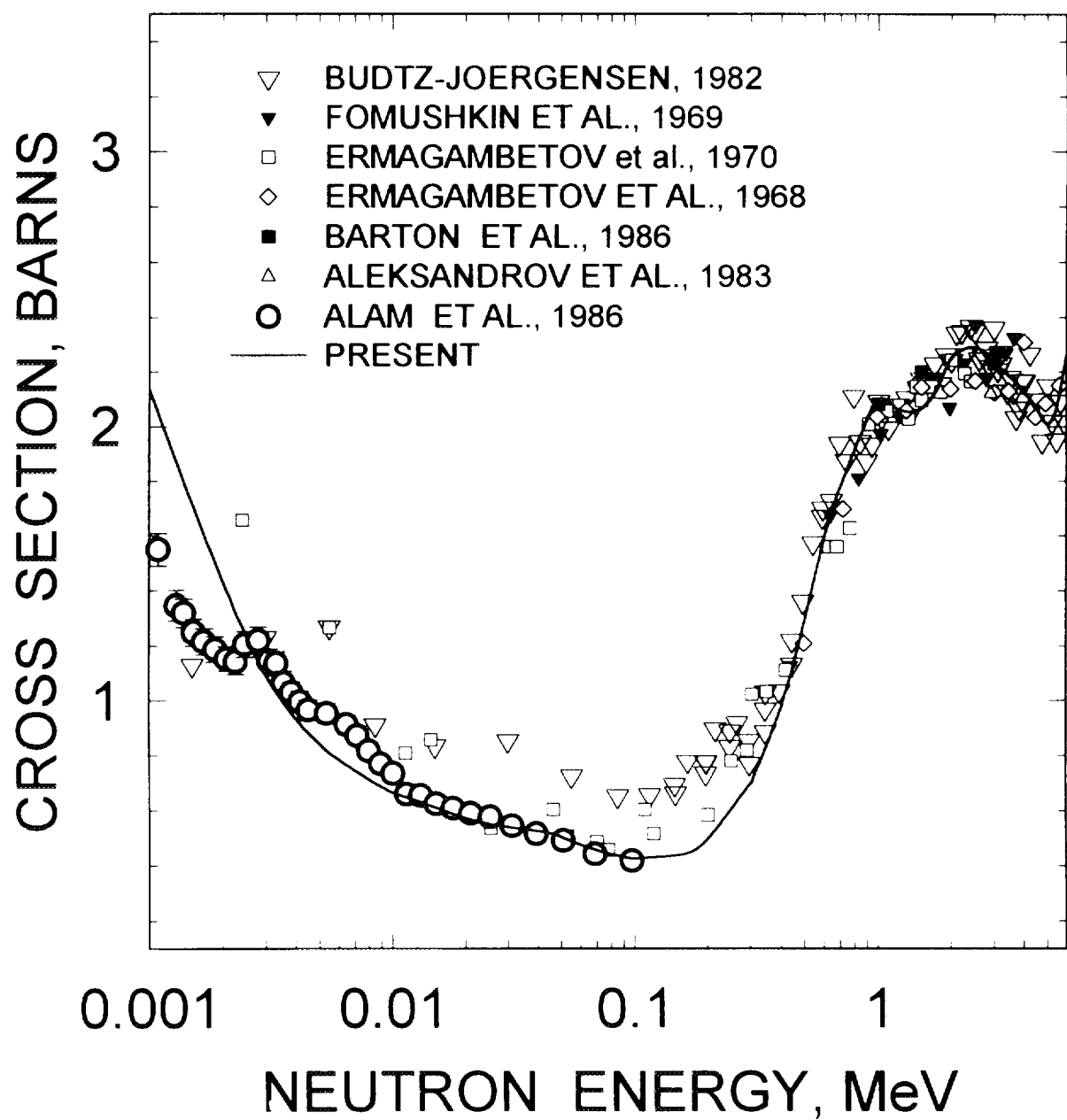


FIG. 4.4

## $^{238}\text{Pu}$ FISSION CROSS SECTION

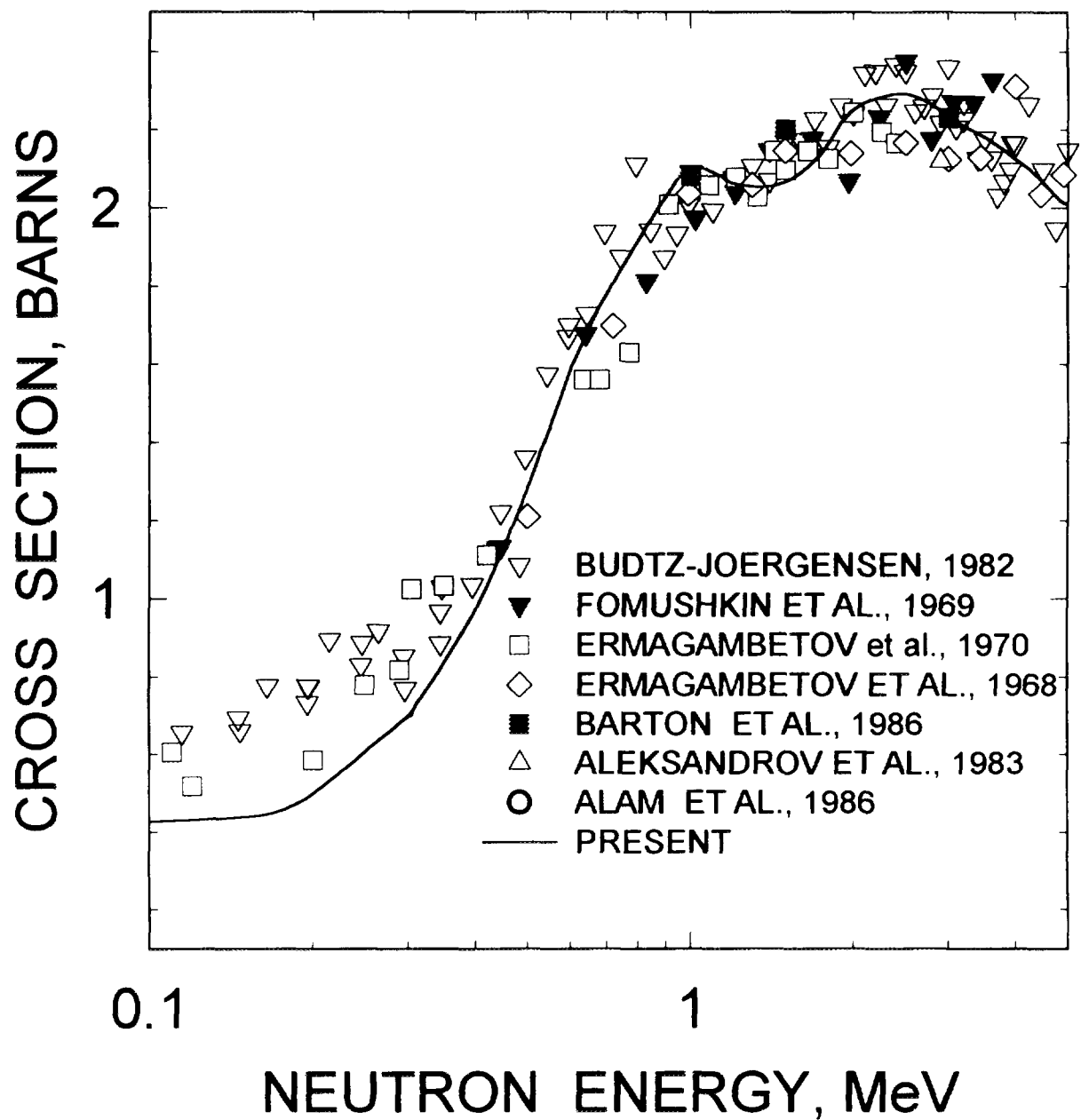


FIG. 4.5

## $^{238}\text{Pu}$ FISSION CROSS SECTION

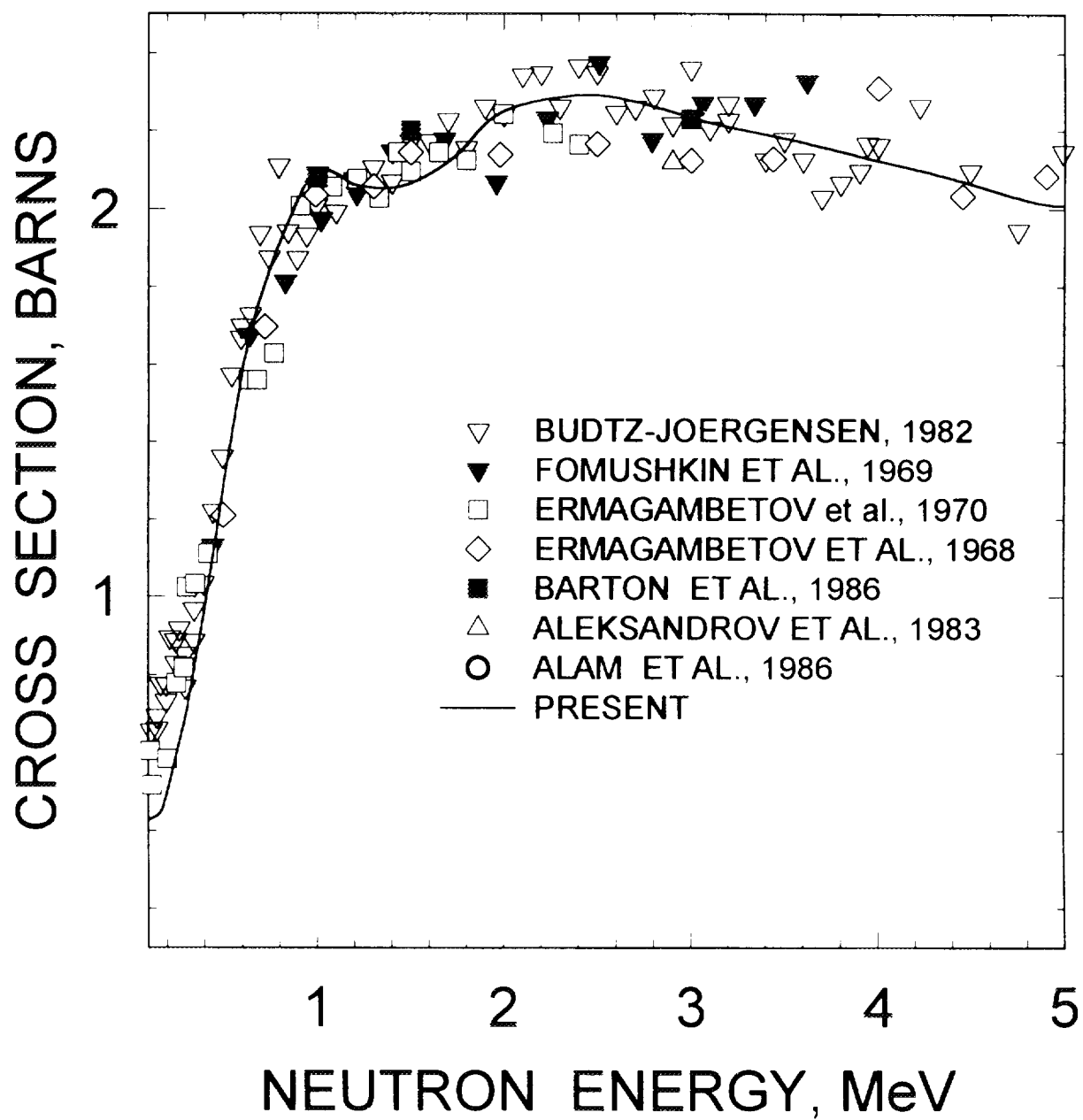


FIG. 4.6

## $^{238}\text{Pu}$ FISSION CROSS SECTION

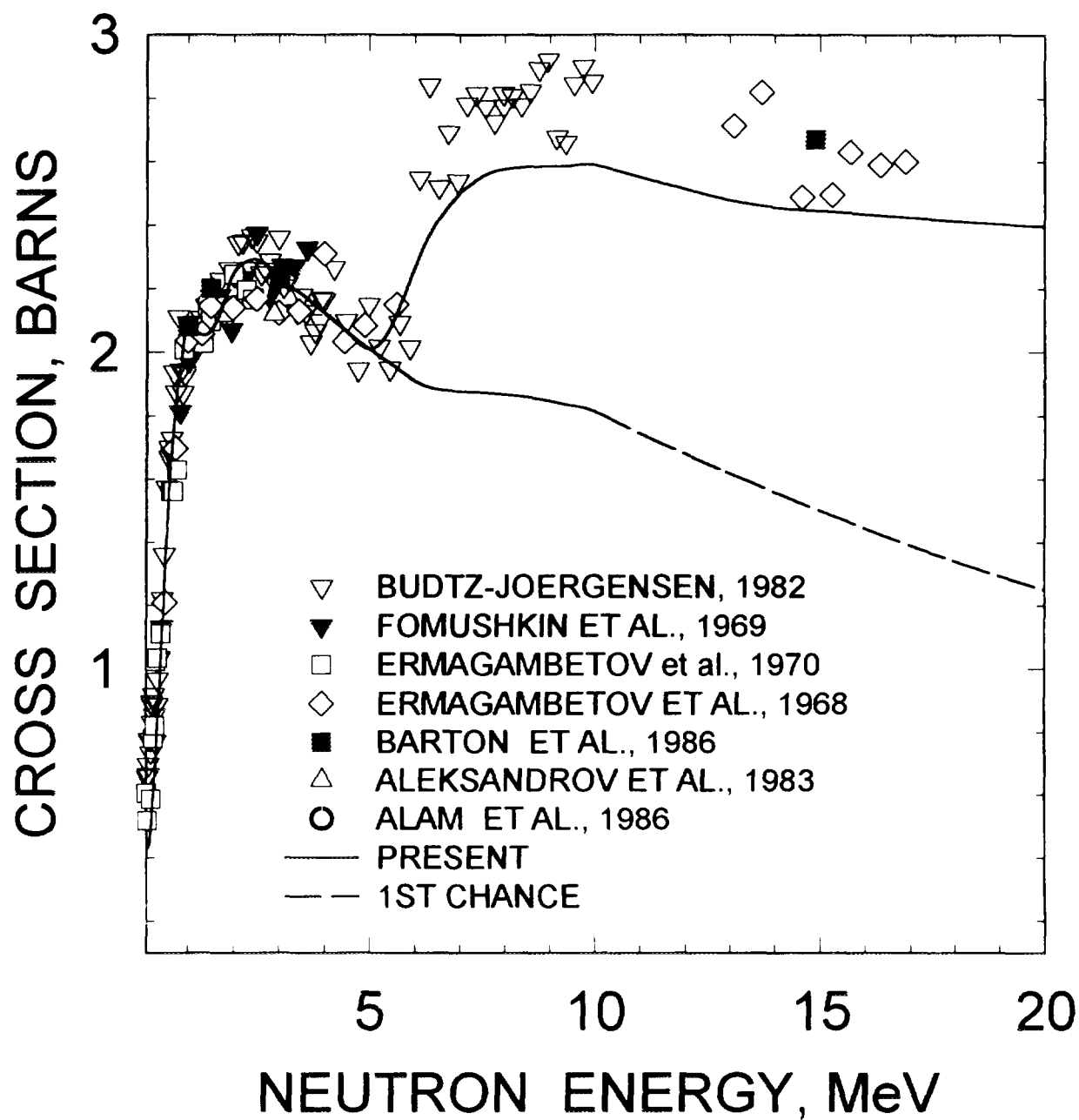


FIG. 4.7

# $^{237}\text{Pu}$ FISSION CROSS SECTION

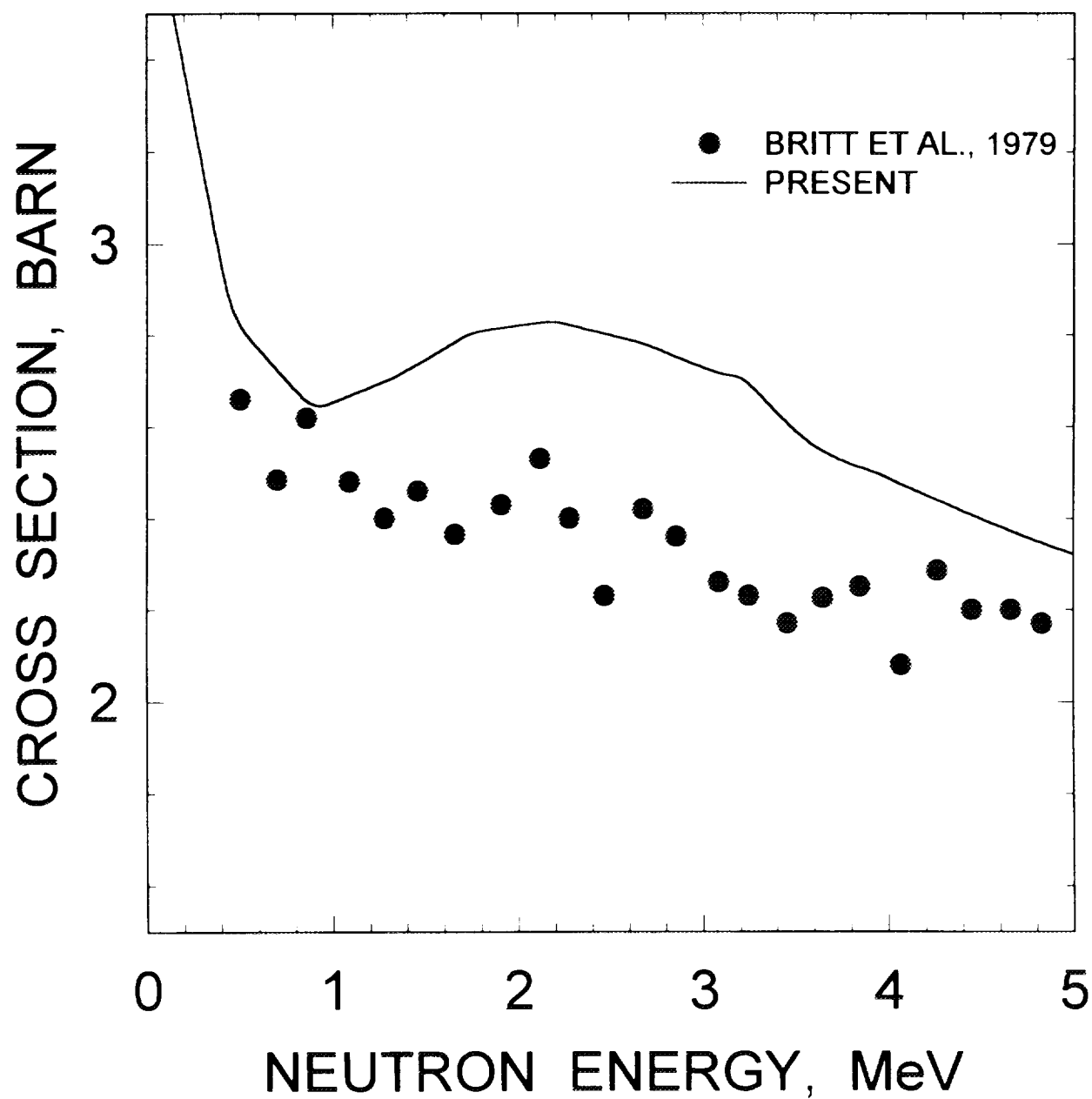


FIG. 4.8

# $^{236}\text{Pu}$ FISSION CROSS SECTION

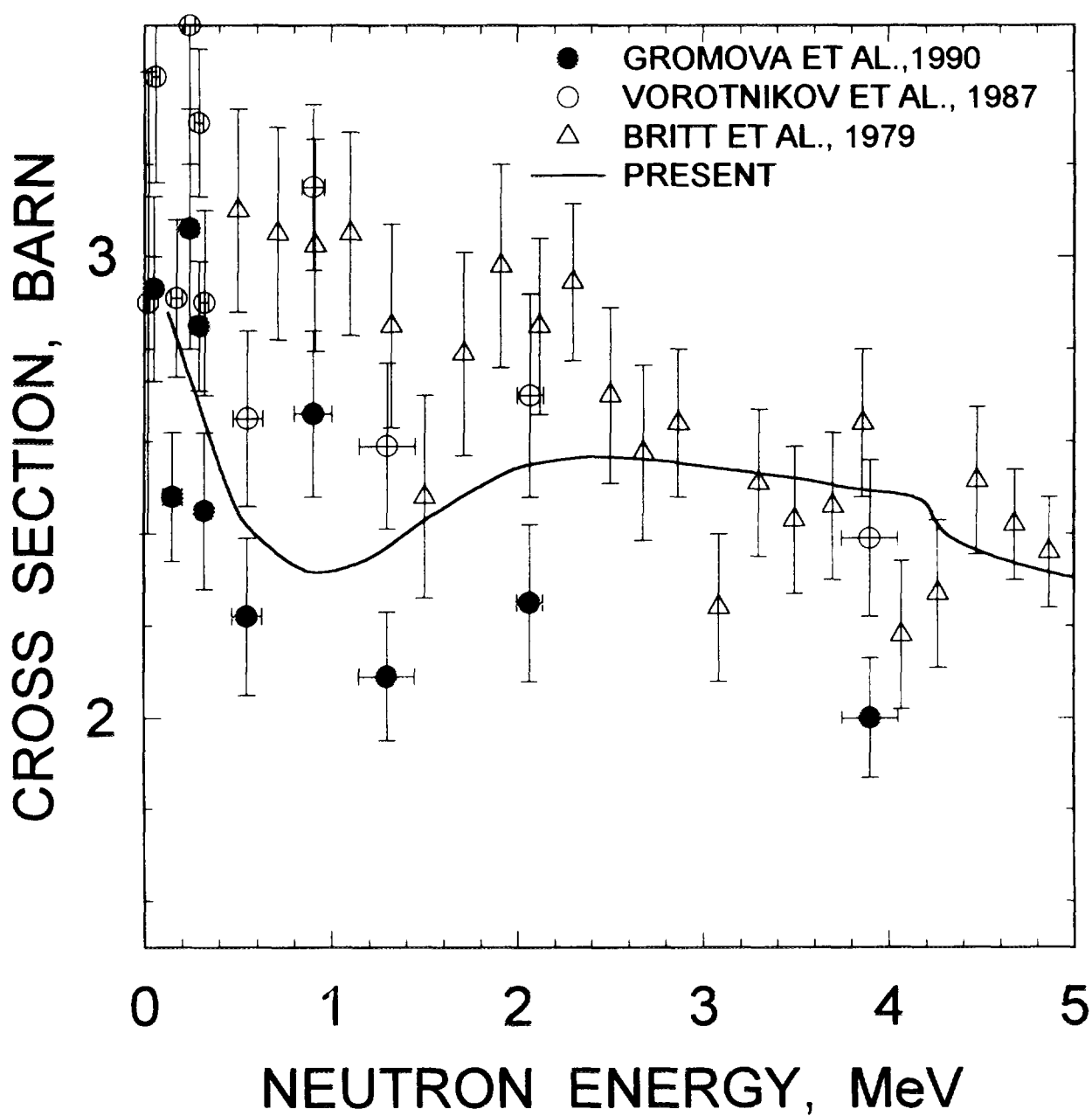


FIG. 4.9

# $^{238}\text{Pu}$ FISSION CROSS SECTION

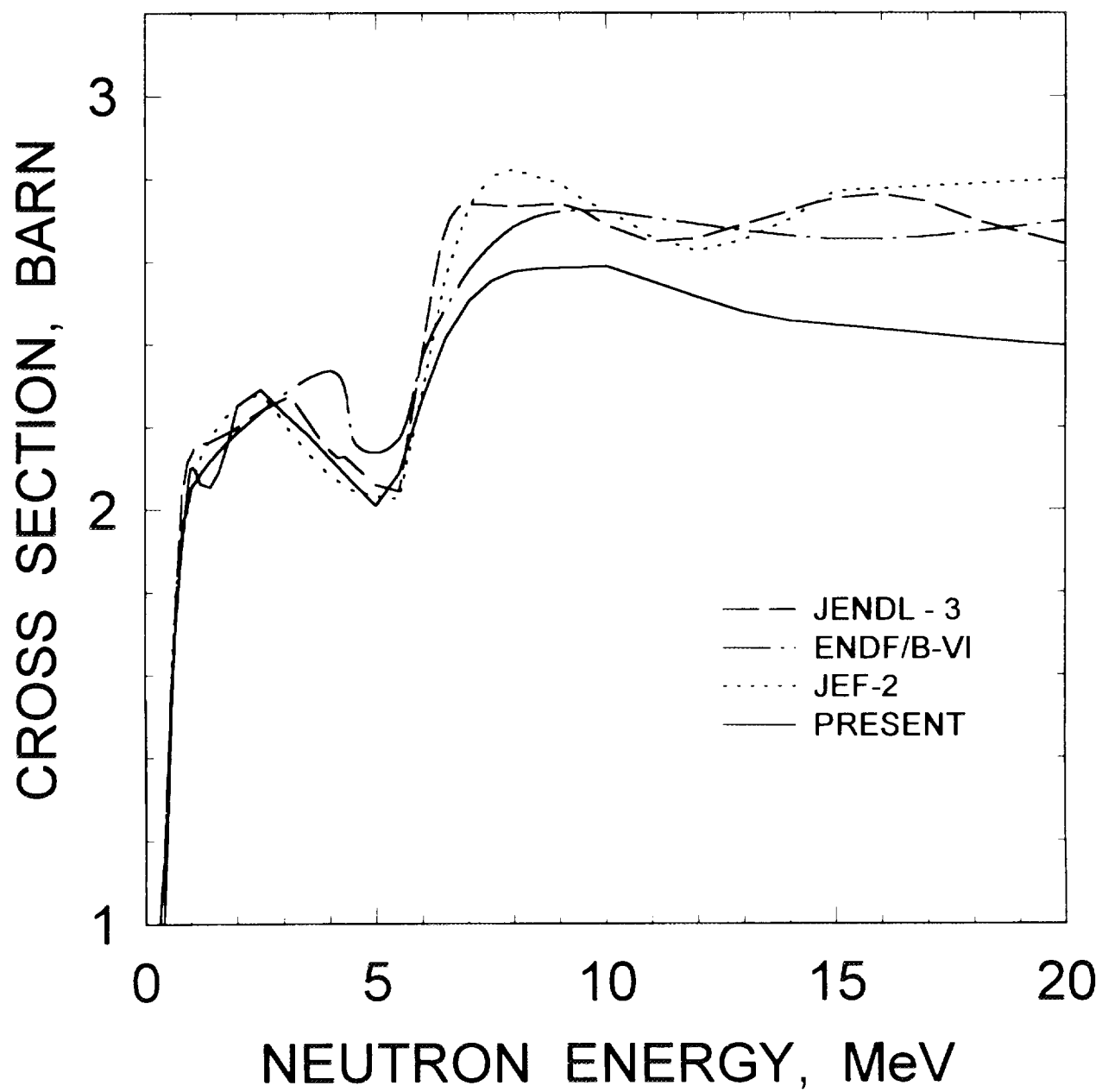


FIG. 4.10



$^{238}\text{Pu}$

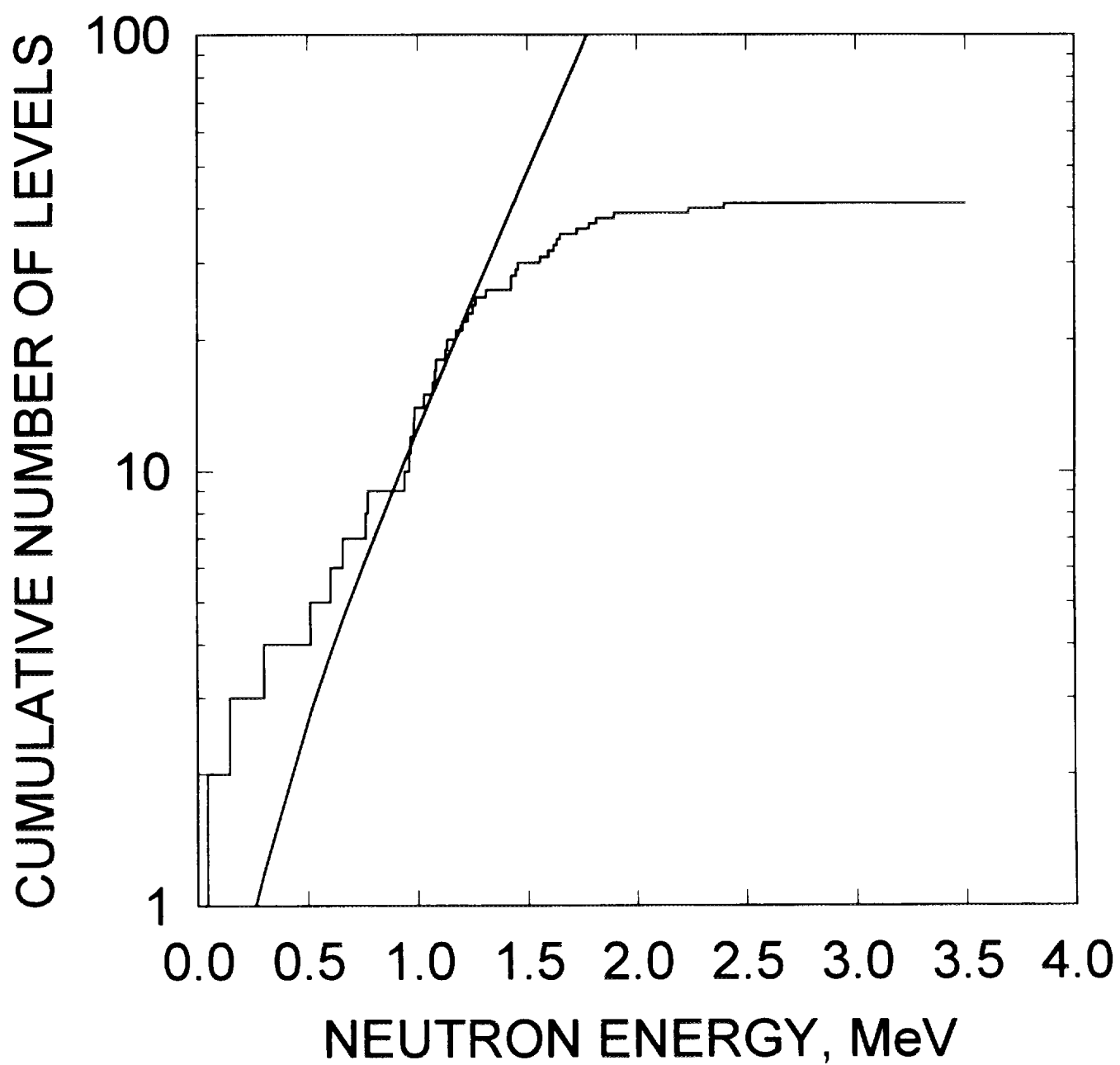


FIG. 4.11

## $^{238}\text{Pu}$ INELASTIC CROSS SECTION

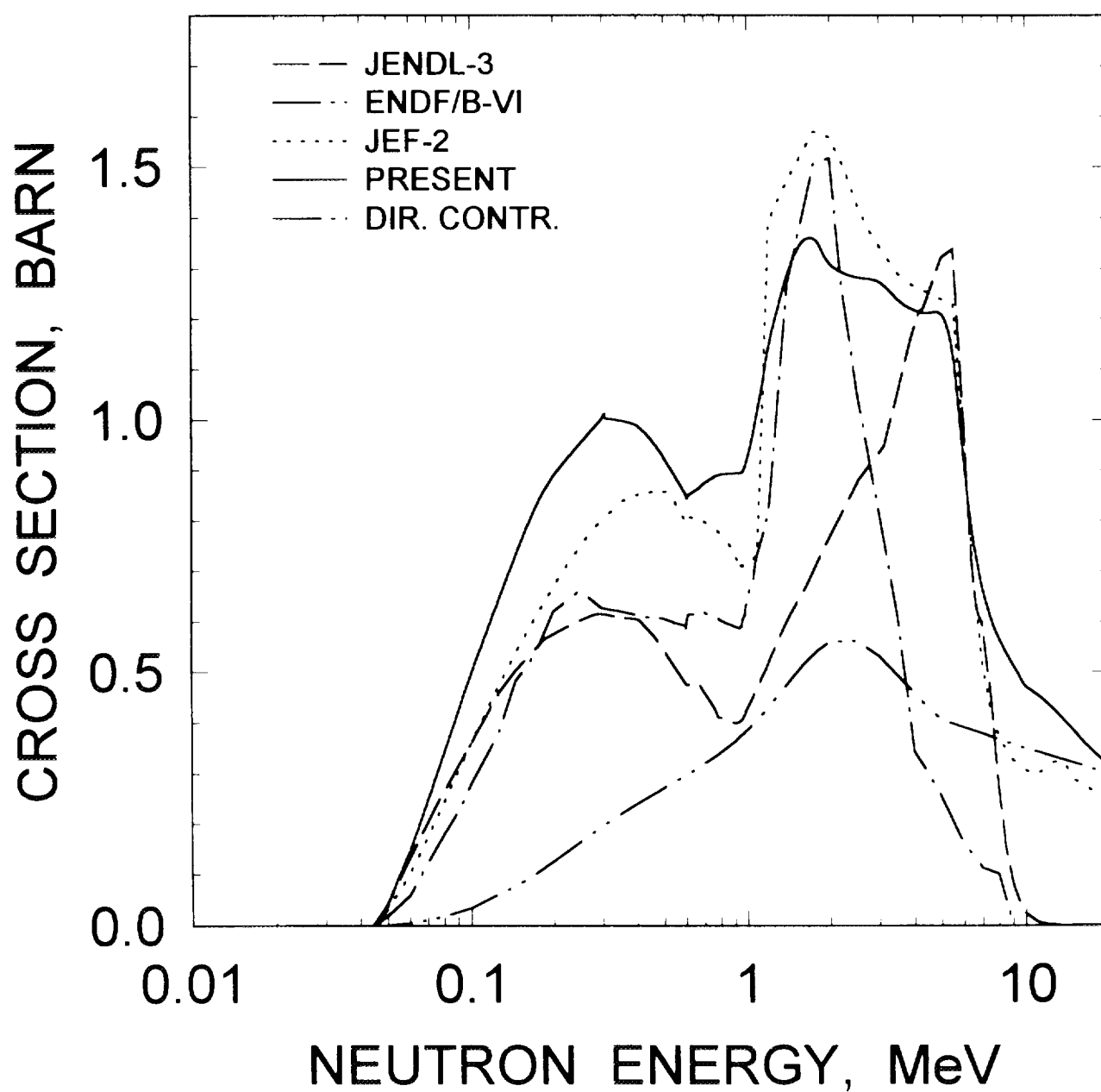


FIG. 4.12

$^{238}\text{Pu}$  INELASTIC SCATTERING  
IN CONTINUUM

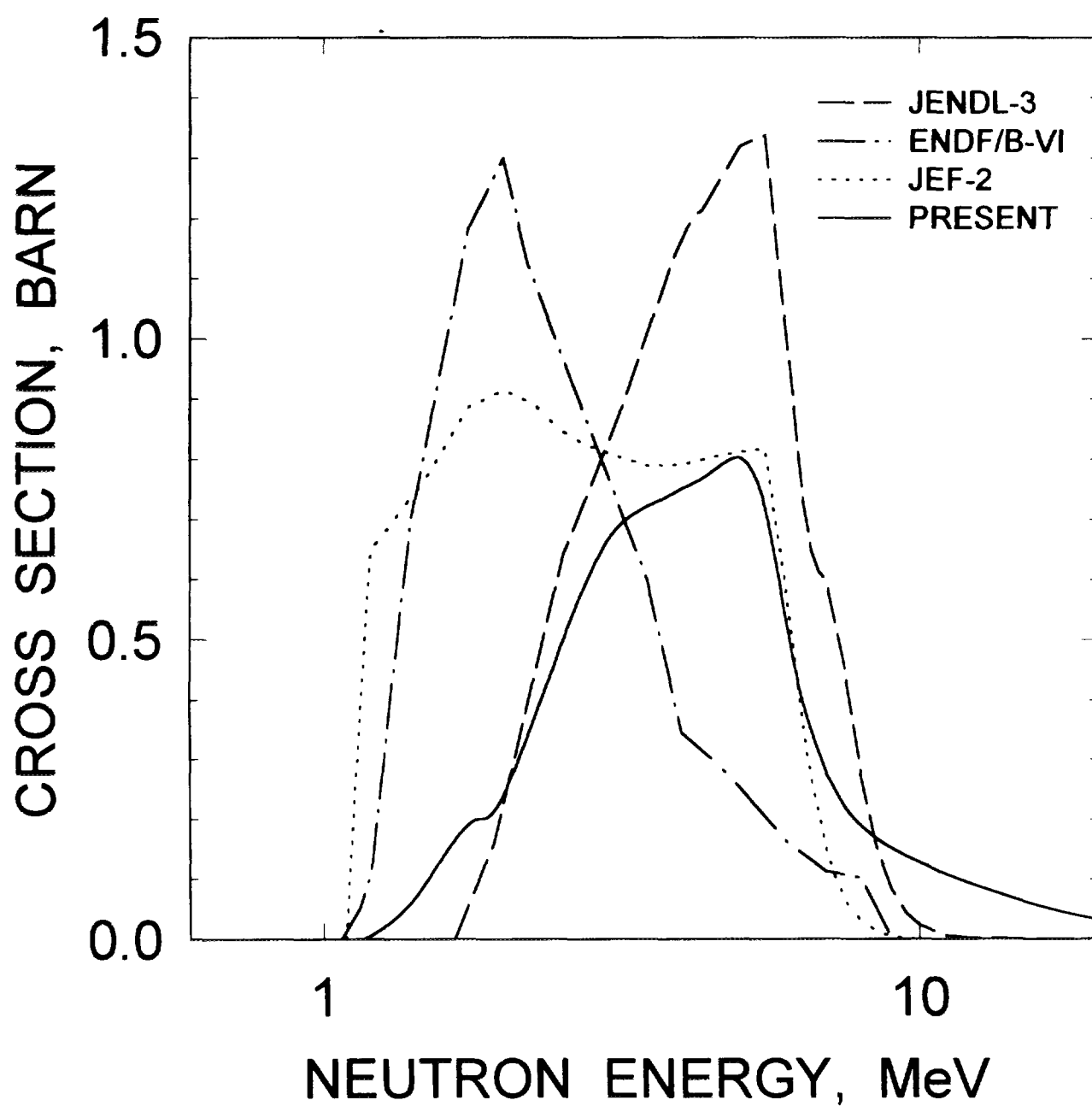


FIG. 4.13

$^{239}\text{Pu}$

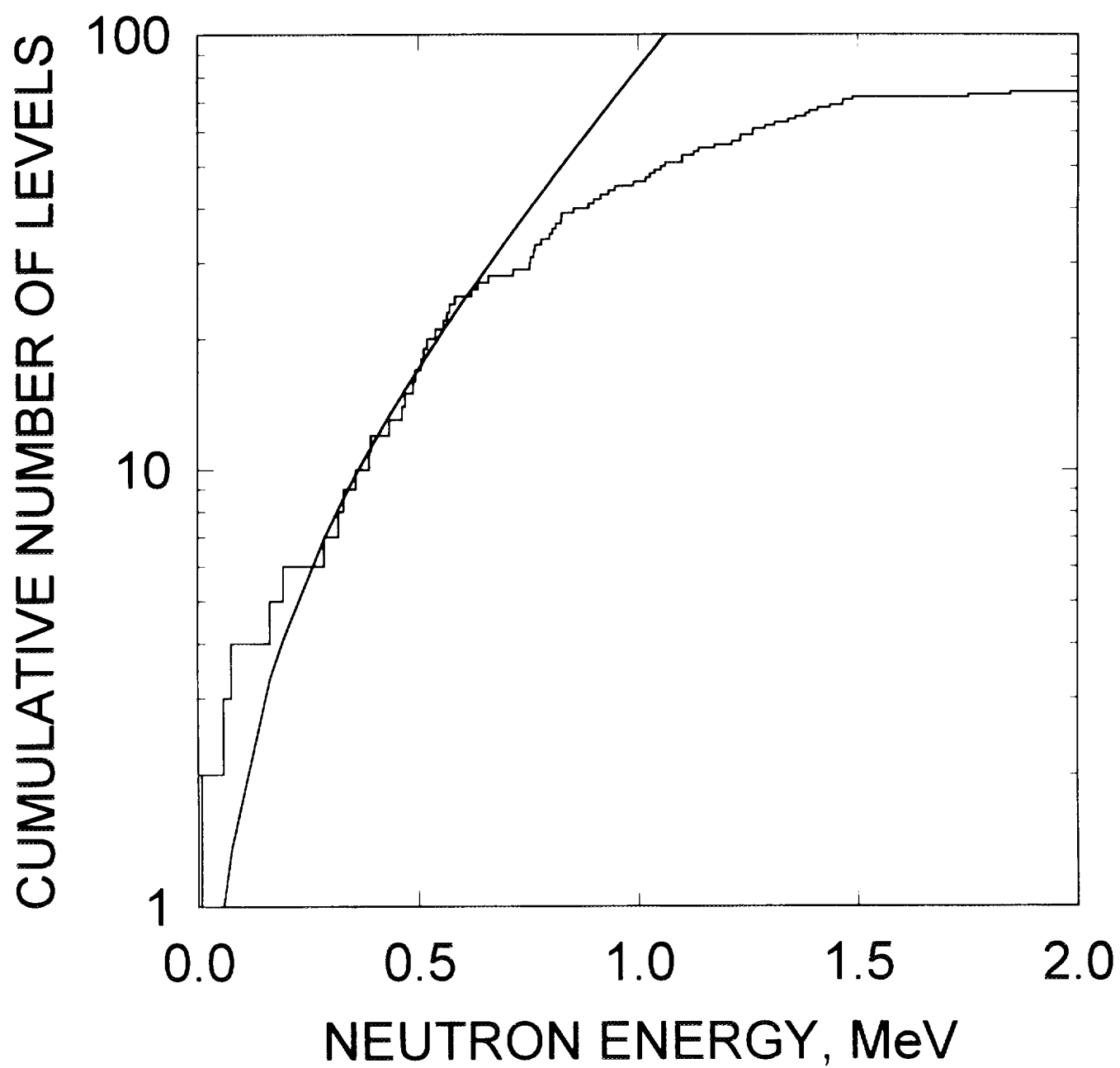


FIG. 4.14

$^{238}\text{Pu}$ : 0.04408 MeV,  $2^+$  LEVEL EXCITATION

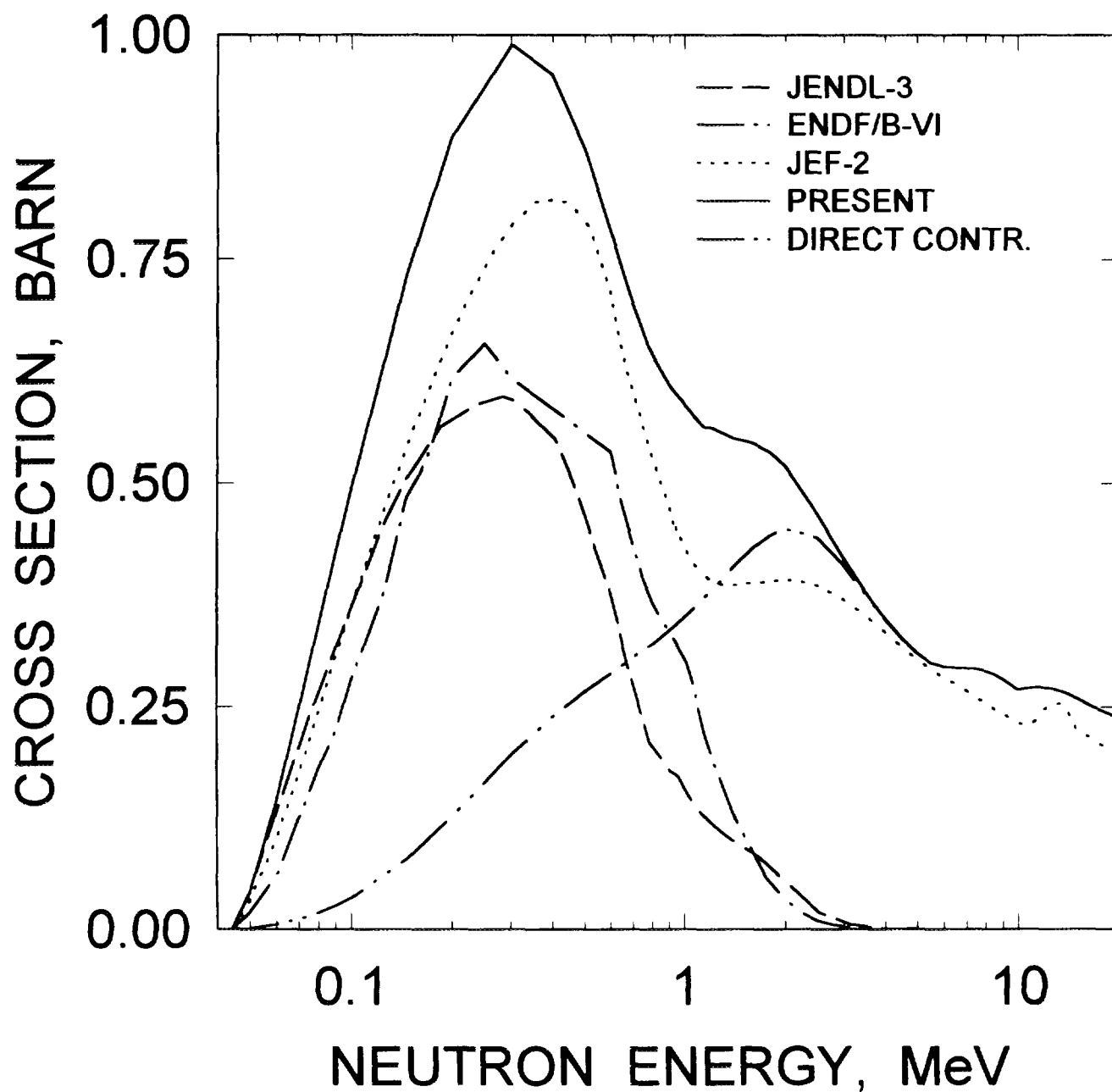


FIG. 4.15

$^{238}\text{Pu}$ : 0.14596 MeV,  $4^+$  LEVEL EXCITATION

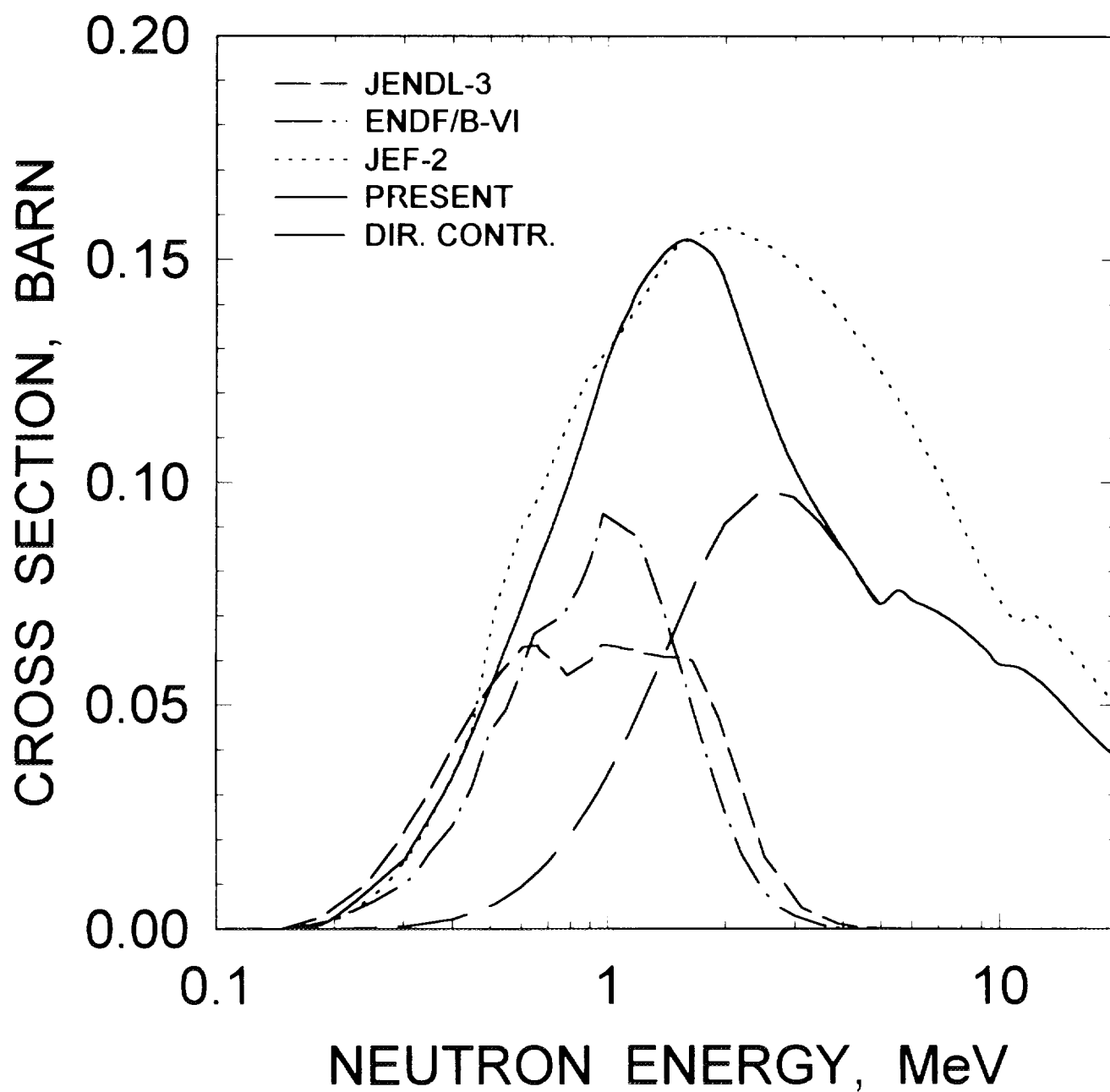


FIG. 4.16

$^{238}\text{Pu}$ : 0.3034 MeV,  $6^+$  LEVEL EXCITATION

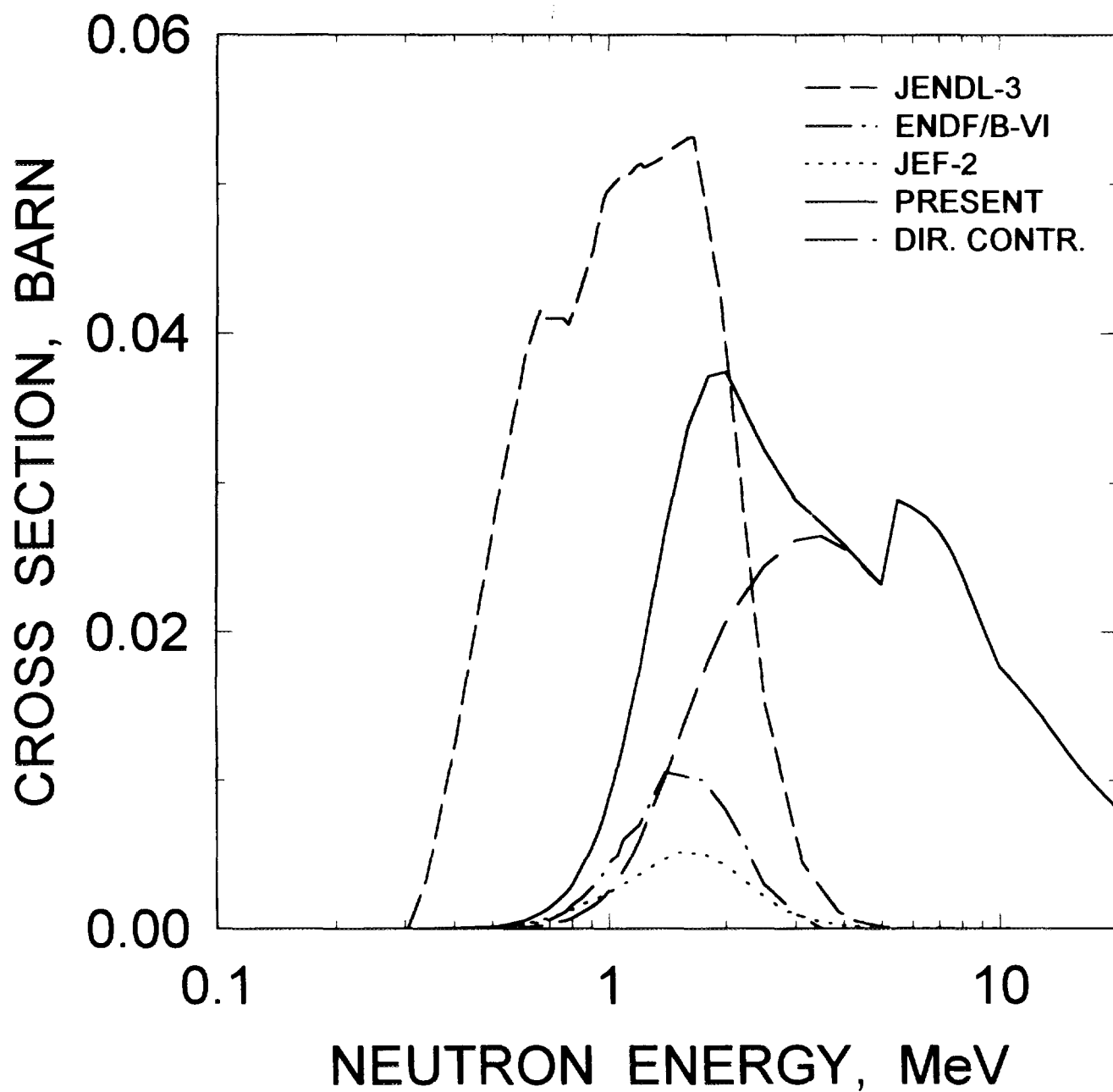


FIG. 4.17

$^{238}\text{Pu}$ : 0.5134 MeV,  $8^+$  LEVEL EXCITATION

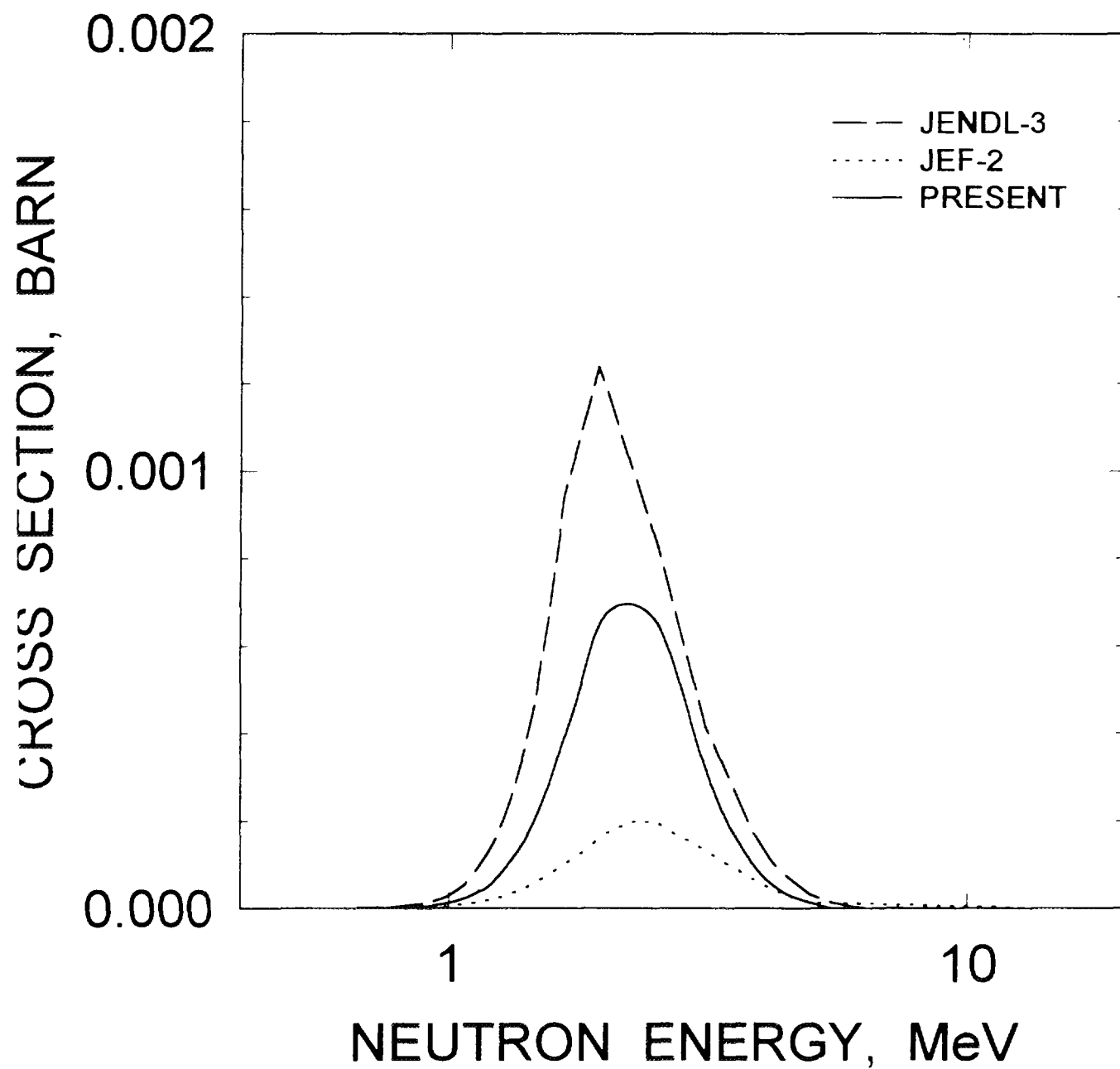


FIG. 4.18



$^{238}\text{Pu}$ : 0.60518 MeV,  $1^-$  LEVEL EXCITATION

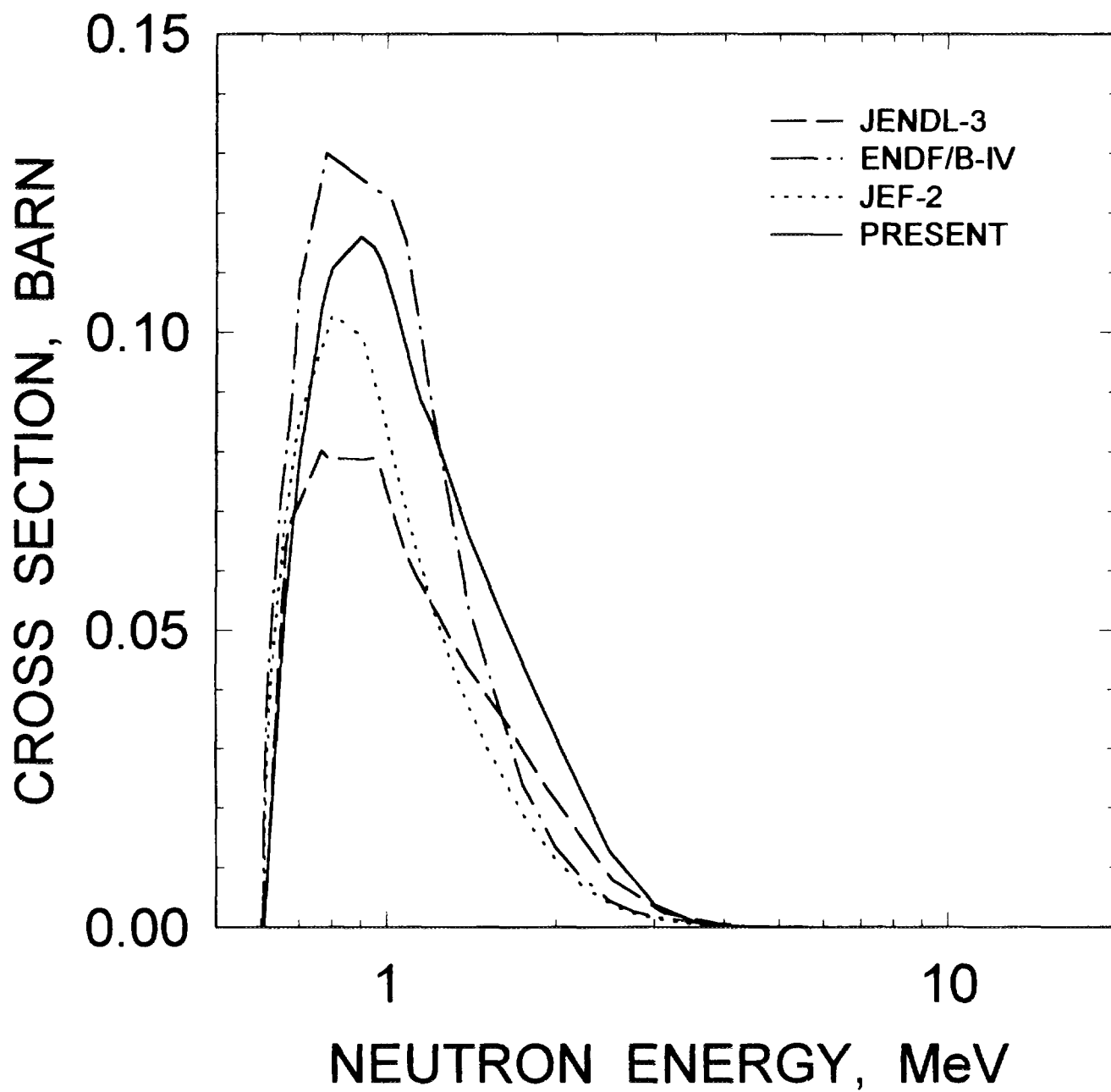


FIG. 4.19

$^{238}\text{Pu}$ : 0.66143 MeV,  $3^-$  LEVEL EXCITATION

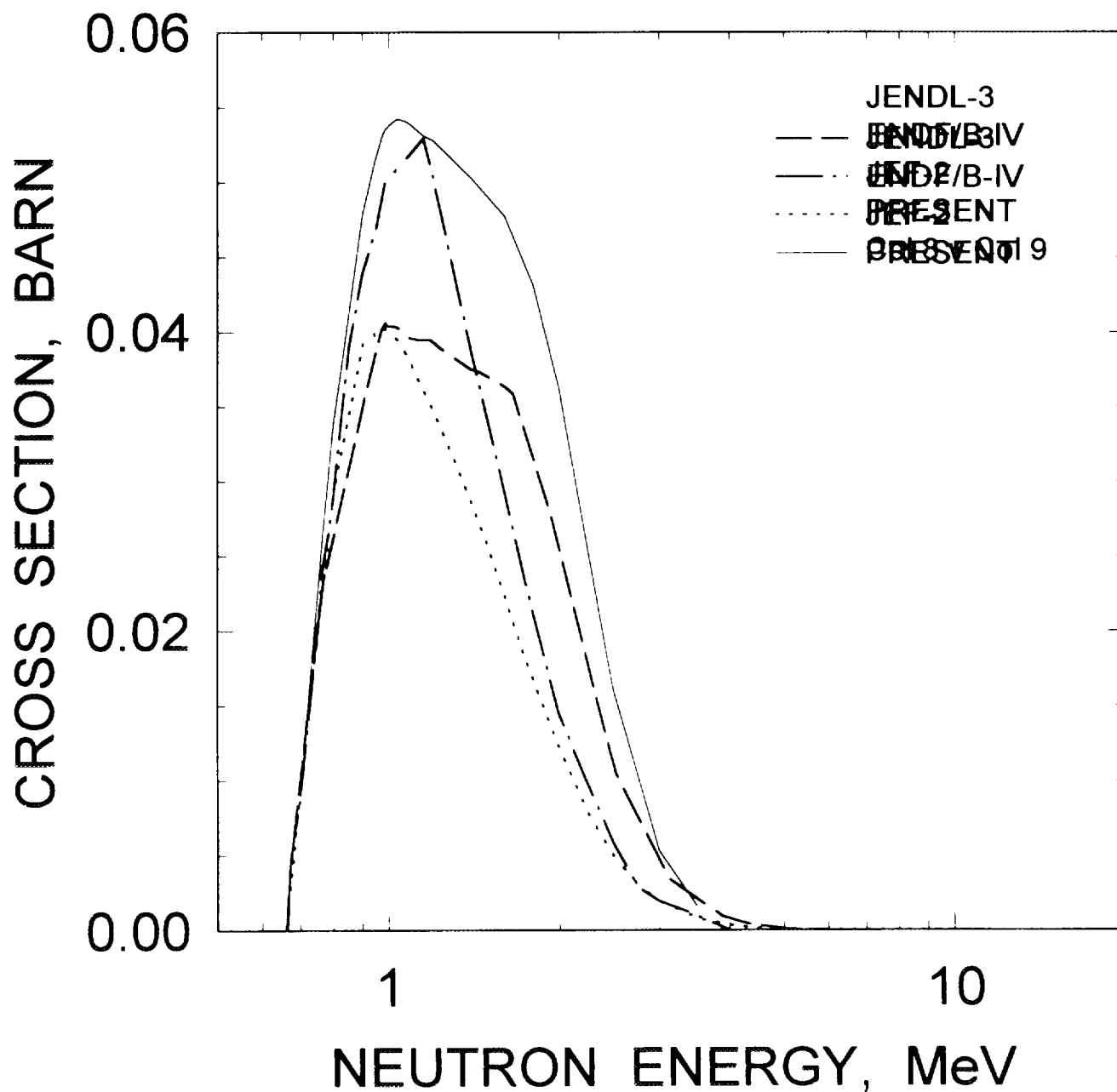


FIG. 4.20

# $^{238}\text{Pu}$ CAPTURE CROSS SECTION

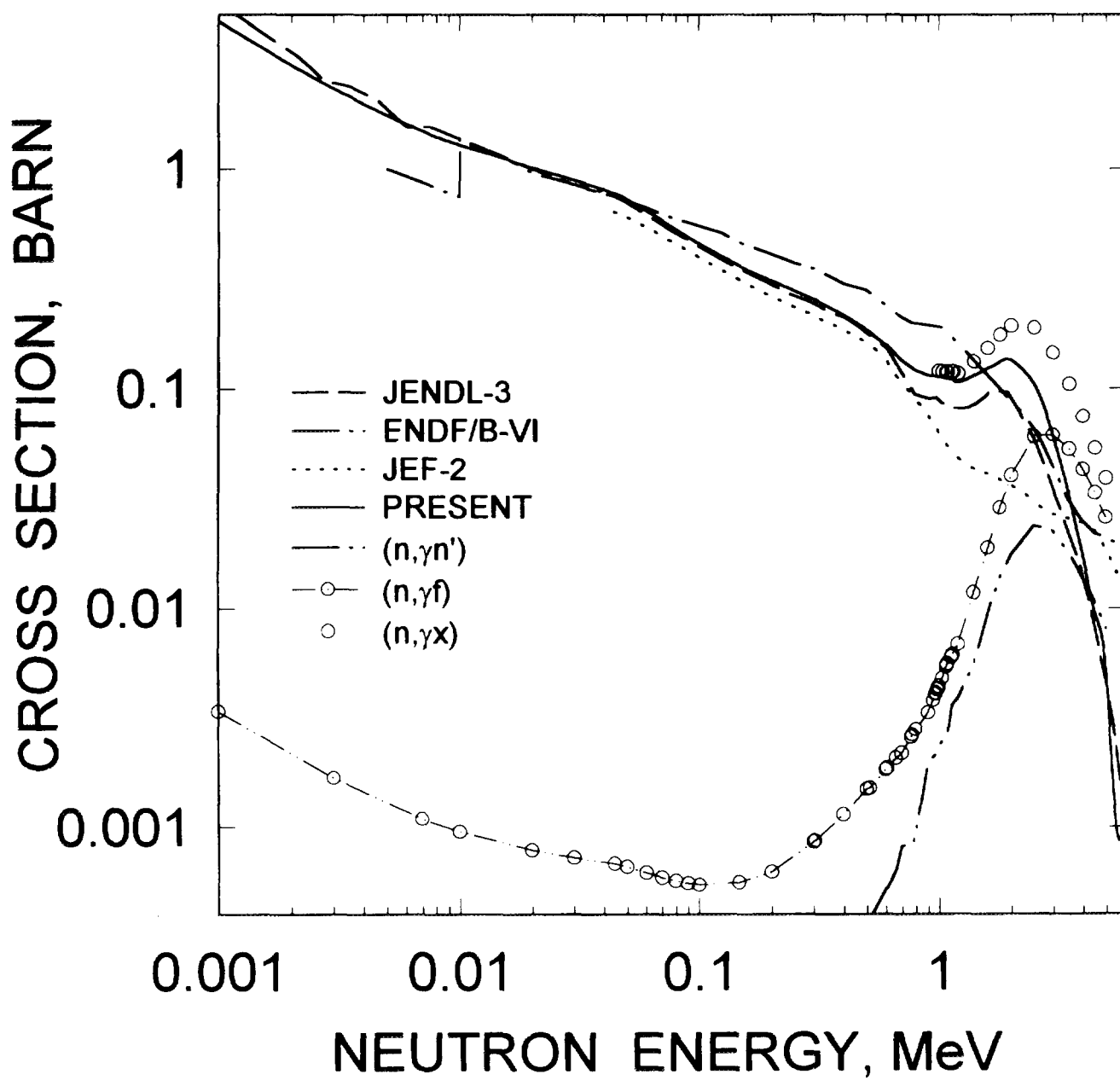


FIG. 4.21

# $^{238}\text{Pu}$ (n,2n) CROSS SECTION

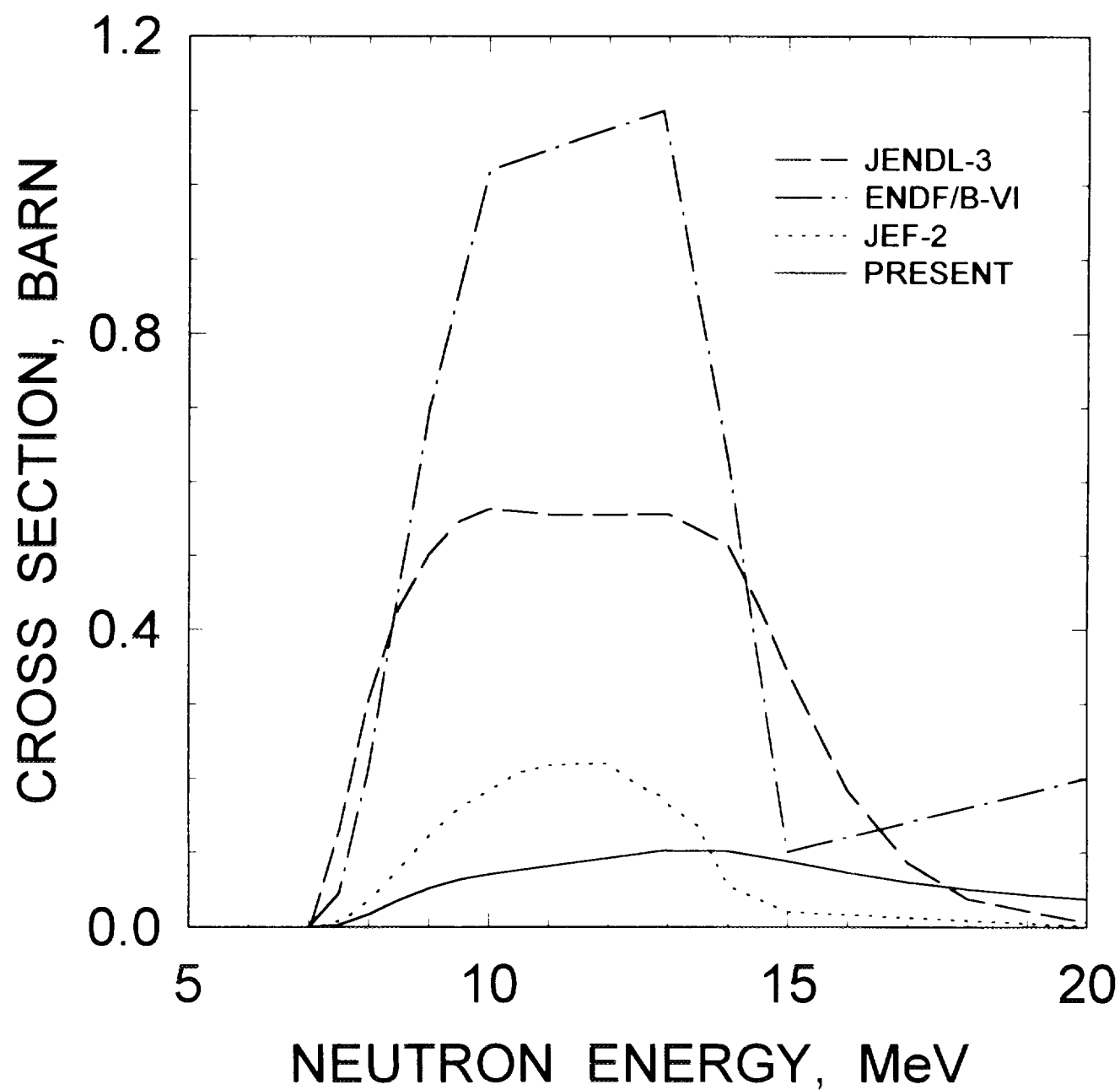


FIG. 4.22

# $^{238}\text{Pu}(n,3n)$ CROSS SECTION

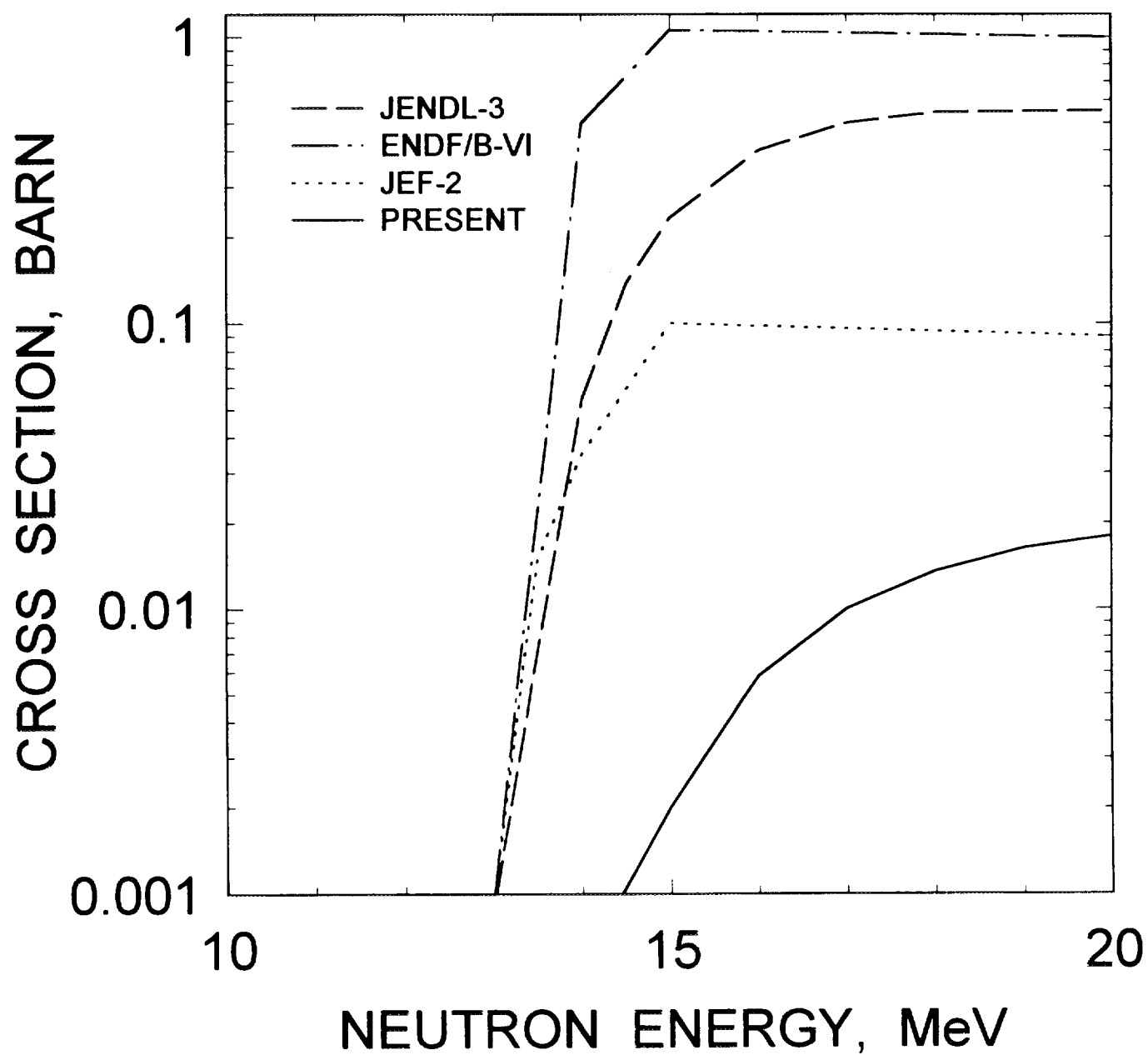


FIG. 4.23

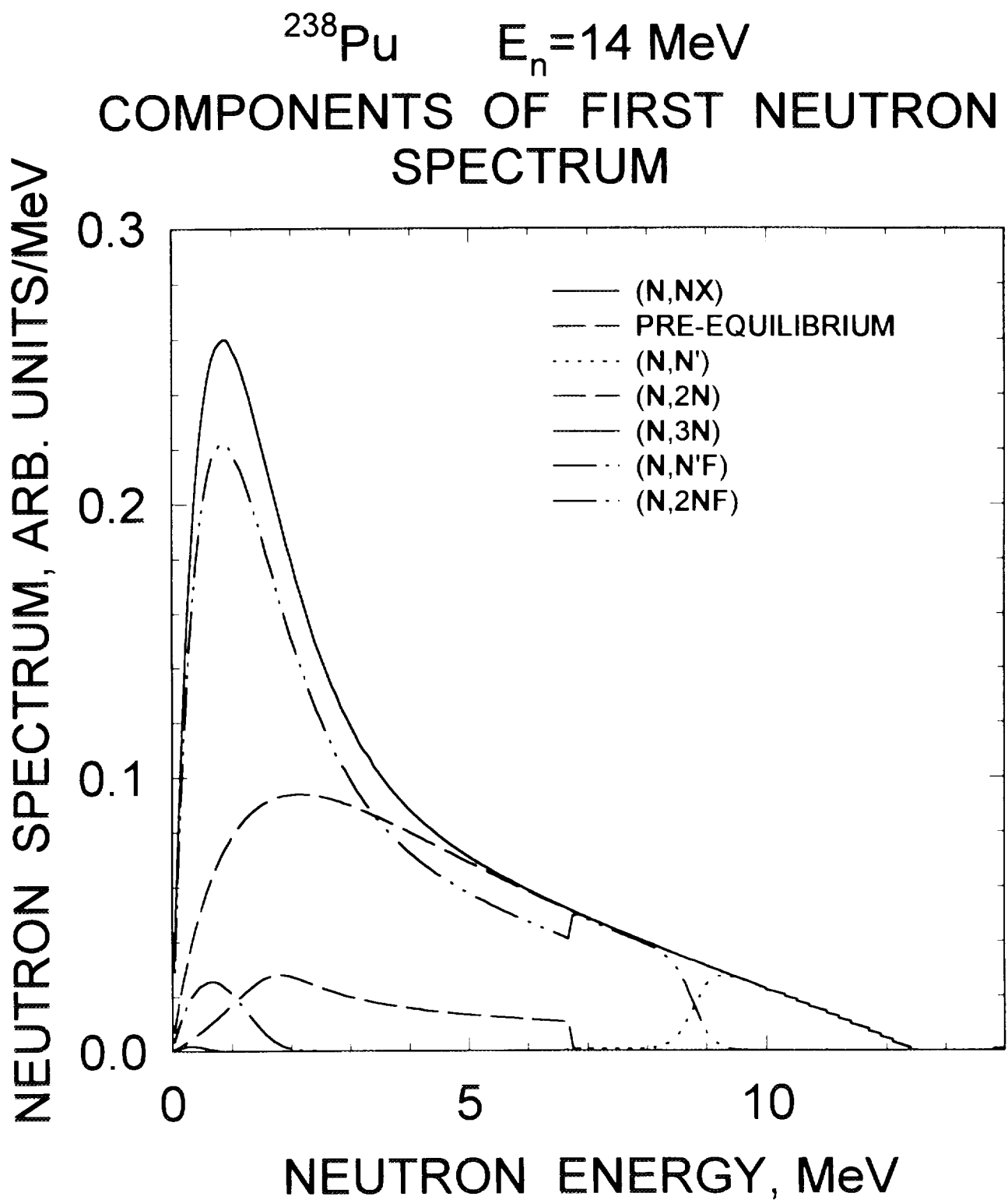


FIG.5.1

$^{238}\text{Pu}$   $E_n = 14 \text{ MeV}$   
COMPONENTS OF SECOND NEUTRON  
SPECTRUM

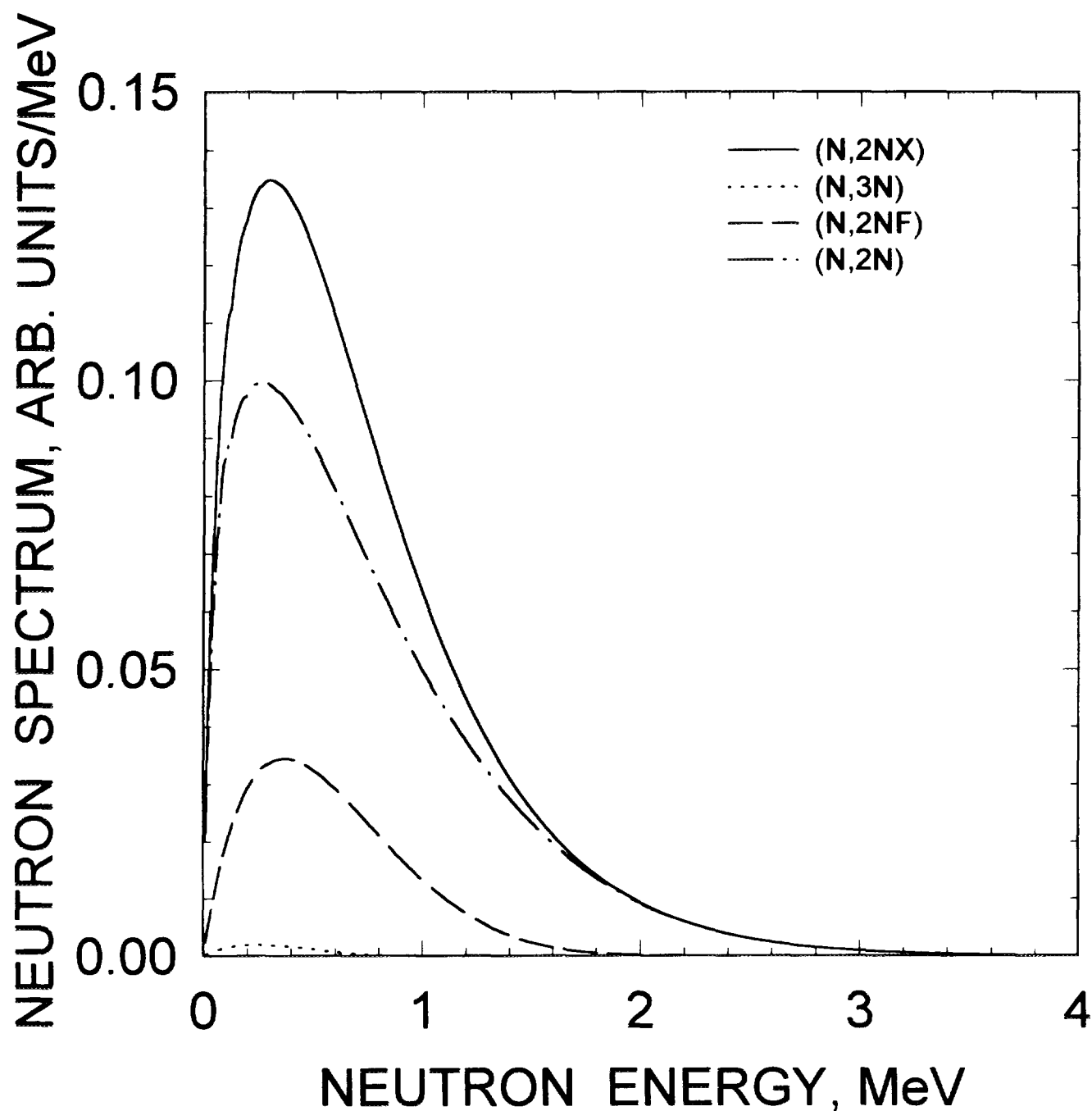


FIG.5.2

$^{238}\text{Pu}$   $E_n = 8 \text{ MeV}$   
COMPARISON WITH JENDL-3  
AND ENDF/B-VI

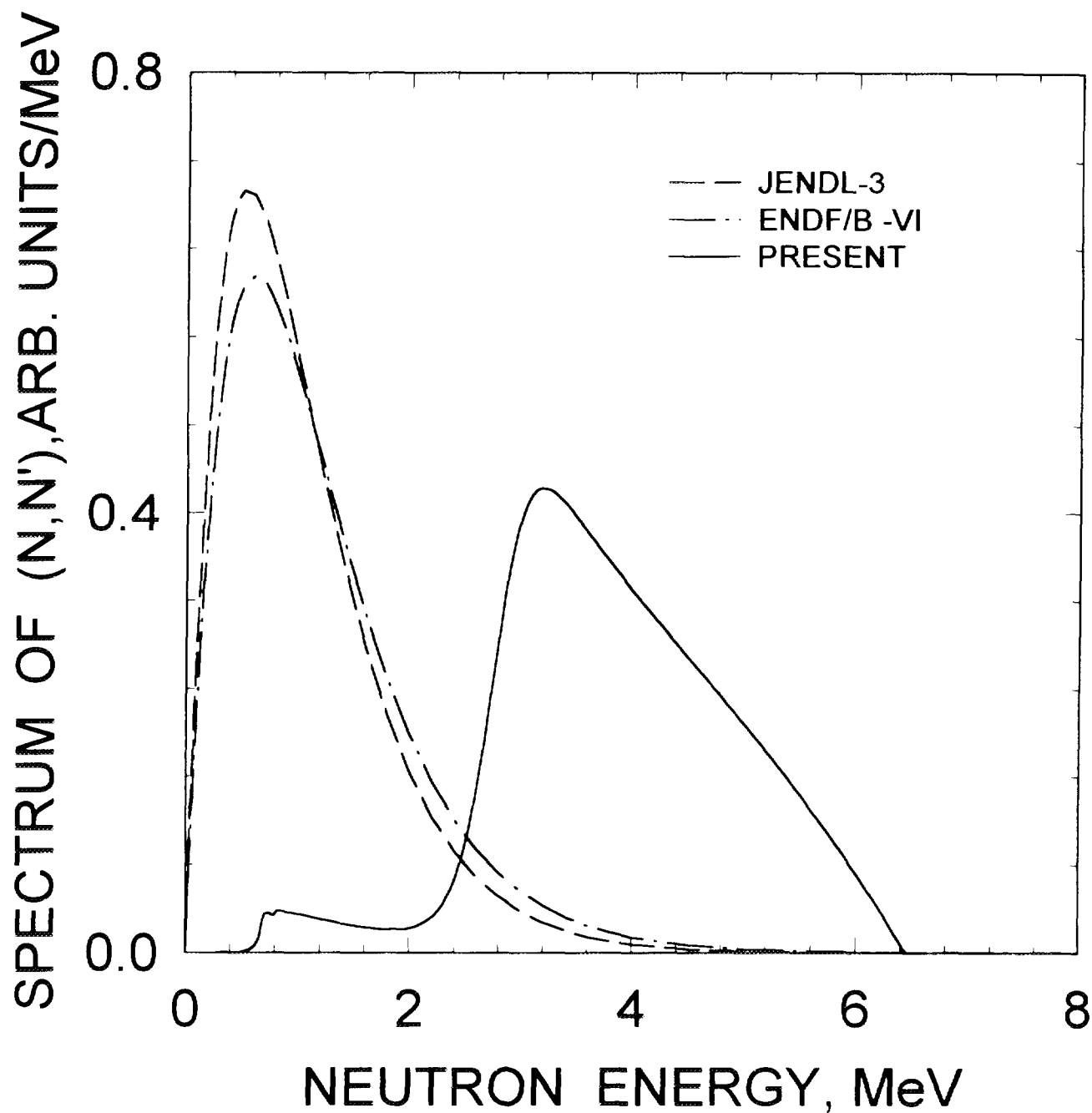


FIG.5.3



$^{238}\text{Pu}$   $E_n=8\text{ MeV}$   
COMPARISON WITH JENDL-3  
AND ENDF/B-VI

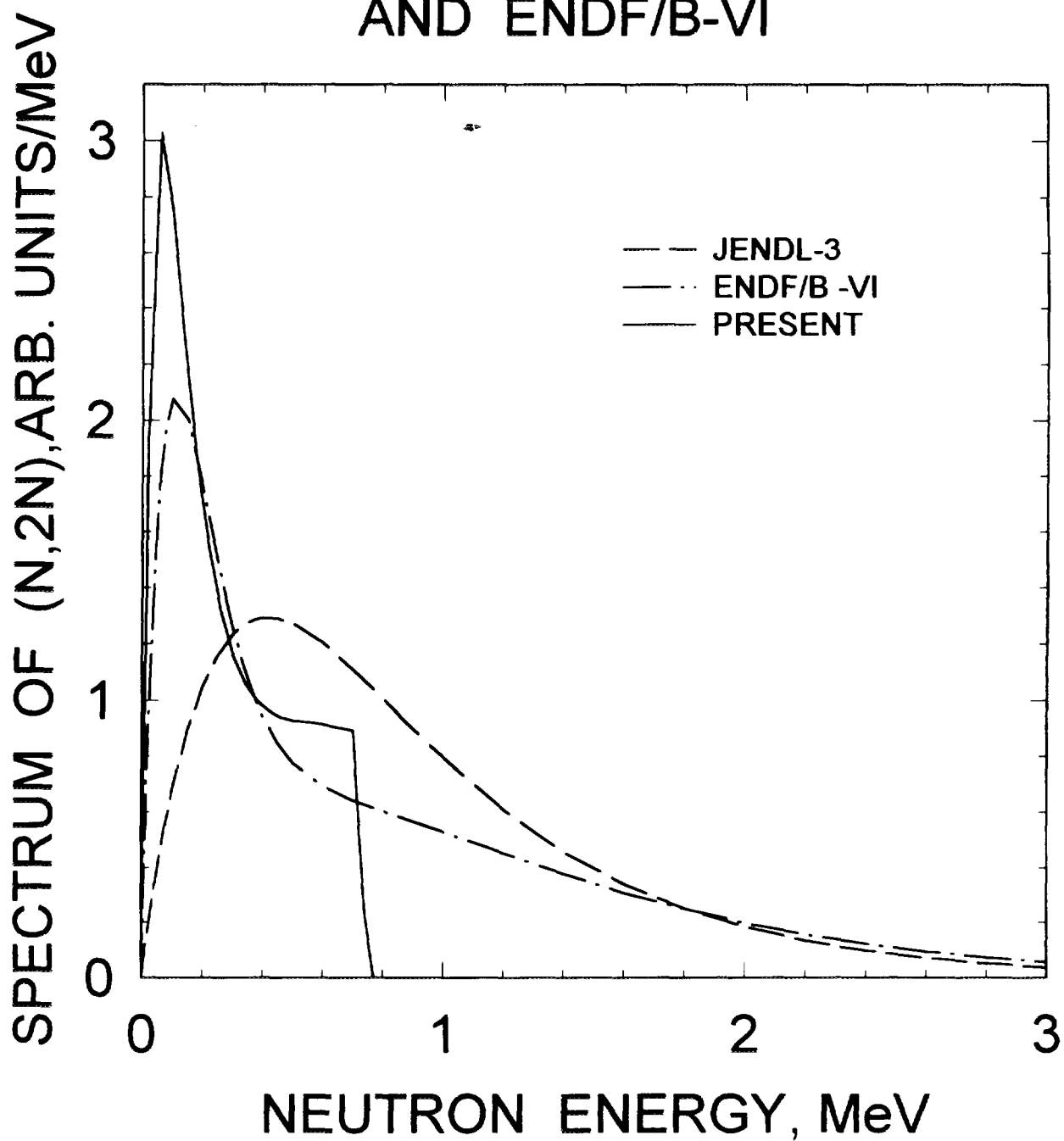


FIG.5.4

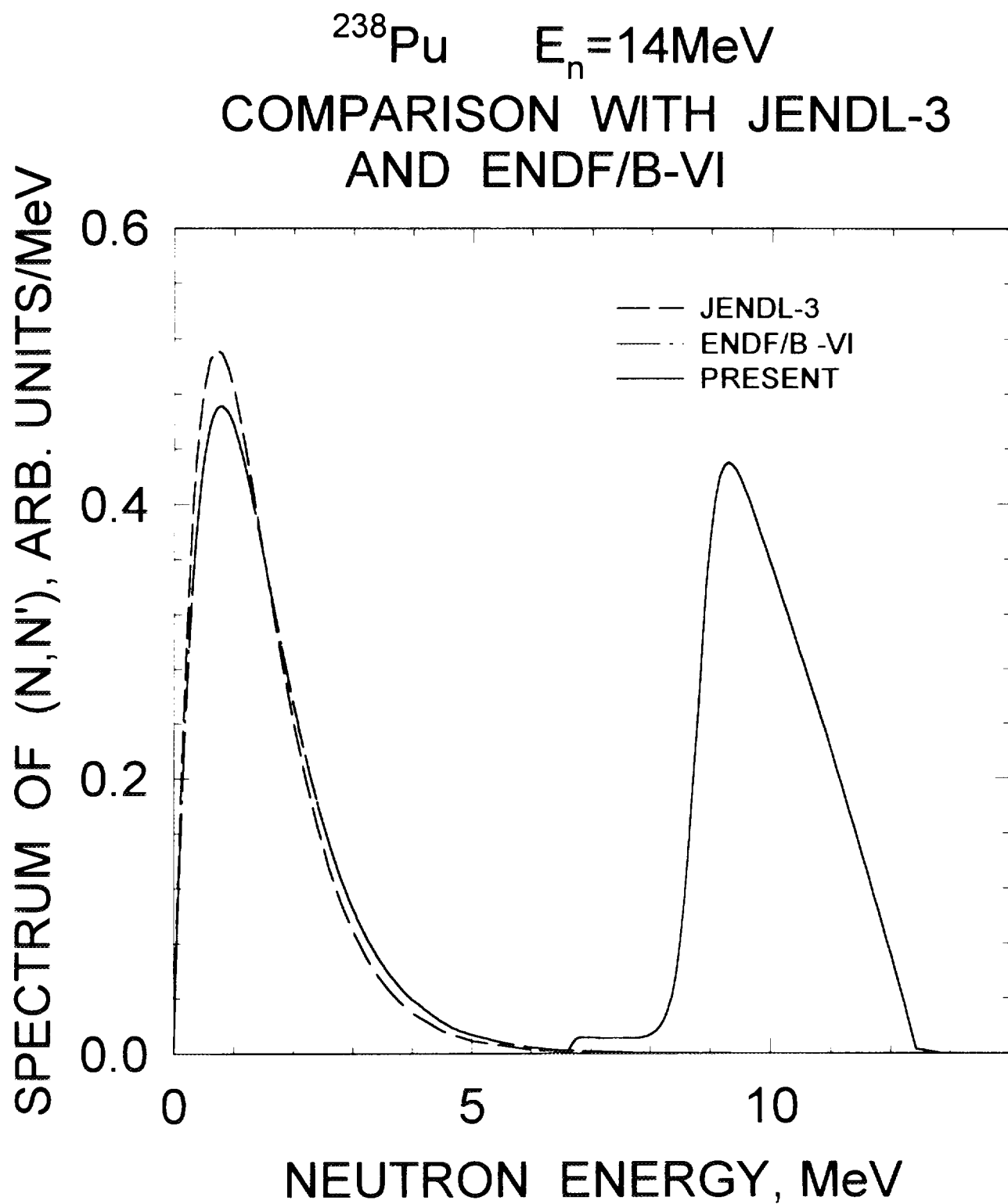


FIG.5.5

$^{238}\text{Pu}$   $E_n=14$  MeV  
COMPARISON WITH JENDL-3  
AND ENDF/B-VI

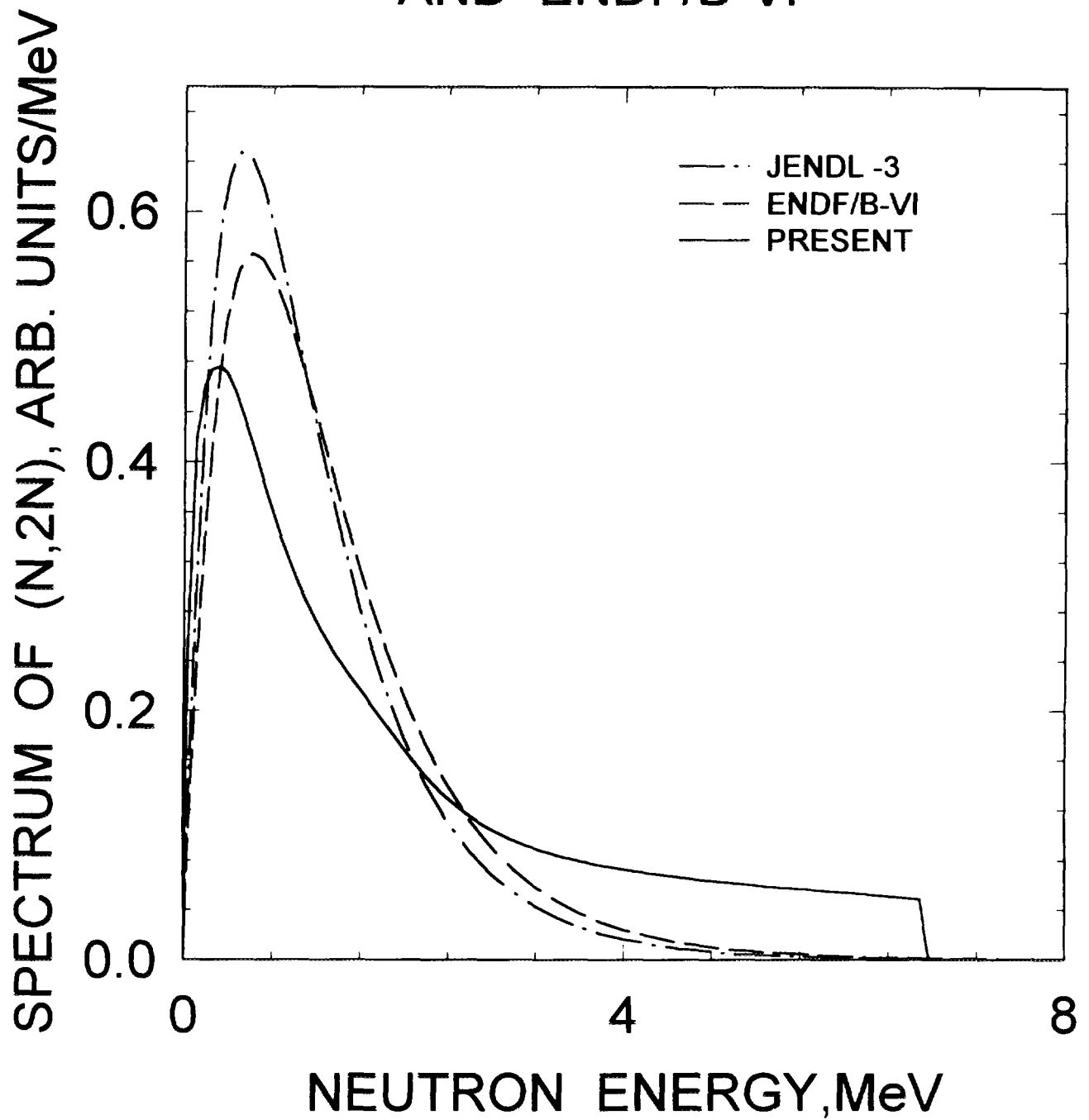


FIG.5.6

$^{238}\text{Pu}$   $E_n = 14 \text{ MeV}$   
COMPARISON WITH JENDL-3.2  
AND ENDF/B-VI

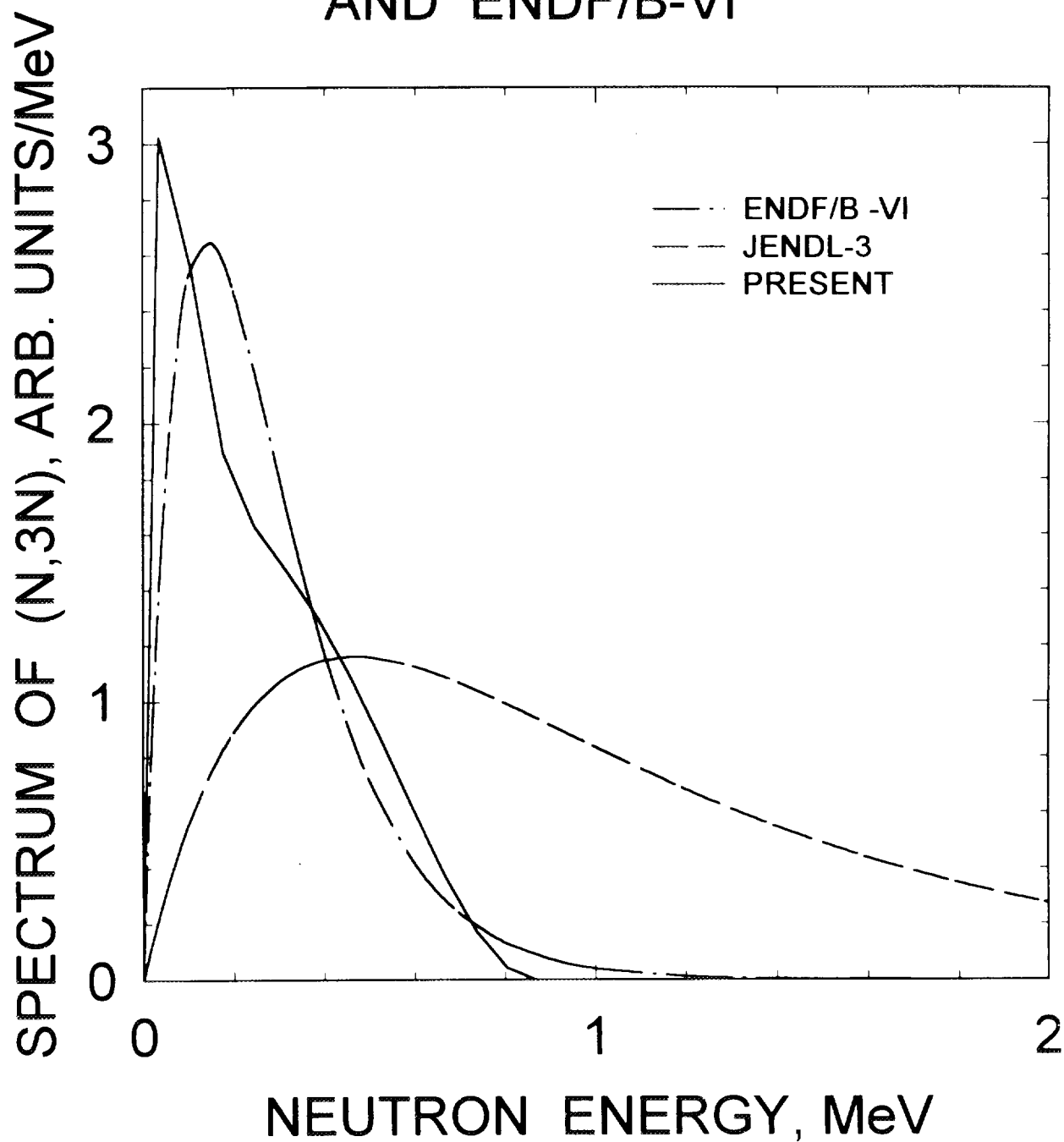


FIG.5.7

$^{238}\text{Pu}$  COMPARISON OF SPECTRA WITH  
DIFFERENT SHAPES OF THE PROMPT  
NEUTRON FISSION SPECTRA

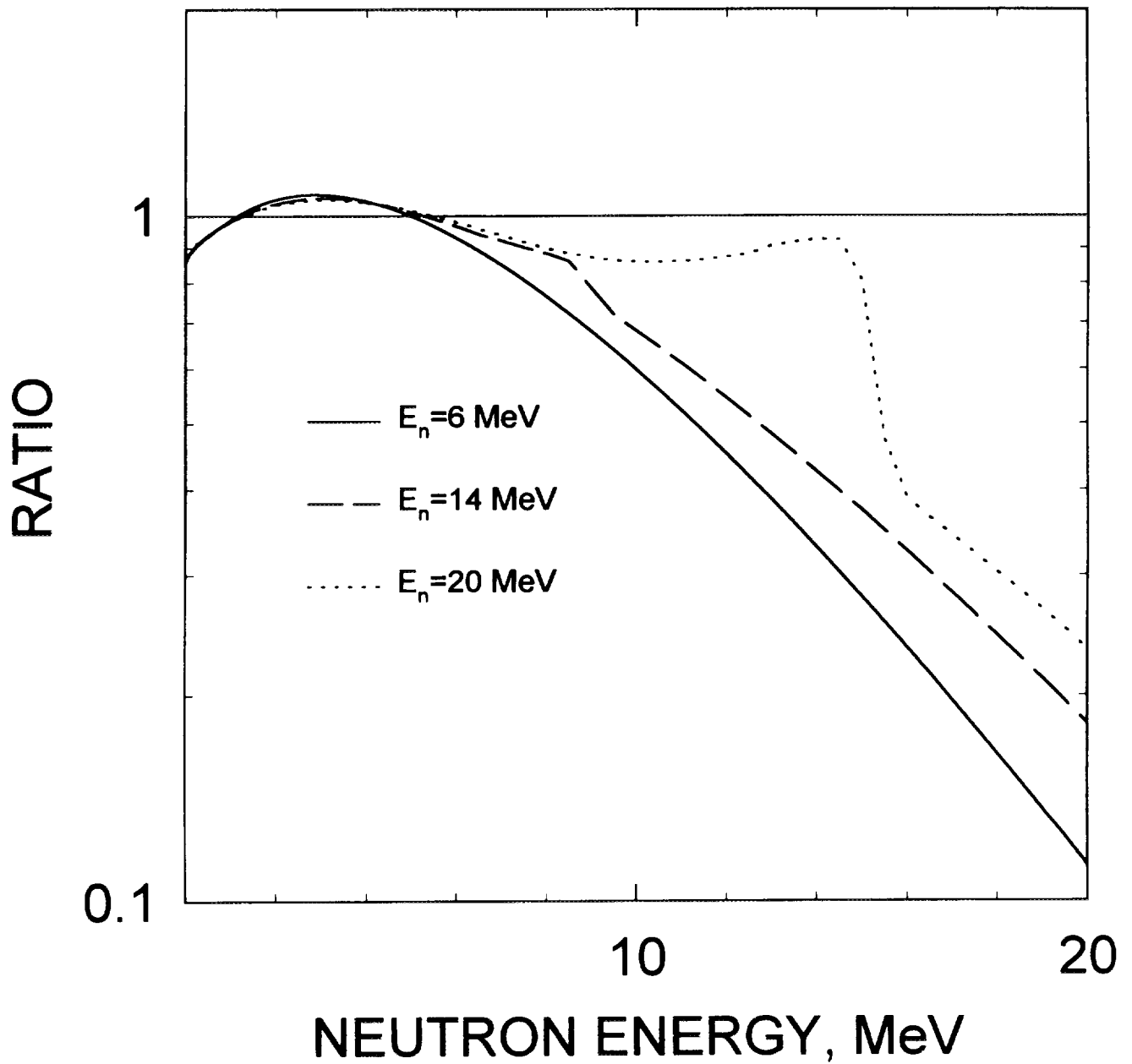


FIG. 5.8

$^{238}\text{Pu}$  PRESENT PROMPT FISSION  
SPECTRUM RATIO TO WATT  
SPECTRUM WITH THE SAME  
AVERAGE ENERGY

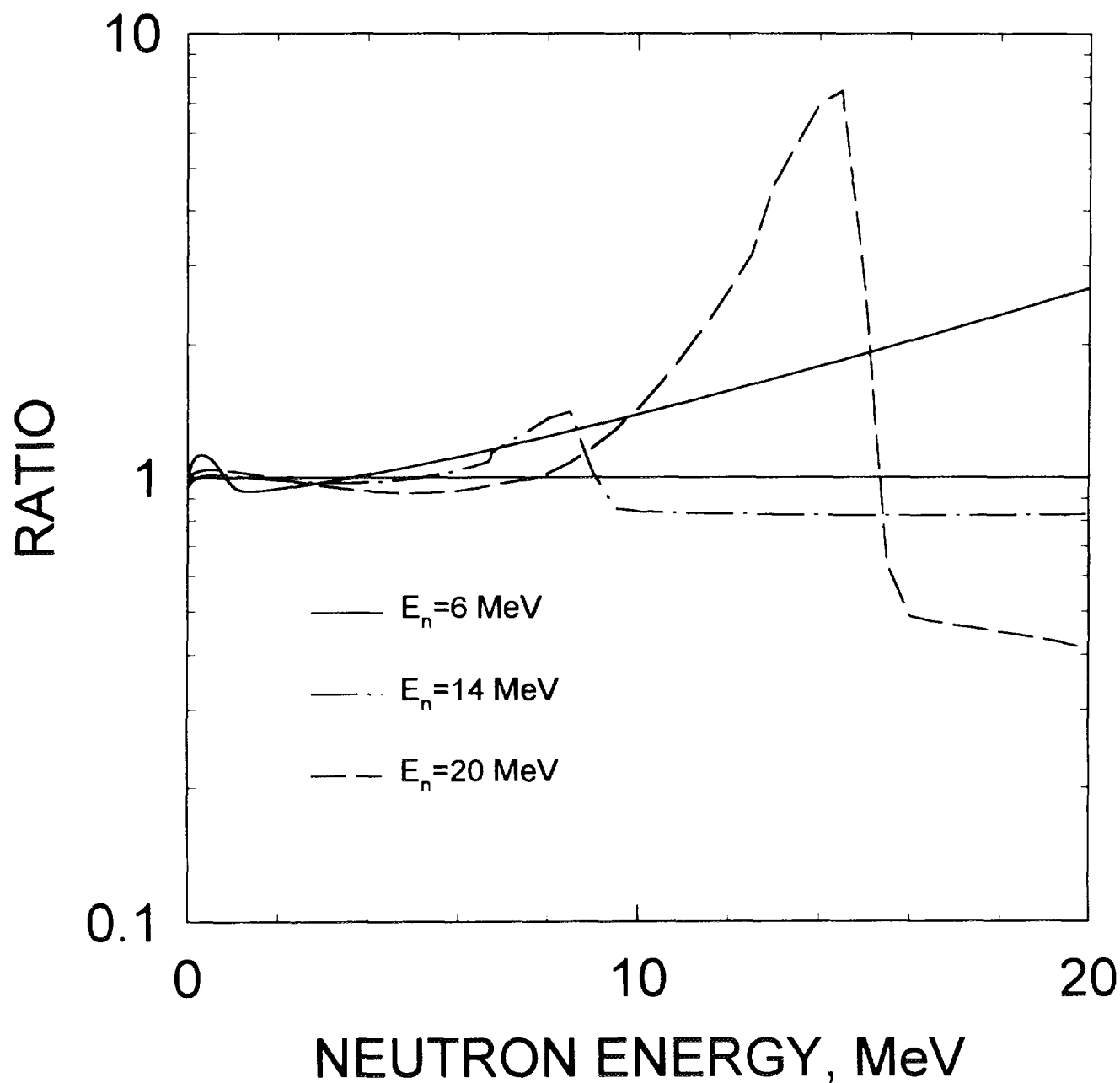


FIG. 5.9

$^{238}\text{Pu}$   
FISSION NEUTRON SPECTRA  
FOR  $E_n = 6 \text{ MeV}$

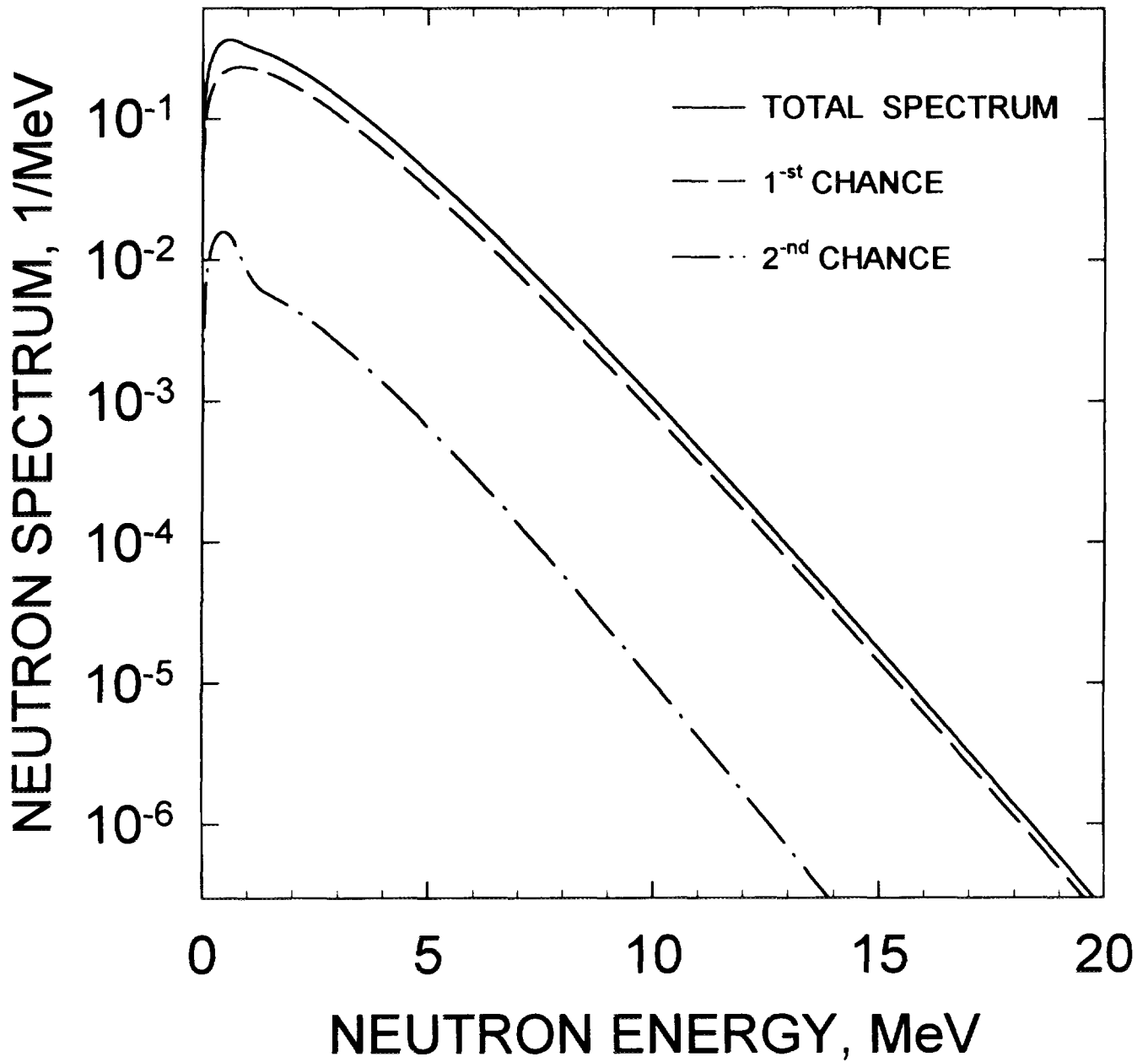


FIG.5.10

$^{238}\text{Pu}$   
FISSION NEUTRON SPECTRA  
FOR  $E_n = 14 \text{ MeV}$

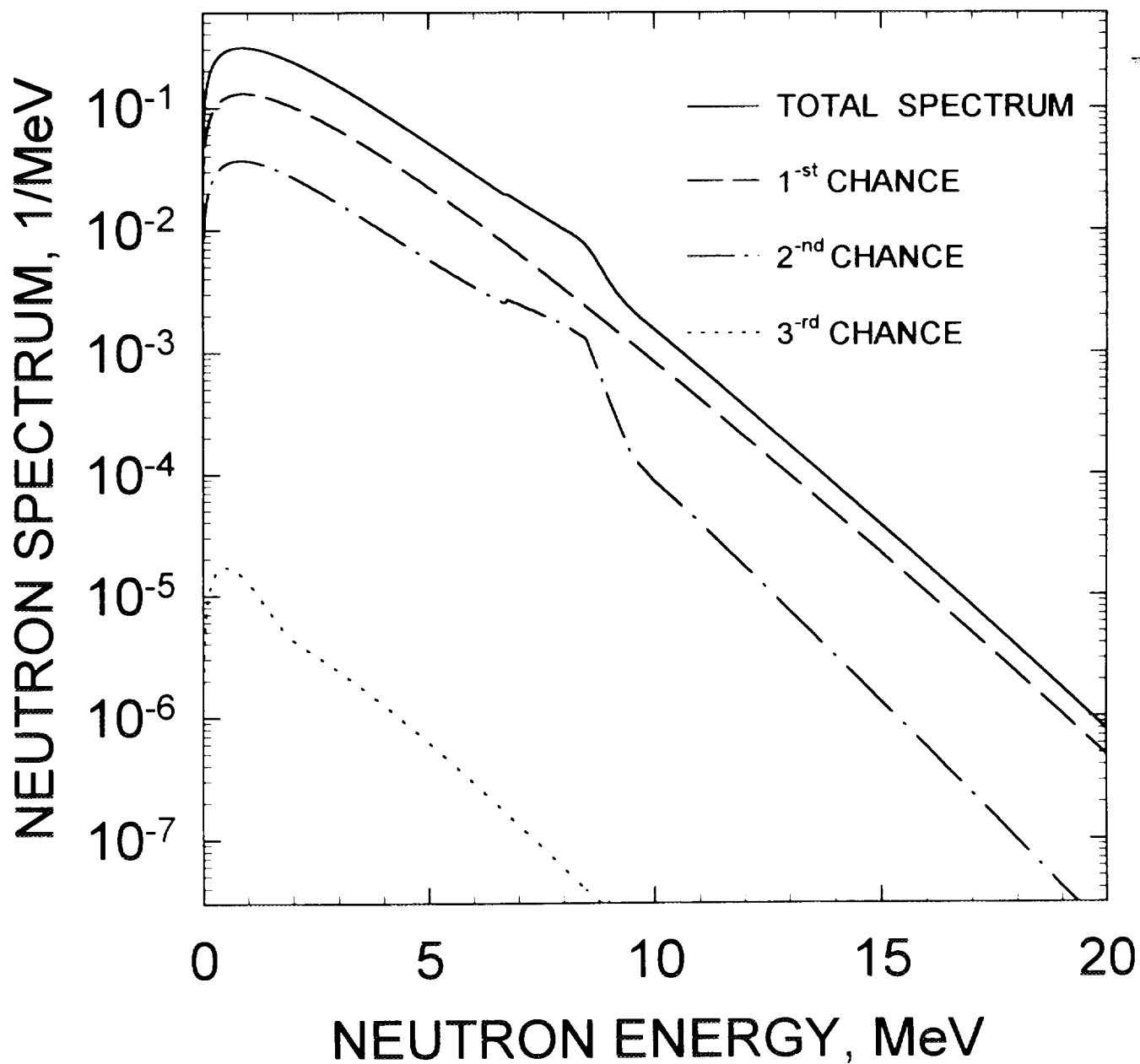


FIG.5.11



$^{238}\text{Pu}$   
FISSION NEUTRON SPECTRA  
FOR  $E_n = 20 \text{ MeV}$

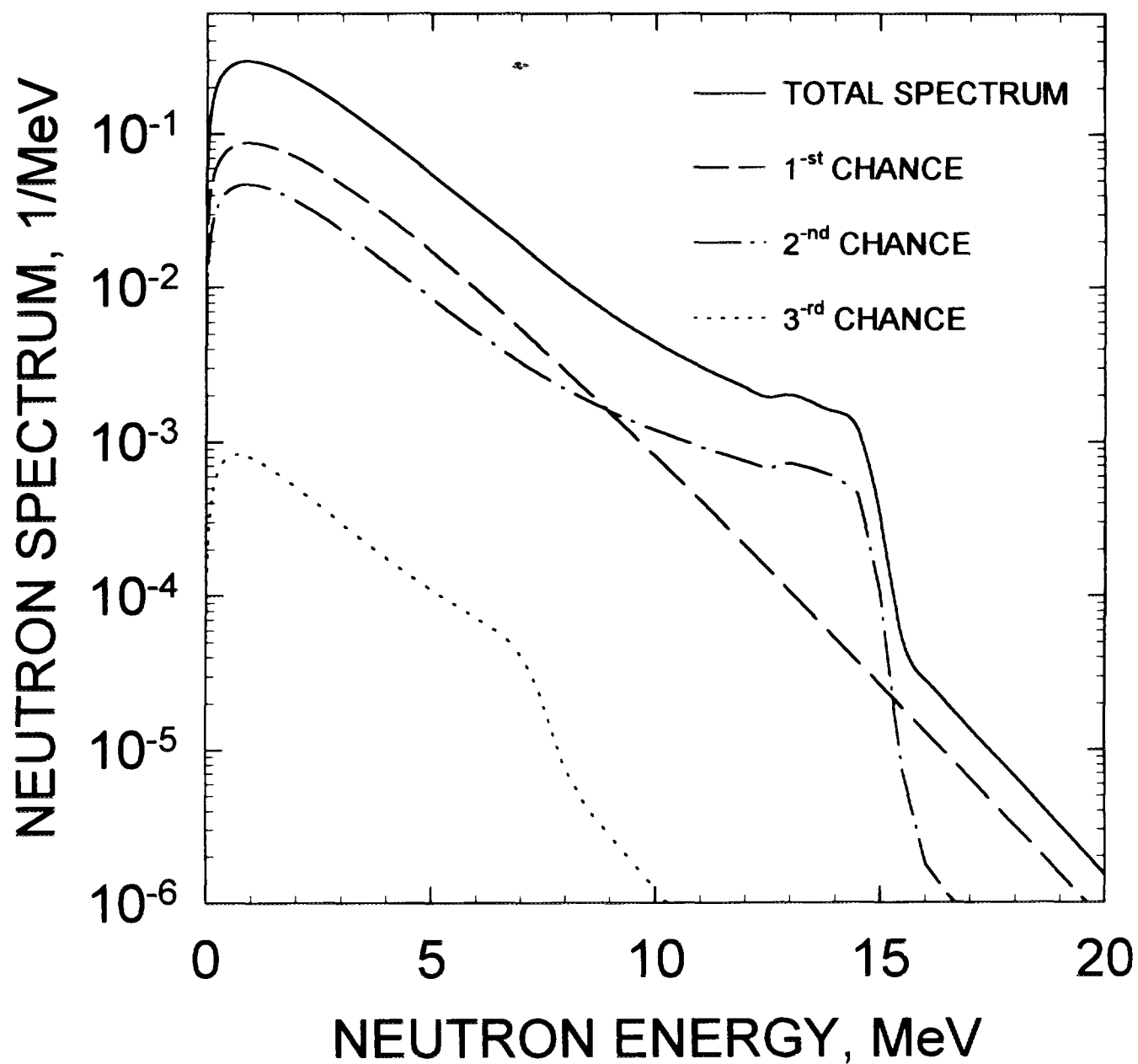


FIG.5.12

$^{238}\text{Pu}$  COMPARISON OF THE PROMPT  
NEUTRON FISSION SPECTRUM WITH  
ENDF/B-VI AND JENDL-3.2 ,  $E_n=15$  MeV

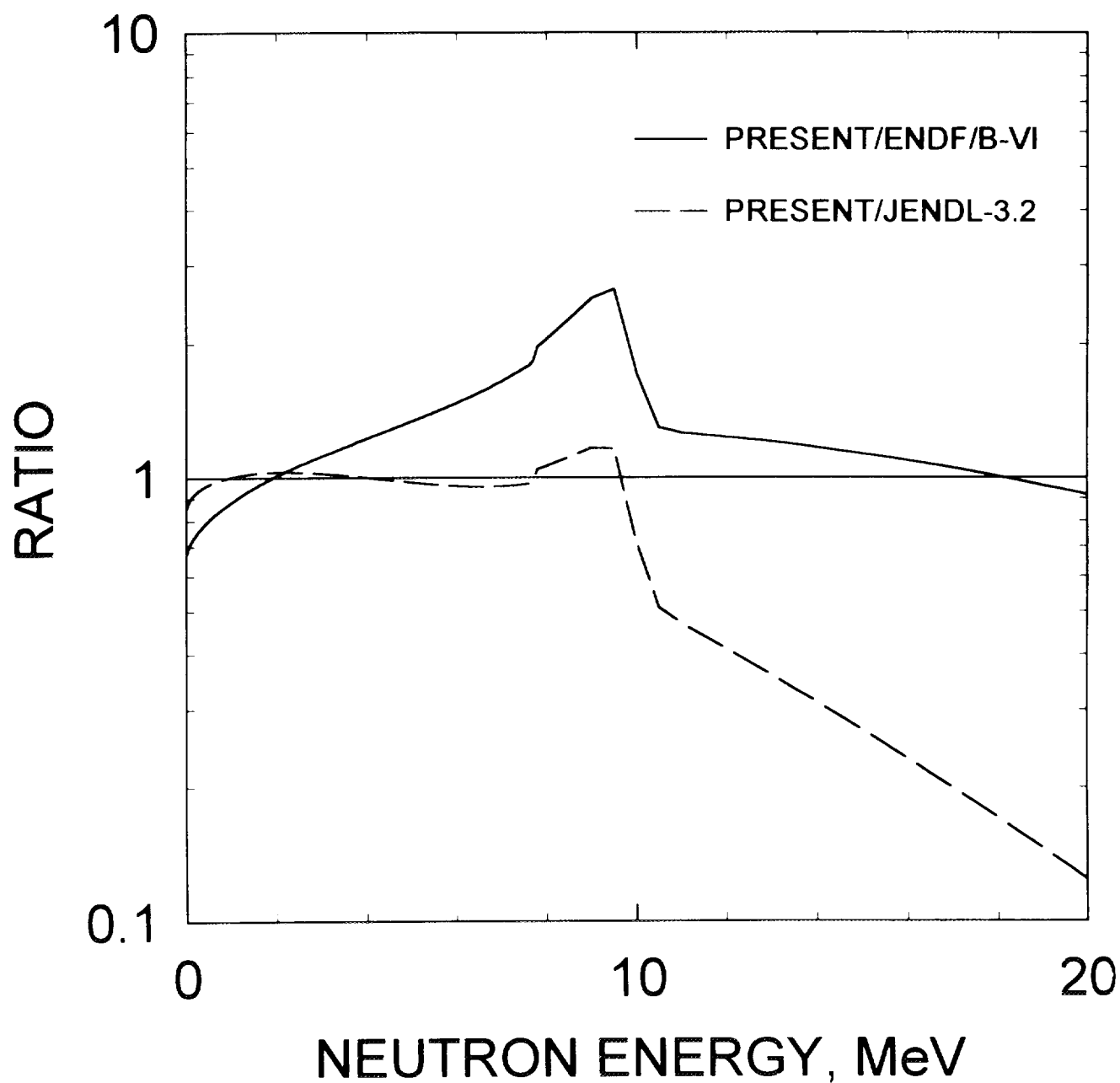


FIG. 5.13

# $^{238}\text{Pu}$ PROMPT NEUTRON MULTIPLICITY

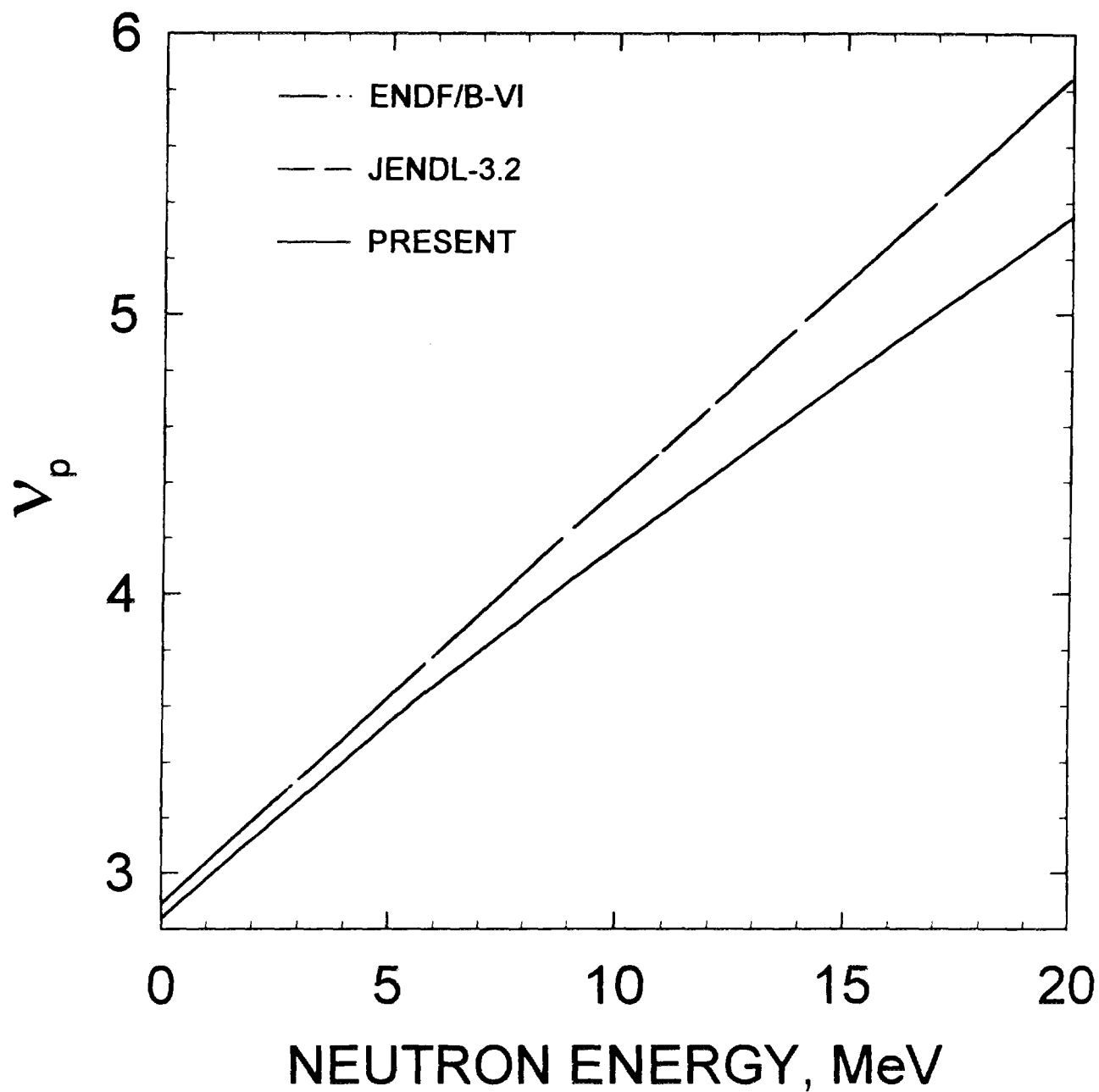


FIG.6.1

---

Nuclear Data Section  
International Atomic Energy Agency  
P.O. Box 100  
A-1400 Vienna  
Austria

e-mail: [services@iaeand.iaea.or.at](mailto:services@iaeand.iaea.or.at)  
fax: (43-1)20607  
cable: INATOM VIENNA  
telex: 1-12645 atom a  
telephone: (43-1)2060-21710

---

online: TELNET or FTP: [iaeand.iaea.or.at](http://iaeand.iaea.or.at)  
username: IAEANDS for interactive Nuclear Data Information System  
username: ANONYMOUS for FTP file transfer  
For users with Web-browsers: <http://www-nds.iaea.or.at>

---